UNIVERSITY OF OKLAHOMA

GRADUATE COLLEGE

DIFFUSIONAL CONSTRAINTS IMPLICATIONS IN C-C REACTIONS OVER BRØNSTED ACID SITES

A DISSERTATION

SUBMITTED TO THE GRADUATE FACULTY

in partial fulfillment of the requirements for the

Degree of

DOCTOR OF PHILOSOPHY

By

NILSON FRANCISCO LADAIM DE PAULA

Norman, Oklahoma

2023

Downloaded from SHAREOK. Persistent Handle URL: https://hdl.handle.net/11244/337706

DIFFUSIONAL CONSTRAINTS IMPLICATIONS IN C-C REACTIONS OVER BRØNSTED ACID SITES

A DISSERTATION APPROVED FOR THE
SCHOOL OF CHEMICAL, BIOLOGICAL AND MATERIALS ENGINEERING

BY THE COMMITTEE CONSISTING OF

Dr. Daniel E. Resasco, Chair

Dr. Steven P. Crossley

Dr. Bin Wang

Dr. Lance Lobban

Dr. Elizabeth C. Butler

© Copyright by NILSON FRANCISCO LADAIM DE PAULA 2023
All Rights Reserved.

Be the Glory and the Honor given to God, and God only!

With love to my parents Fernando and Solange for their tireless efforts for goods, and my whole family and friends.

Acknowledgements

First, I would like to thank God. In the moments of greatest need, I could find comfort in His Words. Without Him I would never have reached this point and for this I owe Him everything.

Second, I would like to express my greatest gratitude to my advisor Dr. Daniel Resasco, who has always helped me encouraging to think beyond and beyond. Your feedback and encouragement have been essential in shaping my research and helping me navigate the academic landscape. A person that I will forever be thankful for.

Special thanks to the catalyst group professors: Dr. Bin Wang, Dr. Lance Lobban and Dr. Steven Crossley. Your insightful comments, constructive criticism, and dedication to discuss ideas have been incredibly inspiring and motivating to keep moving. And also, I would like to thank Dr. Elizabeth Butler as well for participating as a committee member, it is an honor to have you.

I am also immensely grateful to my colleagues and friends that I have made until this point: Dr. Gengnan Li, Dr. Tuong Bui, Dr. Yang Feifei, Nabihan Abdul Rahman, Felipe Cruz, Marco Tulio Portella, Ana Carolina Jerdy, Thomas Sallas, Dr. Han Chau, Dr. Reda Bababrik, Dr. Eduardo Freitas, Alejandra Gomez, Ismaeel Alalq, and several others. Sharing our stories, beliefs and research projects were several times fruitful and I hope to maintain our friendships through our lives.

Mom and dad, Solange and Fernando; my friends, Thays Sagrillo, Fernanda Muniz, Julia Muniz, Gabriella Reis, Ivan Anholete, Elton Couto, Matheus Falceta, Sergio Bagude, Allana Calvano, Isabella Calvano, Francesca Marinoni; my cousins: Gabriela Ladaim, Rômulo Ladaim, Thalles Ladaim, Yago Ladaim, and everyone involved. Countless times

a single phone call or a simple message was so powerful that hold myself confident that I was doing the right thing.

My soccer club teammates and great friends. How many times we have travelled together and laughed about so many things. I am sorry for being old and not running as I was used to, lab hours also did not help much to keep my physique but at least I could put some 20 year olds on the bench for a couple games. And as I told you a couple months ago: you do not know how important y'all were to me during this PhD. Thanks soccer once again.

Sooner born and Sooner bred, when I die, I'll be Sooner dead! BOOMER SOONER!

Table of Contents

Acknowledgements ..... **v**

List of Tables ..... **ix**

List of Figures ..... **x**

ABSTRACT ..... **xvii**

Chapter 1 – Introduction and Research Direction **1**

1.1 Background and Initial Motivation 1
1.2 Definition and Properties of Zeolites 3
1.2.1 Zeolite Y 6
1.2.2 Zeolite MFI 10
1.3 Diffusion Concepts on Porous Catalysts and its Importance on Catalyst Studies 12
Internal Diffusion Limitations Studies in Zeolites 14
1.4 Organic Reactions over Acid Catalysts 18
1.4.1 Aldol Condensation 18
1.4.2 Catalytic Cracking 20
Research Objectives **23**

Chapter 2 – Mass-Transfer Limitations Investigation using Liquid Phase C-C Coupling Aldol Condensation Reactions in Porous Catalyst Media **24**

2.1 Introduction and Literature Review 24
2.2 Reaction-Transport Modeling 31
2.3 Experimental Methods 38
2.3.1 Chemicals and Materials 38
2.3.2 Catalyst Preparation 38
2.3.3 Site-density Quantification 38
2.3.4 X-ray diffraction Characterization 39
2.3.5 Particle Size Measurements 39
2.3.6 Catalytic Reaction Measurements 40
2.4 Results and Discussions 42
2.4.1 Catalyst Characterization 42

2.4.2 Catalytic reaction measurements and assessment of MTL in Self-Aldol Condensation 46
2.4.2 Cross-condensation Product Selectivity Shifts under Different Regimes 60
2.4.3 In-situ Pyridine Titration 65
2.5 Conclusion 78
Chapter 3 – MFI Synthesis: A Particle Size Effect Over Ketone-Condensation and Diffusivity Perspectives 82
3.1 Introduction and Literature Review 82
3.2 Experimental Methods 87
3.2.1 Chemicals and Materials 87
3.2.2 MFI Synthesis 87
3.2.3 Zeolite Characterization and Catalytic Reaction Measurements 87
3.3 Results and Discussions 89
3.3.1 Synthesized Zeolite Characterization 89
3.3.2 Catalytic Activity and Diffusion Discussions 94
3.4 Conclusions 106
Chapter 4 – Insights on Hydrocarbon Catalytic Cracking Over Zeolite Y, The Impact of Mesoporosity Introduction 108
4.1 Introduction and Literature Review 108
4.2 Experimental Methods 114
4.2.1 Chemicals and Materials 114
4.2.2 Site Density Counting 114
4.2.3 Gas-Phase Catalytic Reactions 114
4.3 Results and Discussions 116
4.3.1 Isooctane Cracking Mechanism over Acid Sites in Zeolites 116
4.3.2 Catalytic Cracking Differences Between Non-Steamed and Steamed Commercial Zeolite Y 120
4.3.3 Na-Titration over Commercial Zeolite Y 126
4.3.4 Pair-Acid Site Study over Y15: A Product Selectivity Analysis 132
4.4 Conclusion 139
References 141

List of Tables

Table 1: Bronsted acid site density of Y and ZSM5 partially Na-exchanged series. 45
Table 2: Reaction-diffusion parameters obtained from fitting the titration model. 50
Table 3: Dimer and trimer selectivity comparison in self-condensation of both ACE and CPO 53
Table 4: Calculated reaction and adsorption constant for CPO self-aldol condensation over Y30 from the reaction equations. 58
Table 5: Cross condensation reaction result outputs in Z140. 61
Table 6: Cross condensation reaction result outputs in Z40. 62
Table 7: Parameters obtained by fitting experimental data of cross-aldol condensation on the NaHY(Si/Al:30) series with the reaction-diffusion model. 64
Table 8: Classification of chemi- and physisorbed pyridine on acidic solids. Adapted from Ref [158]. 71
Table 9: Site density and average particle size of the synthesized ZSM5 zeolites. 93
Table 10: Site density and consumption rates of Na-titrated S-ZSM5 150 ^{o}C. 97
Table 11: Calculated Thiele moduli and effectiveness factors for the S-ZSM5 series. ... 98
Table 12: Product selectivity distribution on isobutane cracking over zeolite Y with varying Si/Al. 117
Table 13: Concentration of Brønsted acid sites on the commercial zeolite Y samples with different Si/Al ratios from Zeolyst International. 120

List of Figures

Figure 1: Brønsted acid site in zeolite catalysts, the reacting environment in which reaction frequently occurs. An elementary representation. 4

Figure 2: Scheme of the structure of zeolite Y. Reproduced from Ref [43]..... 7

Figure 3: XRD patterns of H-Y zeolite as changed by hydrothermal treatment at different temperatures: (a) initial H-Y zeolite, 298 K; (b) H-Y zeolite treated at 403 K; (c) H-Y zeolite treated at 423 K; (d) H-Y zeolite treated at 443 K; (e) H-Y zeolite treated at 473 K. Reproduced from Ref [47]. 8

Figure 4: Experimental (A) and deconvoluted (B) and ^{27}A1 MAS NMR spectra of hydrated (Hyd) and acac-treated (Acac) Sample 1. Reproduced from Ref [49]. 9

Figure 5: Perpendicular and regular channels in ZSM-5 lattice. Adapted from Ref [59]. 11

Figure 6: Desorption of isooctane at 428 K from small and large H-ZSM5-5 crystals in parent and mesoporous forms. Reproduced from Ref [89]..... 16

Figure 7: Measured selectivities to (a) methylhexane products as a function of the methylhexane Thiele modulus, ($\phi_{MH=}$) and (b) b-scission products as a function of the dimethylpentane Thiele modulus ($\phi_{DMP=}$) during nC7 isomerization on physical mixtures of Pt/SiO_2 and acid catalysts. Reproduced and adapted from Ref. [17]. 17

Figure 8: Acid catalyzed ketone aldol condensation reaction mechanism. An illustration. 19

Figure 9: a) classical cracking mechanism for an alkane molecule (RH) consisting of a H-transfer step to an absorbed carbenium ion ($R1^+$ followed by β-scission; b) cracking mechanism for an alkane molecule (HR) proceeding via carbonium ion route. Adapted from Ref [101]. 22

Figure 10: Spectra of hydroxyl region of various exchanged mordenites. Reproduced from Ref [130]. 28

Figure 11: Catalytic titration of W30Z-14.8: 2-butanol dehydration rate as a function of the cumulative amount of titrant (2,6-di-tert-butyl-pyridine or pyridine) adsorbed during reaction. Reproduced from Ref [141]. 29

Figure 12: Catalyst spherical controlled volume description. Draw by the author..... 31

Figure 13: Graphical correlation of effectiveness factor as Thiele modulus changes in a spherical catalyst particle. Generated by the author. 34
Figure 14: Image representation of a titrated catalyst particle with an inner active volume (‘a)’) and deactivated volume (‘b)’). Drawn by the author. 35
Figure 15: Reaction rate profile as a function of titrant uptake for Uniform Titration model (‘a)’) and Shrinking Core model (‘b)’). Generated by the author with representative values for Thiele modulus. 37
Figure 16: Isopropyl amine Hofmann elimination reaction representation. 39
Figure 17: Graphical representation of a high pressure batch reactor used for the catalytic measurements. 40
Figure 18: Scanning Electron Microscope pictures of ZSM5 (Si/Al =140 & 40) and Y. 42
Figure 19: X-ray diffraction patterns for the synthesized ZSM5 and commercial samples of ZSM5 and Y zeolites. 43
Figure 20: Temperature programmed decomposition of adsorbed isopropylamine (IPA-TPD) on the two Na-partially exchanged series of ZSM5 and Y zeolites. Propylene evolution in a 10 K/min heating ramp from IPA-saturated samples. 44
Figure 21: Carbonyl consumption rate as a function of concentration; a) acetone condensation on zeolite H-Z140 and b) cyclopentanone on H-Y30. 46
Figure 22: Self-condensation rates of CPO and ACE as a function of titrated site density in series of Na-exchange ZSM5 zeolite with Si/Al of 140. 47
Figure 23: High Na-loadings exchanged samples in comparison with simulated trend in cyclopentanone self-aldol condensation in Z140. 47
Figure 24: Self-condensation rates of CPO and ACE as a function of titrated site density in series of Na-exchange ZSM5 zeolite with Si/Al of 140. 48
Figure 25: Self-condensation rates of CPO and ACE as a function of titrated site density in a series of Na-exchange FAU zeolite. 49
Figure 26: Trimer total product selectivity second order dependence on ACE conversion in the self-aldol condensation in Y30 zeolite. 54
Figure 27: a) Experimental set of data for the studied zeolites and **b)** parity plot comparing the effectiveness factor calculated from Eq (1) and that obtained from the experimentally observed self-condensation rates relative to the maximum rate (no MTL). 55

Figure 28: Linearized plot of each kinetic model for the CPO self-aldol condensation in Y30. 57
Figure 29: Linearized plot of each kinetic model for the CPO self-aldol condensation in Y30. 58
Figure 30: Linearized plot of the Transition State Theory versus the inverse of reaction temperature. C_{CPO} = 1 mol/L. 59
Figure 31: Selectivity distribution of cross-aldol condensation of Ace-CPO in NaHY 30 series. 63
Figure 32: Rates of products formation as a function of Na-titrated site density in the NaHY (Si/Al:30) zeolite series (symbols) compared to calculated rates derived from the reaction-diffusion model. 64
Figure 33: Self-condensation rates of CPO and ACE as a function of in-situ pyridine uptake in ZSM5 zeolite with Si/Al of 140. The black point over the graph points to at zero rate at the measured IPA-TPD BAS density relative to Z140. 66
Figure 34: Comparison between experimental rates on pyridine with modeled Na-titration rates in ZSM5 zeolite with Si/Al of 140. 66
Figure 35: Self-condensation rates of CPO and ACE as a function of in-situ pyridine uptake in ZSM5 zeolite with Si/Al of 40. 67
Figure 36: Comparison between experimental rates on pyridine with modeled Na-titration rates in ZSM5 zeolite with Si/Al of 40. 68
Figure 37: Self-condensation rates of CPO and ACE as a function of in-situ pyridine uptake in Y zeolite with Si/Al of 30. 68
Figure 38: Comparison between experimental rates on pyridine with modeled Na-titration rates in Y zeolite with Si/Al of 30. 69
Figure 39: Relative activity drop as titrant agent is added in ZSM5 zeolite with Si/Al of 140 with **a)** pyridine addition, and **b)** Na-titration. 70
Figure 40: Relative activity drop as titrant agent is added in ZSM5 zeolite with Si/Al of 40 with **a)** pyridine addition, and **b)** Na-titration. 70
Figure 41: Relative activity drop as titrant agent is added in ZSM5 zeolite with Si/Al of 40 with **a)** pyridine addition, and **b)** Na-titration. 70

Figure 42: R spectrum of sorbed pyridine on the surface of zeolite Y (10 mg/cm^2) before heating (trace a) and after heating at 250 ◦C for 15 min (trace b) recorded in parallel mode with the FPA detector. The spectra are for the same sample at the same position in the cell. Reproduced from Ref [158]. 72
Figure 43: IR spectrum of sorbed pyridine on the surface of H-ZSM-5 (10 mg/cm^2) before heating (trace a) and after heating at 250 ◦C for 15 min (trace b) recorded in parallel mode with the FPA detector. The spectra are for the same sample at the same position in the cell. Reproduced from Ref [158]. 72
Figure 44: Ultraviolet visible light spectra of a mixture containing 400 mg of catalyst ('a)' respective to zeolite ZSM5, and 'b)' to zeolite Y) in 100 mL of cyclohexane as solvent with 0.20 mmol/g_{cat} of pyridine added. 74
Figure 45: Ultraviolet visible light spectra of a mixture containing 400 mg of zeolite ZSM5 in 100 mL of cyclohexane as solvent with 0.20 ('W Py'), 0.40 ('W Py2x') and 0.60 ('W Py3x') mmol/g_{cat} of pyridine added. 75
Figure 46: Rates of products formation as a function of pyridine uptake in Y30 zeolite in respect to [A] products ('a)') and [C] products ('b)'). 77
Figure 47: Selectivity distribution of cross-aldol condensation of ACE-CPO in Y30 through in-situ pyridine titration. 77
Figure 48: Transmission electron microscopy images of nano ZSM-5 samples Z-2 and Z-3. Reproduced from Ref [183]. 84
Figure 49: Synthesized ZSM-5 zeolites FE-SEM images in various template ratios. Adapted from Ref [183]. 85
Figure 50: Idealized schematic of a finned zeolite in which the fins have the same crystallographic registry as the seed (left image). Illustration of a finned zeolite that comprises continuous channels throughout the seed (size β) and fins (size α) with characteristic fin dimensions of α×α×α. Adapted from Ref [193]. 86
Figure 51: X-ray diffraction spectrum of synthesized ZSM5 zeolites and commercial ZSM5 sample. 89
Figure 52: X-ray diffraction spectrum of synthesized ZSM5 zeolites at 150 ^{o}C with different crystallization periods. 90

Figure 53: Temperature programmed decomposition of adsorbed isopropylamine (IPA-TPD) on four synthesized ZSM5 samples. Propylene evolution in a 10 K/min heating ramp from IPA-saturated samples. 91
Figure 54: Scanning Electron Microscope pictures of four S-ZSM5 (Si/Al =80) at similar magnification (27 KX). 92
Figure 55: Scanning Electron Microscope pictures of four S-ZSM5 (Si/Al =80) at similar magnification (120 KX). 93
Figure 56: Scanning Electron Microscope pictures of S-ZSM5 150 ^{o}C (Si/Al =80) at different crystallization periods (72 and 120hrs). 94
Figure 57: Self-aldol condensation rates of acetone and cyclopentanone over S-ZSM5s. Reaction conditions: 250 ^{o}C, 1 mol/L feeding reactant, 1 hour of reaction time. 250 mg of catalyst. 95
Figure 58: Self-aldol condensation rates of acetone and cyclopentanone over S-ZSM5s with different crystallization periods. Reaction conditions: 250 ^{o}C, 1 mol/L feeding reactant, 1 hour of reaction time. 250 mg of catalyst. 96
Figure 59: Self-aldol condensation rates of acetone and cyclopentanone over Na-titrated S-ZSM5 150 ^{o}C samples as a function of titrated acid sites. Reaction conditions: 250 ^{o}C, 1 mol/L feeding reactant, 1 hour of reaction time. 250 mg of catalyst. 97
Figure 60: Theoretical Thiele modulus and correspondent effectiveness factor calculated based on consumption catalytic rates of acetone and cyclopentanone. 98
Figure 61: Self-aldol condensation rates of acetone and cyclopentanone over Na-titrated S-ZSM5 160 ^{o}C samples as a function of titrated acid sites. Reaction conditions: 250 ^{o}C, 1 mol/L feeding reactant, 1 hour of reaction time, 250 mg of catalyst. 99
Figure 62: Scanning Electron Microscope pictures of S-ZSM5 150 ^{o}C (Si/Al =80) with different Na loadings (Na0.0625 and Na0.25) calculated based on a TPAOH molar amount. 101
Figure 63: Catalytic measurements of the self-aldol condensation rates of acetone and cyclopentanone with Na-added during synthesis compared to Na-titrated S-ZSM5 150 ^{o}C samples as a function of titrated acid sites. Reaction conditions: 250 ^{o}C, 1 mol/L feeding reactant, 1 hour of reaction time. 250 mg of catalyst. 102

Figure 64: Scanning Electron Microscope pictures of 0.5TPAOH S-ZSM5 150 ºC (Si/Al =80). 104
Figure 65: Carbocation initiation in heptane (model molecule), a first elementary step onto catalytic cracking reaction. A model representation. 109
Figure 66: Conventional TEM images of severely steamed and subsequently acid-leached zeolite Y crystals with Si/Al ratios 15 (a) and 30 (b), commercially available as CBV-720 and CBV-760, respectively, from Zeolyst. Reproduced from Ref [214]. 112
Figure 67: a) Product distribution of 2,5-dimethylhexane catalytic cracking over zeolite Y15 in flow mode. Bar representation is relative to product distribution within progressing reactant time on stream. Reaction conditions: 400 ºC, 50 mg, 0.5 mL of reactant injected per hour, 100 mL/min of N_2 inert flow. Pretreatment under N_2 at 300 ºC for 2 hours prior injection. **b)** 2,5-dimethyl hexane carbon positioning notation. 118
Figure 68: Isooctane cracking conversion comparison among the commercial zeolite Y samples. Reaction conditions: 400 ºC, 50 mg, 0.5 mL of reactant injected per hour, 100 mL/min of N_2 inert flow. Pretreatment under N_2 at 300 ºC for 2 hours prior injection. 121
Figure 69: Product selectivity of isooctane cracking over zeolite Y2.6 (a and b), Y15 (c and d) and Y30 (e and f). Reaction conditions: 400 ºC, 0.5 mL of reactant injected per hour, 100 mL/min of N_2 inert flow. Pretreatment under N_2 at 300 ºC for 2 hours prior injection. 123
Figure 70: C_1 selectivity as a function of isooctane conversion over zeolite Y2.6, Y15, and Y30 in pulse mode. Reaction conditions: 400 ºC, 0.5 mL of reactant injected per hour, 100 mL/min of N_2 inert flow. Pretreatment under N_2 at 300 ºC for 2 hours prior injection. 124
Figure 71: H-transfer ratio at low isooctane conversions over zeolite Y2.6, Y15, and Y30. Reaction conditions: 400 ºC, 0.5 mL of reactant injected per hour, 100 mL/min of N_2 inert flow. Pretreatment under N_2 at 300 ºC for 2 hours prior injection. 126
Figure 72: Pulse mode catalytic conversion of isooctane as a function of titrated site density in series of Na-exchange Y zeolite with Si/Al of 2.6. The marker color darkens from blue to lack as the number of pulses increases. The red marker over x-axis is relative to the calculated BAS density of the non-exchanged parent Y2.6. For Y2.6 a fixed 50 mg of catalyst is used. 127

Figure 73: Pulse mode catalytic conversion of heptane as a function of titrated site density in series of Na-exchange Y zeolite with Si/Al of 2.6. The marker color darkens from blue to black as the number of pulses increases. The red marker over x-axis is relative to the calculated BAS density of the non-exchanged parent Y2.6. For Y2.6 a fixed 50 mg of catalyst is used. 128
Figure 74: Pulse mode catalytic conversion of isooctane as a function of titrated site density in series of Na-exchange Y zeolite with Si/Al of 15. The marker blue colors turns darker as the number of pulses increases. The red marker over x-axis is relative to the calculated BAS density of the non-exchanged parent 15. For Y15 a fixed 3.5 mg of catalyst is used..... 129
Figure 75: Pulse mode catalytic conversion of isooctane as a function of titrated site density in series of Na-exchange Y zeolite with Si/Al of 30. The marker blue colors turns darker as the number of pulses increases. The red marker over x-axis is relative to the calculated BAS density of the non-exchanged parent 30. For Y30 a fixed 12.5 mg of catalyst is used. 130
Figure 76: Relative isooctane conversion activity as a function of percentage of titrates sites in zeolite Y15 and Y30 in pulse mode reactions. 131
Figure 77: Relative isooctane conversion activity as a function of percentage of titrates sites in zeolite Y15 and Y30 in flow mode reactions. 132
Figure 78: a) H-transfer ratio ($C_4/C_{4=}$) and **b)** C_1 selectivity as a function isooctane conversion in zeolite Y15. A comparison between reaction modes. 134
Figure 79: Conversion difference between initial Y15 and metal-exchanged zeolites, both as per Brønsted acid site basis gram of catalysis basis. 135
Figure 80: H-transfer ratio ($C_4/C_{4=}$) as a function isooctane conversion in zeolite Y15 and Na, Ca and Co-exchanged samples in a) pulse and b) flow reaction mode. 136
Figure 81: C_1 selectivity as a function isooctane conversion in zeolite Y15, Na, Ca and Co-exchanged samples in pulse and flow reaction mode. 137
Figure 82: The inverse correlation between H-transfer ratio ($C_4/C_{4=}$) and C_1 selectivity over zeolite Y15, Na and Ca-exchanged samples in both reaction modes. 138

ABSTRACT

The constrained pore structure and catalytic properties of zeolites can occasionally offer diffusion limitations to a molecule during the course of a chemical reaction. These constraints significantly impact the rate of condensation or cracking, either as a result of the spatial conformation of the reacting molecule inside a confined domain or the high catalytic activity of a reacting site. It is proposed an experimental approach to conveniently control the concentration of acid sites in commercial zeolite samples using the exchange property of that active proton and an alkaline atom such as sodium (Na). By combining this approach with reaction-diffusion modeling, one can measure the extent of mass-transfer limitations (MTL) in different catalytic systems and analyze the change in product selectivity or rate profile as the governing regime changes. In the case of comparing the structural differences between reactants such as acetone and cyclopentanone in restrained environments, a notable impact was observed due to the larger volume of the molecule. As the space voids increase from one constrained zeolite topology to a more accessible structure, a lower degree of mass-transfer limitations is detected. However, for the smaller reacting particle could access hindered sites as compared to the larger reactant, resulting in a higher consumption rate and notable mass-transfer limitations relative to site activity rather than spatial restraints. Instead of deactivating a site prior to the catalytic reaction, it is also investigated the in-situ addition of an inert-poison specie. While alkaline-exchange was relatively effective in quantitatively determining the extent of MTL, in-situ additions were successful in qualitatively controlling the governing regime properties and affecting the product distribution as a consequence. The structural similarities between the solvent

and the titrant molecule resulted in a certain degree of desorption, which was inadequate for ascertaining the concentration of acid sites, as observed in literature.

To conveniently control the particle size through zeolite synthesis, one can also acknowledge the effect of diffusion on reaction rate. This particle presented an agglomeration of nanoaggregates over the outer surface of a big unchanged particle, in which occurred to considerably contribute towards the catalytic activity. Na-titration was able to identify mass-transfer limitations in the most active sample, but it was limited in explaining the activity reduction for the larger nanoparticle size sample.

While controlling the concentration of acid sites was proven experimentally to diminish the influence of mass-transfer limitations, the presence of mesoporosity is also another experimental route towards decrease such limitations and it is investigated here for the commercial samples of zeolite Y. The parent form of zeolite Y presented a certain degree of diffusion restraint, but as mesoporous channels were introduced, a boost in activity occurred for hydrocarbon cracking, probably through an exposure of synergistic sites. These were assumed to be either sites located in more active environments or proximate enough to contribute to a higher catalytic rate. Na-titration was adequate in identifying their contribution in activity in mesoporous samples, and decreasing the Bronsted acid density also supports the idea that proximate sites were contributing to the higher catalytic activity. By using different titrant cations, preferential titration over those synergistic sites occurred in all cases, being more effective as a bivalent cation addition. The mechanistic discussion of whether those sites favored cracking via protonation of a saturated or unsaturated hydrocarbon was performed, showing the inverse correlation between the reaction pathways rather than specific features of a catalyst only.

The results reveal the complex interplay between the reaction kinetics, diffusion limitations, and product selectivity, and provide insights into how to optimize zeolite catalysts for different applications. Overall, this work contributes to a better understanding of the fundamental mechanisms governing diffusion limitations in zeolites and provides a feasible experimental approach to more efficient design and selective processes results, being controlling the extent of mass-transfer limitations or restricting a site functioning that favors a specific reaction route.

Chapter 1 – Introduction and Research Direction

1.1 Background and Initial Motivation

Zeolites are crystalline materials with a well-defined pore structure that allows them to act as molecular sieves industry [1, 2]. These materials are widely used in various industrial applications, including separation, catalysis, and ion exchange. In particular, zeolite catalysts are critical for many important chemical processes, including petrochemical refining, chemical synthesis, and environmental remediation.

The first industrial application of zeolites is dated in the 1940s, when an American corporation discovered that synthetic zeolites had an enhanced performance in the production of gasoline and other fuels compared to platinum and palladium catalysts used before [3]. These materials are usually found in nature close to volcanic areas, naturally occurring from the reaction of volcanic ashes and alkaline groundwater [4]. Zeolites as chabazite and natrolite are common types of these natural catalyst each with unique crystal structure and properties. Still, due to the lack of control of the crystal properties, these materials are not used in industry, instead, synthetic zeolites assure the control of purity, uniformity, and specific crystal properties directly related to the application it is design for and thus preferential.

Because of the atoms arrangement in the crystalline structure of the zeolite, it provides improved catalytic properties resulted from the constrained pore pattern [5]. As a consequence of the constrained aperture, high energy intermediates are stabilized due to the close contact and interaction with the atoms in the framework; additionally, the constrained aperture creates shape selectivity, determining which molecules can diffuse

inside the catalyst volume and influencing the products formed [6]. However, the performance of zeolite catalysts can be limited by diffusion limitations, which occur when reactant molecules struggle to access the active sites within the zeolite pores [7-9]. These limitations can lead to reduced reaction rates and selectivity, as well as catalyst deactivation due to coke formation. To improve the efficiency and effectiveness of zeolite catalysts, it is crucial to understand and mitigate these diffusion limitations.

Researchers have used various experimental and theoretical techniques to study diffusion in zeolites, including molecular simulations, and experimental spectroscopy approaches [10-12]. These studies have shown that the transport properties of zeolites, such as the diffusivity and permeability of different species through the zeolite pore structure, can be affected by factors such as pore size, shape, and connectivity, as well as the presence of adsorbates and cations. A recent work by Porter and O'Malley (2021) highlights the importance of considering factors that can influence diffusion in zeolites, including the dynamic effects of adsorbate molecules and the presence of defects in the zeolite structure [13]. The authors also discuss recent advances in experimental and computational techniques for studying diffusion in zeolites, as well as the potential for using machine learning approaches to develop predictive models of diffusion behavior.

Other recent studies have focused on developing new synthesis strategies for zeolites with tailored pore structures, which can help to optimize catalyst performance by reducing diffusion limitations deactivation [14, 15]. For example, Zhang et al. reported a new method for synthesizing hierarchical zeolites with a dual-pore structure, which showed improved catalytic activity and selectivity for the conversion of bulky molecules compared to conventional zeolites [16]. While the mesopores conferred an enhanced transport inside

the catalytic environment, the micropores were responsible for the molecular selectivity and improved catalytic activity.

Aforesaid transport constraints generate local concentration gradients of a reacting species inside of a catalyst volume not only impacting the activity alone, but also product selectivity. A molecule residence time increases inside these porous domains and favor parallel and sequential reactions as a consequence [17].

The need to better understand the impact of diffusion in zeolitic environments, with the aim of identifying and quantifying its extent, is a key motivation for research. Next, an overview of the current understanding of zeolites and diffusion in heterogeneous catalysis is provided, highlighting opportunities for ongoing contributions to this field and for developing experimental approaches to address current interests.

1.2 Definition and Properties of Zeolites

Zeolites are composed of a three-dimensional framework of tetrahedrally coordinated silica and alumina, which are linked together by oxygen atoms to form a porous and well defined crystalline structure [18]. One of the most important properties of zeolites is their high surface area and porosity, allowing them to selectively trap and convert small molecules such as water, carbon dioxide, and nitrogen oxides [19-21]. The pore size and shape of zeolites can vary depending on the arrangement of the tetrahedra guided by the presence of cations structure directing agents (SDAs) during the zeolite synthesis. Different structural features (cages, and channels) are obtained as a function of synthesis/gel mixture, nucleation and crystal growth conditions, and SDAs used [22-24].

This structural diversity gives rise to a wide range of adsorption and catalytic properties in zeolites, which are exploited in many industrial applications.

In addition to their high surface area, zeolites also exhibit a unique ion-exchange capacity. The cations within the zeolite structure can be exchanged with other cations in solution, which can be exploited to selectively remove or recover ions from a mixture. This property arises from the nature of that aluminum cation in the framework incorporated in the tetrahedral position. Originally, alumina (Al_2O_3) is found in its most stable form as octahedrally coordinated with 4-5 oxygens whereas silica assembles a 3-dimensional structure covalently bonded in a tetrahedral form to 4 oxygen atoms [25, 26]. As the primary units of a crystal composed by silica grow, aluminum can substitute that silicon tetrahedral position due to their comparable ionic radii as well as for its considerable presence in the nutrient solution [27]. This replacement results in a negative charge imbalance in the zeolite structure (Si^{4+} vs. Al^{3+}), which is compensated for by the presence of cations such as sodium or potassium [28]. Through a cation exchange of these alkali species with a NH_4^+ salt and additional thermal treatment a bridging hydroxyl emerges from the catalyst surface giving rise to an exposed proton which are known to be the reaction sites of the zeolites. This proton is also referred to as Brønsted acid site (BAS) (**Figure 1**).

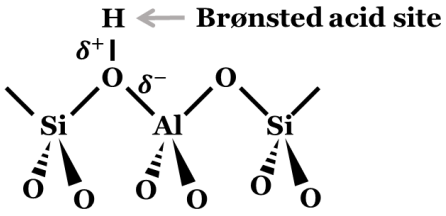

Figure 1: Brønsted acid site in zeolite catalysts, the reacting environment in which reaction frequently occurs. An elementary representation.

The degree of aluminum substitution can be controlled during zeolite synthesis by adjusting the composition of the precursor materials and the reaction conditions. In some cases, however, excessive aluminum substitution can lead to the formation of amorphous or poorly crystalline materials, which can reduce the adsorption and catalytic properties of the zeolite [29-31]. Understanding the factors that control aluminum substitution is essential for the development of new zeolite structures with tailored properties for specific industrial applications. One example is the excellent thermal and chemical stability of zeolites, which makes them suitable for use in high-temperature and corrosive environments, arisen from the strong covalent bonds between the atoms in the zeolite structure, giving the material a high degree of rigidity and resistance to deformation [32, 33]. This property is convenient in petroleum cracking and catalytic reforming reactions, where catalyst stability and catalytic activity are critical to the success of the process [34].

Two of the most commonly used zeolite structures for commercial purposes are the zeolites Y and MFI. Both materials have unique properties, as their pore sizes and structural stability, that are attractive for a wide range of industrial applications [35].

In the case of zeolite Y, its use is primarily in the petrochemical industry in chemical reactions as cracking and isomerization, in particular in fluid catalytic cracking (FCC) of heavy petroleum fraction into more energetically valuable compounds [36]. FCC is part of a refinery process involving C-C bond cleavage of long-chain hydrocarbons in a continuous gas-phase flow at high temperatures through a zeolitic catalyst bed. During the course of reaction, the smaller products are sent to a fractionator responsible for separating the product stream mixture and direct them for further processing, while the spent catalyst is left with residual coke and conducted to regenerator vessel. In an oxygen environment

and appropriate condition, coke is burned off and the refreshed catalyst is returned to the FCC reactor vessel for its continuous use.

Unlike cracking reactions, in the petrochemical industry MFI is extensively used in alkylation reactions. The production of high-octane gasoline through alkylation of olefins improves the octane rating of that product resulting in an improved the fuel performance [36, 37]. Typically, when an alkylation agent (either an alkene or alcohol) is co-fed with another coupling molecule, the acid sites present in MFI serve to adsorb and-or activate this agent and through a concerted mechanism, catalyze the formation of a C-C bond between the reactants [38].

The conversion of biomass into biofuels and chemicals is another important use of MFI zeolites. This catalyst is responsible for enhanced catalytic dehydration activity and lowering the oxygen content of sugars and biomass-derived compounds, which accounts for the large production of furan, a constituent of chemicals and materials for the use in polymers and resins, e.g. [39, 40]. Isomerization and cyclization reactions are also commonly used reactions in MFI being valuable towards generating more energetically valuable and stable chemical species taking advantage of the acidic and distinct shape-selectivity properties of the presented catalyst [41, 42].

Next, important details of each catalyst is discussed to clarify aspects necessary to the understanding of the ongoing study.

1.2.1 Zeolite Y

Zeoltie Y, also known as faujasite, is a large-pore catalyst with a three-dimensional structure consisting of interconnected cages and channels. These interconnection units are 12 membered-rings channels with an aperture diameter of approximately 7.4 Angstroms

(Å) and an internal cage with a diameter of 13 Å, which can also be defined as supercages [2]. In this zeolite, the stacking primary units of tetrahedrally coordinated silica and alumina forms a sodalite unit which replicates and piles over one another through a hexagonal prism. The resulting crystalline structure is presented in **Figure 2**. These apertures makes this zeolite suitable for the diffusion of large molecules as long hydrocarbon chains.

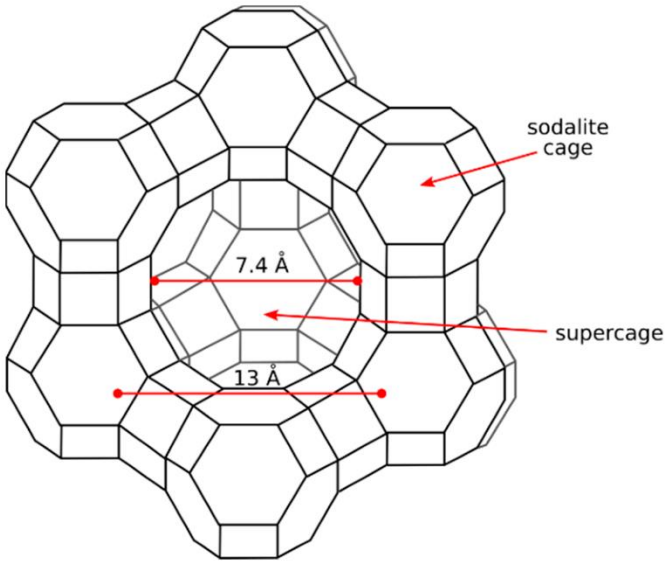

Figure 2: Scheme of the structure of zeolite Y. Reproduced from Ref [43].

It has a Si/Al ratio of approximately 2.5 with a consequent high concentration of BAS resulting in problems associated decreased hydrothermal stability. This is explained by the easy aluminum extraction at high temperature treatments and in the presence of water, an accelerated hydrolysis, leading to structural degradation [44, 45]. At these conditions this reaction is characterization by breaking down Al-O-Si bonds into Si-OH (silanols) and Al-OH bonds, which are less stable than their original form and result in the structure collapse [46]. The loss in crystallography can be observed in **Figure 3**, a work

done by Dimitrijevic et al. by treating as synthesized H-Y (Si/Al 2.7) samples in hot liquid water in temperatures ranging from 403-473 K for 72 hours [47].

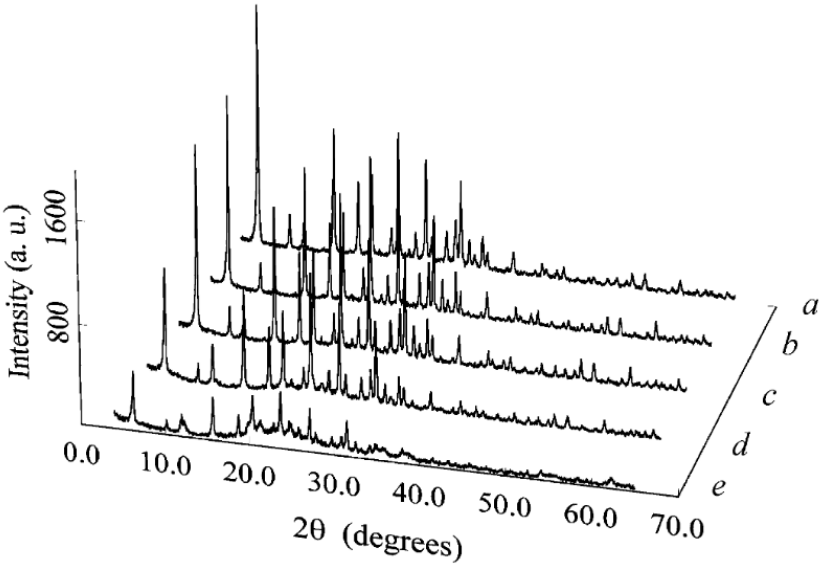

Figure 3: XRD patterns of H-Y zeolite as changed by hydrothermal treatment at different temperatures: (a) initial H-Y zeolite, 298 K; (b) H-Y zeolite treated at 403 K; (c) H-Y zeolite treated at 423 K; (d) H-Y zeolite treated at 443 K; (e) H-Y zeolite treated at 473 K. Reproduced from Ref [47].

Such aluminum extraction happens to result in the presence of extra-framework alumina (EFAL) species, which refers to aluminum oxides existing outside the zeolite framework in different forms, such as isolated AlOx species, clusters, or layers [48]. The nature and amount of EFAL can depend on the method of preparation, the composition of the starting zeolite, and the conditions of the treatment. One way to identify their presence over a local environment in zeolites is through a solid-state nuclear magnetic resonance (NMR) spectroscopy in which EFAL species have different NMR chemical shifts (~0 ppm) and relaxation times than those incorporated in the framework (~60 ppm). A study of dealuminated zeolite Y by Grobet et al. identified a slight presence of EFAL in self-steamed hydrated NH4-Y sample at 873K for 4 hours with a pronounced increased of those species once treated with acetylacetone to cause aluminum extraction (**Figure 4**) [49].

Intermediate peaks relative to 0 and 60 ppm are attributed to partially EFAL, a penta-coordinated alumina that has not been fully extracted from the surface [50].

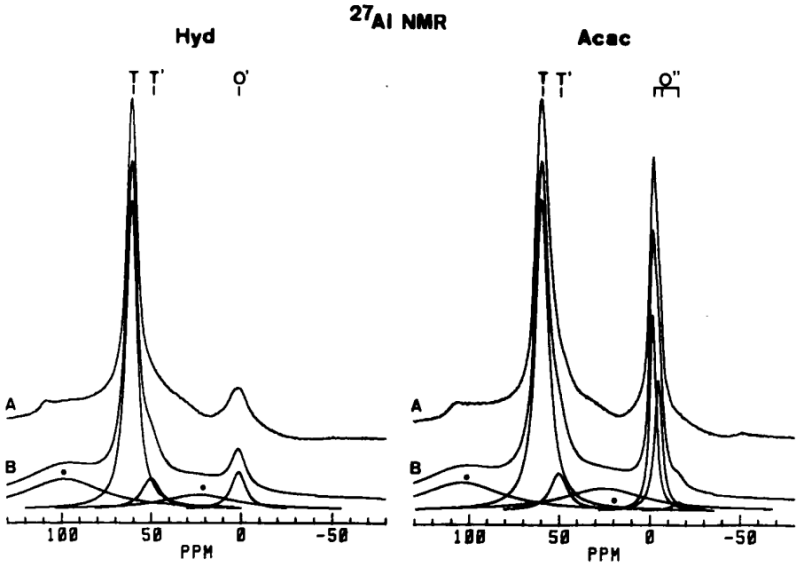

Figure 4: Experimental (A) and deconvoluted (B) and ^{27}A1 MAS NMR spectra of hydrated (Hyd) and acac-treated (Acac) Sample 1. Reproduced from Ref [49].

The presence of these partial Al extractions and EFAL seem to be detrimental to the stability of that low Si/Al zeolite, however it actually prevents further hydrolysis. It occurs due to the fact that dealumination increases Si/Al resulting in a stronger and more stable Si-O-Si bonds, also because EFAL acts as protective layer around the Al atoms in the zeolite, reducing their exposure to water and impeding hydrolysis [51]. These processes are indeed used in commercial zeolite Y samples and the resulting catalysts are commonly referred to as ultra-stable Y, useful in industrial application for its structural integrity over time under harsh conditions.

Besides the structural stability ability of these external fragments, synergistic effects are addressed in the literature in regards of their catalytic activity and lifetime stability [52]. Due to the properties of these Al-OH bonds, EFAL can behave as strong Lewis and Brønsted acid sites providing different acidities than those found in the

framework-Al. However, such contribution relies on the type of EFAL present, its distribution and concentration, and the reaction conditions applied, requiring careful considerations in its use for the optimum catalytic performance.

Another problem associated with the higher concentration of active sites is the deposition of bulk carbonaceous species over the surface for their higher tendency of reaction and continuous oligomerization over the active surface, also known as coke [53, 54]. This coke reduces the catalytic activity by sterically inactivating that local site environment hindering the reactive proton [55]. Coking can be efficiently removed from a zeolitic surface through an oxidative treatment under flow in air, operated in optimal conditions to avoid structure collapse from that water produced by coke oxidation [56].

1.2.2 Zeolite MFI

In addition to zeolite Y, MFI, also known as ZSM-5, is also a small-pore zeolite with a three-dimensional structure consisting of interconnected 10-membered ring channels with a pore size of approximately 5.5 Å (**Figure 5**) [2]. Such small apertures finely select the types of molecules that can be adsorbed or catalyzed, preventing the formation of bulk molecules, which could cause a further decrease in activity. It can be found in several Si/Al ratios that balance catalytic activity and catalyst stability depending on the purpose for which it will be used. A result of a possible higher Si/Al, i.e., concentration of active sites, is the synergism between two proximate sites, responsible for activating a molecule to a certain extent or participating in the reaction mechanism, lowering the energy demand for that reaction to occur [57]. Such proximity is achieved during the zeolite synthesis [58].

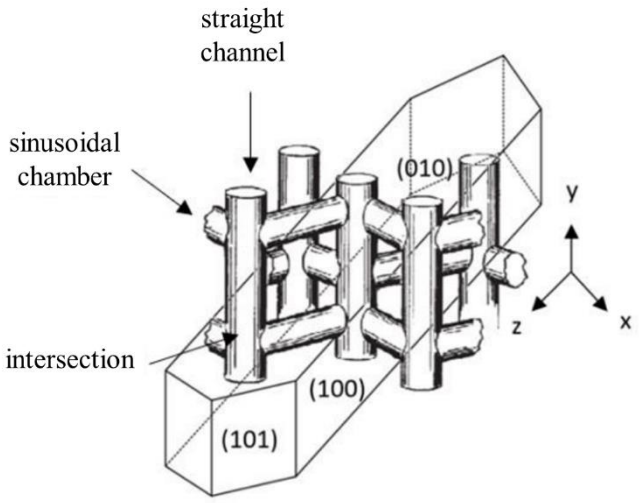

Figure 5: Perpendicular and regular channels in ZSM-5 lattice. Adapted from Ref [59].

The synthesis of MFI is complex and challenging compared to other zeolite syntheses due to the precise control of the reaction conditions and the use of specific SDAs to direct the crystallization growth to achieve the desired properties of that catalyst. Despite the significant progress that has been made in recent years in developing new experimental methods to improve the MFI synthesis with alternative SDAs, conventional methods utilize tetra propylammonium cation (TPA^+) as the most common SDA [60, 61]. Due to the positive charge in the center of this molecule and its placement within the intersection of the channels and cages of MFI, TPA+ can orient the Al atoms sitting at these positions, improving catalytic properties for some reactions [62, 63]. The use of inorganic salts can also guide the positioning of an acid site through the channels instead [64]. This aluminum positioning allows only certain transition state conformations and is selective towards specific products [63].

Another strong feature of MFI is its distinct confinement effect resulting from the constrained channels, leading to enhanced selectivity for certain types of reactions, such as

the selective conversion of methanol to olefins (MTO) and the isomerization of bulky hydrocarbons in petrochemicals [65-68]. This is a consequence of limiting the mobility and orientation of the molecules in the transition state while stabilizing them through van der Waals interactions with atoms in the framework Structure [69-71]. Consequently, the confinement effect is an important factor that contributes to the high catalytic activity and selectivity of MFI.

The unique properties of zeolites make them valuable materials that require continuous research focused on developing experimental approaches to modify existing structures to further enhance their adsorption and catalytic properties.

1.3 Diffusion Concepts on Porous Catalysts and its Importance on Catalyst Studies

In addition to the materials and reaction concepts presented, molecules diffusion inside porous systems is also necessary for the development of this study. Diffusion refers to the natural process of molecules transport from an area of high abundance of particles to a lower concentrated one aiming a more homogenous distribution along the control volume [72, 73]. This phenomenon is key to catalysis studies once the contact between the reactant and the reacting agent (catalyst) must happen for the reaction to occur. If one can control the rate in which these collisions happen, then one will be able to dictate the rate and the outcomes of a reaction.

Heterogenous catalysis is characterized by the difference phase between the reacting species (liquid or gas phase) and the catalyst (solid phase). The catalyst solid material is composed of a large surface area in which the reacting species diffuse through

to adsorb and thus react. In the case of zeolites, the reaction sites are predominantly concentrated inside the porous framework of the catalyst particle demanding reactants diffusion for reacting. However, the limited space created by the porosity environment can cause molecules to encounter difficulties in the transport process, these are known as diffusion or mass-transport limitations [34, 74, 75]. Such limitations directly affect the system performance overall for having a heterogenous reactant distribution along the catalyst volume and becoming rate-limiting.

Two types of diffusional limitations can be encountered in heterogenous catalysis [76]:

1) External diffusion limitations: defined as the difference in reactant concentration between the bulk phase and the outer reacting surface, caused by a flow resistance from that catalyst particle. Usually, this resistance occurs when flow and-or stirring conditions are insufficient enough to guarantee a concentration gradient between the phases. If a system becomes externally diffusion limited, increasing the gas-phase velocity, or the stirring speed of a reactor tank, or decreasing the particle size are ways to reduce transport limitations effects [77]. Because of that, mitigating its effect is relatively accessible as compared to internal diffusion limitations.

2) Internal diffusion limitations: characterized by low diffusivity of reactants inside the catalyst pores, it is derivative from either a small aperture of that zeolite pore or large size of the reacting species. Here, the reactant concentration in the outer surface of the particle is higher than that found in the particle center, exposing internal sites to different concentrations, and reporting a reaction rate that is actually

an average rate throughout the catalyst. In kinetic studies such events disturb the results and lead to inaccurate interpretations. Once this restraint is caused by the intrinsic properties of the catalyst and the molecules, diminishing it is complex and requires robust study. Yet, efforts have focused on the generation of mesoporosity in the catalyst particle or experimental synthesis approaches to obtain nanosized particles, which directly ties into the diffusion path of a reacting specie [78, 79].

Then, when a system becomes mass transfer limited the overall catalytic rate reflects the aspects of the molecules diffusion inside the catalyst particle, being influence by operational factors (e.g., flow velocity, reactant concentration, temperature, pressure, and others) as well as catalyst characteristics (e.g., pore size and geometry, catalyst particle size and shape). In general, the study of diffusion limitations in zeolites is essential for continuous improvement of the design and performance of zeolite catalysts, as well as advancing our understanding of complex chemical reactions in confined spaces.

Internal Diffusion Limitations Studies in Zeolites

The assessment of diffusion limitations in zeolites could be performed through many types of experimental approaches: (i) in-situ spectroscopy analysis, using infrared (IR) or Raman to observe molecules adsorption and desorption over zeolite surfaces [80-82]; (ii) pulse-response experiments, through regular injection intervals of a studied specie over the sample and monitor the concentration profile as it reaches equilibrium [83]; (iii) Mears criterion for external diffusion limitations and Weisz-Prater criterion for internal diffusion limitations on porous medias, both utilize operational and experimental data to evaluate a zeolite applicability for a particular system [77, 79, 84, 85]; and (iv) a direct calculation of Thiele-modulus, a reaction-transport parameters derived from a mole

balance of a reactant diffusing through a catalyst volume particle to describe the extent of diffusion constraint in a porous media [86-88].

In case of spectroscopy studies on diffusion, isooctane transport studies in ZSM-5 zeolite were performed by tracking IR signals attributed to that hydrocarbon as it was purged from the zeolite framework [89]. To do so, a commercially available ZSM-5 (SP) sample and a large-sized synthesized sample (LP) were treated under an alkaline environment to induce desilication and create mesoporosity in these two samples (SAP and LAP, respectively, based on their parent forms). After reaching a surface saturation, followed by purging, the relative surface concentrations were calculated based on IR bands correspondent to that isooctane normalized C-H stretching vibrations. The creation of mesoporosity in the desilicated samples was shown to alleviate diffusion constraints on isooctane, as demonstrated by its rapid desorption (**Figure 6**). Surely, the diffusion path of a molecule entering a catalyst particle and encountering an active site decreases as a consequence of such large channels, which is advantageous for bimolecular reactions and also reduces coke formation due to the lower residence time of a coke precursor species [90]. One application of isooctane in this study is its ability to serve as a hydrogen donor molecule to an adsorbed carbenium ion and how diffusion limitations impact this process [91, 92]. A larger concentration gradient of a H-donor specie results in lower local concentrations around the reacting site, and thus H-transfer rates to an adsorbed carbenium ion are reduced as consequence [93]. In the diffusion study performed by Meunier et al. the monitored temperatures during the IR spectroscopy experiments were low enough to guarantee no isooctane reaction, which suggests a research motivation in this area.

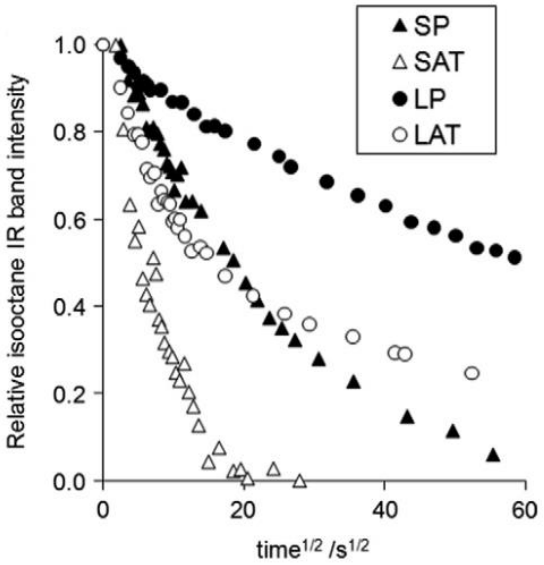

Figure 6: Desorption of isooctane at 428 K from small and large H-ZSM5-5 crystals in parent and mesoporous forms. Reproduced from Ref [89].

In all, the IR technique was shown to be useful and accessible in examining the presence of transport restrictions under a no-reaction regime; however, it could not determine the extent of such quantitatively. This quantification and comparison among different topologies could be realized using Thiele modulus once this parameter takes into consideration intrinsic properties of that certain catalyst (as particle radius and particle shape) and the reaction information at the applied operational conditions (effective diffusivity and reaction rate constant).

Noh's work observed differences in product selectivity as a function of increased diffusional constraints in the isomerization and β-scission reactions of n-heptane over various acid catalysts [17]. As the degree of diffusion limitations was increased, either by altering the density of active sites or the confinement environment, secondary isomerization rates increased to a point in where the smaller voids favored sequential β-scission events (**Figure 7**).

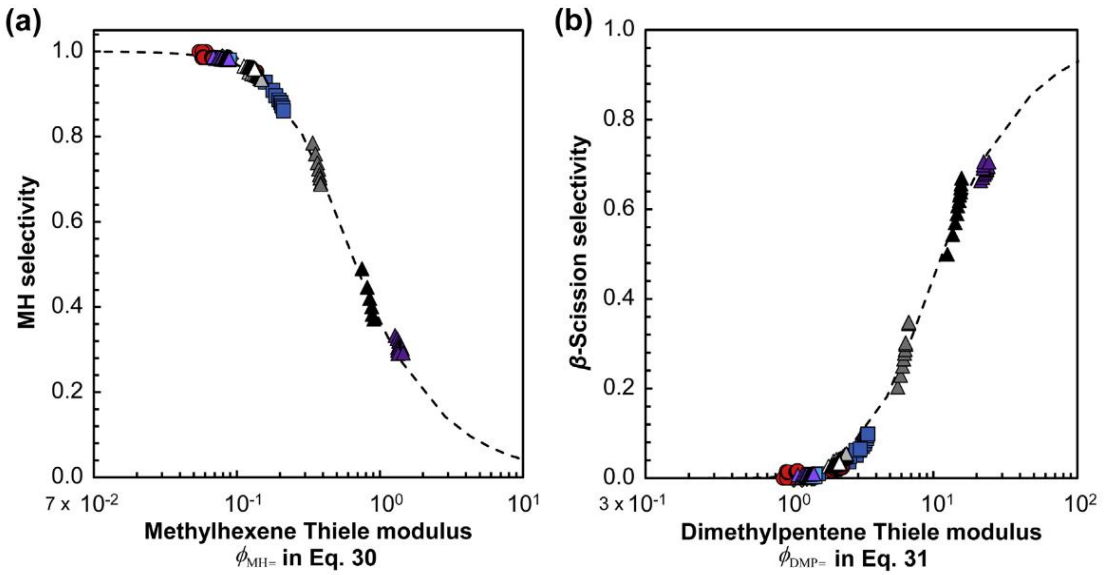

Figure 7: Measured selectivities to (a) methylhexane products as a function of the methylhexane Thiele modulus, ($\phi_{MH=}$) and (b) b-scission products as a function of the dimethylpentane Thiele modulus ($\phi_{DMP=}$) during nC7 isomerization on physical mixtures of Pt/SiO_2 and acid catalysts. Reproduced and adapted from Ref. [17].

The explanation relied on the higher intracrystalline residence time of molecules in those confined environments, as well as the stronger impact of van der Waals interactions between higher energy transition state species and the framework. Thus, the observed product selectivity shifts, favoring one product over the other, were a mere consequence of specific diffusional constraints rather particularities of preferential stabilization of transition states as zeolites changed. With this, by utilizing experimental approaches to tune a molecule transport inside of a solid acid catalyst not only these complex systems are comprehended but also designed for a specific application.

Overall, each approach has its strengths and disadvantages, and the choice depends on the specific research question and the available resources. Certainly, the impacts are not solely related to activity depreciation but also to outcomes relative to the lower transport of reactants and products inside these defined and constrained porous domains. For this,

organic reactions have been studied over zeolites for their large application in industrial processes involving esters, alcohols, and saturated and unsaturated hydrocarbons, and it will be discussed next.

1.4 Organic Reactions over Acid Catalysts

Organic reactions are chemical transformations that involve the breaking and forming of covalent bonds in organic compounds. These reactions are accelerated by the presence of a catalyst, which facilitates the reaction by lowering the activation energy required for the reaction to occur [94]. Acid catalysts, in particular, are widely used in organic reactions because of its ability in donating a proton to the reacting specie, enhancing the activity and promoting the formation of a desired product. By understanding the mechanisms of these reactions and the role of acid catalysts, scientists develop new and more efficient synthetic routes for the production of valuable organic compounds are developed. In the following paragraphs, aldol condensation and catalytic cracking will be explored in more details, exploring the reaction mechanisms and applications.

1.4.1 Aldol Condensation

Aldol condensation is a type of organic reaction that involves the carbon-carbon coupling of two carbonyl compounds, usually an aldehyde and a ketone, to form a β-hydroxy carbonyl compound, which is commonly referred to as an aldol [95, 96]. The aldol product contains both aldehyde and alcohol functional groups in its structure and can easily undergo subsequent dehydration forming an α,β-unsaturated carbonyl compound. This reaction is a powerful tool for the formation of C-C bonds and usually yields products with

higher stability, depending on specific functional groups and substitution patterns found in reactants and products.

In an acid-catalyzed reaction, the condensation mechanism initially involves the protonation of the carbonyl group to form an oxonium ion intermediate, commonly referred to as an enol. The electrophilic carbonyl carbon of the oxonium ion then undergoes a nucleophilic attack by a nearby ketone or aldehyde. The resulting intermediate, which is unstable, then undergoes dehydration and desorption. **Figure 8** presents a mechanism scheme to aid the process understanding.

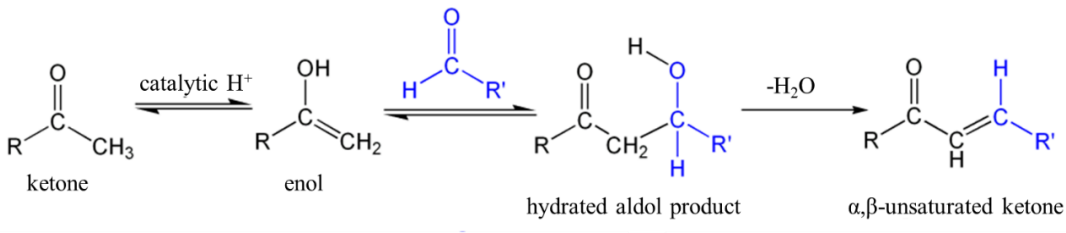

Figure 8: Acid catalyzed ketone aldol condensation reaction mechanism. An illustration.

The bimolecular characteristic of this reaction enables the C-C bond formation occurring between either identical reactants (self-aldol condensation) or different reactants (cross-aldol condensation) [97]. Determining factors such as carbonyl reactivity, molecule steric arrangement, feeding concentration, choice of catalyst and operational conditions, resolve the product selectivity distribution when two molecules are cofed together.

Li et al. conducted a study on the cross-condensation reaction between acetone and cyclopentanone using acid-functionalized mesoporous MCM-41 [98]. Based on experimental results and simulation analysis, the product distribution was found to be influenced by steric hindrance during C-C coupling, the electrophilicity of the adsorbed electrophile, and the acidity of α-C-H in the ketone. The most favored dimer product was

formed when adsorbed cyclopentanone reacted with a nearby acetone ([CPO]ACE) due to the greater stability of enol in cyclopentanone and less geometric interference of acetone. Increasing the Bronsted acid site density enhanced the rate of product formation but did not result in a change in the product distribution. This was attributed to the activation of a second ketone nearby an activated enol, facilitating the C-C coupling between the ketones.

1.4.2 Catalytic Cracking

Catalytic cracking is a reaction used to break down large hydrocarbon species into smaller molecules involving the use of a catalyst, generally a zeolite-based material. This process improves the energy value of the product (gasoline) from crude oil, minimizing waste and reducing the environmental impact of petroleum-based processes.

The cracking reaction mechanism is dependent on the nature of hydrocarbon that undergoes protonation. When an alkane is protonated, it results in the formation of a penta-coordinated carbocation, also known as a carbonium ion, which is highly unstable and prone to undergo protolytic cracking [99, 100]. This instability is attributed to the significant steric strains created by the five bonded atoms surrounding the positively charged carbon, leading to further rearrangement or C-C cleavage between the carbocation and the carbon adjacent to it. A resulting alkene molecule is generated together with an adsorbed carbenium ion. This later specie can desorb from the catalyst surface or receive a hydrogen atom from a nearby molecule, usually a large hydrocarbon which can sustain a carbocation in its structure. This reaction is known as H-transfer and it produces an alkane and a carbenium ion that remains on the catalyst surface; however, this reaction is only likely to occur when the local concentration of saturated hydrocarbons is high [93]. A termination step of this reaction chain is when the carbenium ion molecule donates a proton

and desorbs as an alkene. This reaction mechanism started from a carbonium ion specie is denoted in literature as protolytic cracking.

In the case an alkene is protonated, or an alkane serves as a H-donor specie, the resulting carbocation is a carbenium ion, which is a positively charged carbon with three bonds and a vacant fourth bond [93, 100]. This vacancy causes a high degree of instability, similar to the carbonium ion, making it a highly reactive and short-lived specie [99]. Analogous to protolytic cracking the carbon-carbon bond cleavage occurs between the carbocation and its adjacent carbon neighbor, resulting in a desorbed alkene and a carbenium ion specie that adsorbed in the surface. Depending on the nature of the reactant feed, H-donor species concentration around the site environment, and the carbenium ion surface coverage, H-transfer is likely to occur, or the carbenium ion may react with a nucleophile, losing its positive charge and terminating the reaction chain.

Figure 9 exemplifies the conventional understanding of the catalytic cracking of reaction pathways through a carbenium and a carbonium ion for a certain alkane molecule RH.

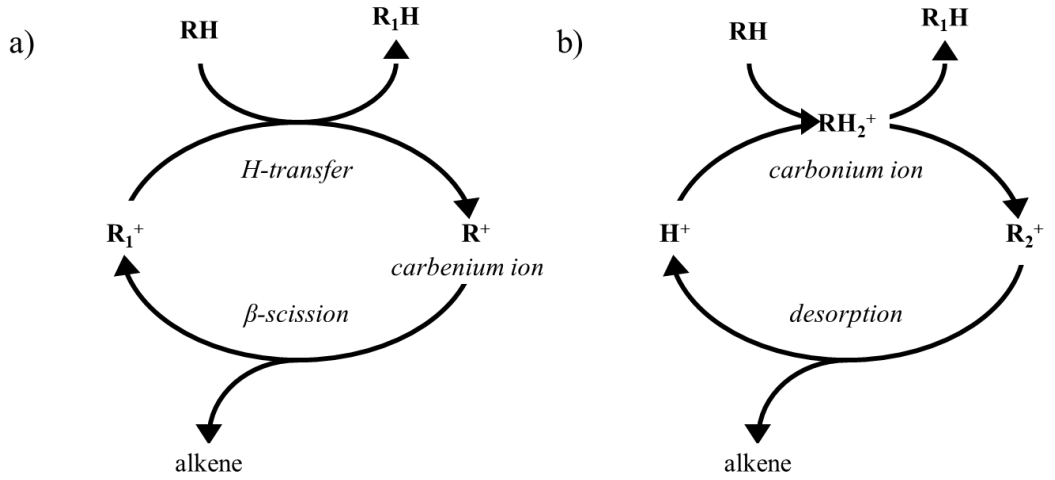

Figure 9: a) classical cracking mechanism for an alkane molecule (RH) consisting of a H-transfer step to an absorbed carbenium ion ($R1^+$ followed by β-scission; b) cracking mechanism for an alkane molecule (HR) proceeding via carbonium ion route. Adapted from Ref [101].

An important remark in regards of the H-transfer step is the stability of the resulting intermediate. Smaller molecules are less likely to donate a proton to an adsorbed carbenium ion for its instability in supporting a positive charge in its structure, instead, large and more substituted hydrocarbons are preferential to exert this functionality [102, 103]. Also, the presence of coking or bulk carbonaceous species serve as a hydrogen supply to these adsorbed species [104].

The catalytic cracking mechanism has received substantial attention in the past few decades, resulting in improved understanding of the process. However, due to advancements in computational methods and growing environmental concerns, efforts are still being made to fundamentally comprehend these reactions. By combining this knowledge with an awareness of diffusion constraints in porous catalysts, it is possible to not only improve the efficiency of cracking processes, but also to discern the factors that directly control reaction rates and product selectivity.

Research Objectives

Therefore, this dissertation will demonstrate four main works performed directly related to diffusion-reaction strategies used to optimize the understandings of diffusion implications around zeolites, coupling theoretical aspects and proposed experimental approaches to do so.

i) Identification and modeling development of mass-transfer limitations on zeolites through liquid phase self-aldol condensation reaction of acetone and cyclopentanone over zeolites Y and MFI. A focus on tuning the concentration of active sites of a catalyst through pre-treatment with inert-alkali species and an in-situ site deactivation with poison molecule.

ii) Implications of a regime transitioning in the cross-aldol condensation of acetone and cyclopentanone, an understanding of diffusion impacts.

iii) Particle size dimensions adjustment through zeolite synthesis and its reflection on liquid catalytic activity. Combining theoretical discussions on diffusion constraints with proposed experimental approaches.

iv) Impact of mesoporosity in zeolite Y and its resulting effects on isooctane cracking activity. Acknowledgment of synergistic sites and their functionality on cracking reaction routes.

Chapter 2 – Mass-Transfer Limitations Investigation using Liquid Phase C-C Coupling Aldol Condensation Reactions in Porous Catalyst Media

2.1 Introduction and Literature Review

Diffusion rates of reacting species inside of microporous frameworks can directly affect observed catalytic rates, selectivities, and even catalyst deactivation depending on the products formed and their residence time inside the particle. When pore size and acid site concentration were changed a shift in product selectivity was obtained in zeolite-catalyzed self-aldol condensation of acetone [105]. Those changes were due to secondary reactions of the products led by their high residence time within the microporous system, being the zeolite topography and site proximity the main elements to contribute to the shifts [17]. Once these differences on diffusional rates exists and influence, one can take advantage of confined environments and acidic characteristics to tune the resulting product selectivity based on size and shape differences in the reactant mixture. One example in is the (self/cross) aldol condensation reaction, a reaction used to elongate the C-chain of a molecule through eliminating the O-content while forming C-C bonds, forming stable and energetically valuable compounds [106-108]. This reaction is characteristic of ketone molecules as reactants, which are obtained through an upgrading of light oxygenates and sugar derived compounds, from biomass pyrolysis [109-112].

The aldol-reaction mechanism comprehension enables the understanding of reaction results in a single-feed and as more than one ketone is fed simultaneously. Each

molecule consists of particular details that are important for the diffusion-reaction comprehension within microporous-zeolites. The study over acid-catalysts has been widely reported in literature over different microporous and mesoporous catalysts [113-117]. The ketone is firstly activated with a simultaneous protonation and tautomerization step by an interaction between a surface proton and the O-atom of the ketone's carbonyl group [118]. The activated enol can be subjected to either an electrophilic attack on the C-atom from a nearby ketone that is either adsorbed (Langmuir-Hinshelwood mechanism) or in the bulk phase (Eley-Rideal mechanism) [119]. The formation of the C-C bond is followed by a concerted mechanism in where there is a proton transfer from the enol in the α-C to the O-atom of zeolite while the O-atom in the carbonyl receives the H from a Brønsted acid site (BAS) [120]. The product formed is quickly dehydrated to produce a α,β-unsaturated ketone that could undergo desorption or a sequential electrophilic attack, a secondary condensation reaction following the same elementary steps as the primary ketone. These elementary steps are shown in **Scheme 1**, in where the cyclopentanone was reacted over functionalized sulfonic acid groups in MCM-41 support, a mesoporous material. In regards of whether the kinetically relevant step is the tautomerization or the C-C coupling literature has reported that it depends on steric influences of both molecule and zeolite topology, and also the confinement over high-energy intermediate species [121, 122].

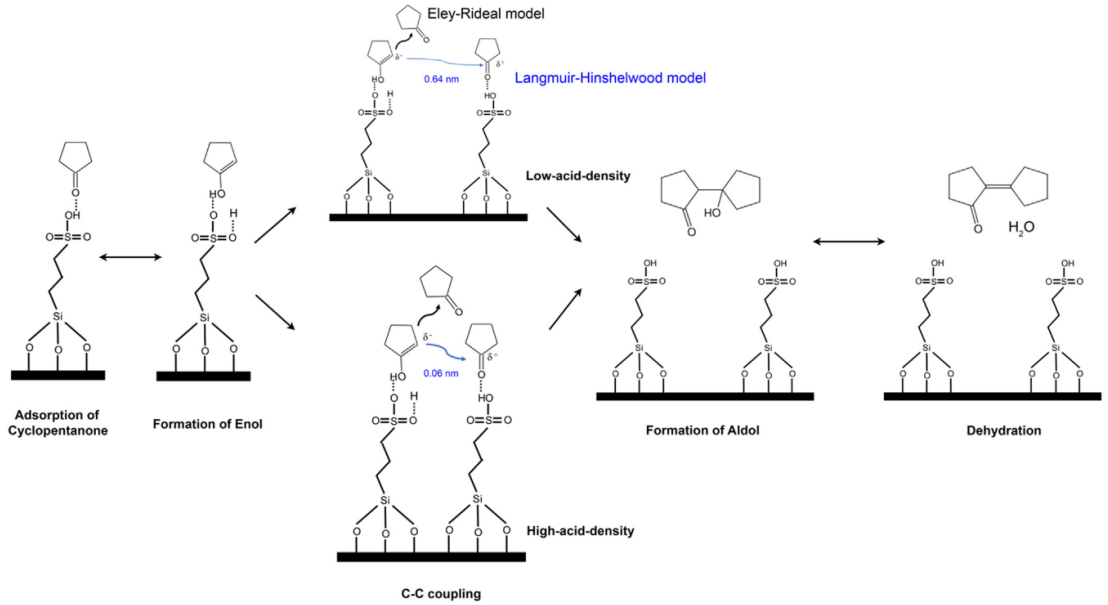

Scheme 1. Proposed mechanisms of CPO self-condensation based on Langmuir-Hinshelwood and Eley-Rideal models under water-free conditions. Reproduced from Ref [119].

These mechanistic studies are only meaningful when diffusion constraints are not governing the activity inside confined environments. It usually occurs when the dimensional magnitude of the molecule geometry and the material's apertures are analogous, raising a concern whether mass-transfer limitations (MTL) are present or not. To control and tailor the extent of MTL one needs to be able to quantify and precisely change the parameters that govern reaction and diffusion for a given reactant/zeolite system, as particle size or site activity on a catalyst. More than 40 years ago, Madon and Boudart developed an experimental test which compares the observed reaction rates per unit mass for porous catalysts of varying loading of active species – in that case Pt – at similar metal dispersions [123]. Accordingly, each catalysts contained a different concentration of active sites which should result in different reaction rates. The authors indicated that only when the ratio between the observed reaction rate and the density of exposed metal atoms, i.e. the turnover frequency, remains constant for all catalysts one

could conclude that mass-transfer limitations are absent. By contrast, if the turnover rate frequency (TOF) decreases as the number of sites increases, one can conclude that the inner active sites are not exposed to the same reactant concentration as the outer sites and the system is under MTL.

To investigate the presence and extent of MTL the present work implements two experimental approaches on acidic zeolite catalysts by adjusting the concentration of active sites and observing further effects on catalytic activity using the aldol condensation as model reaction. Starting with the proton-form of a zeolite, the density of active sites are varied with a gradual site deactivation through cation exchange, a catalyst pre-treatment prior to reaction, and an in-situ titration with a reaction inert molecule.

In literature Na-exchange has been used as a quick experimental test for MTL observance as described by the Madon-Boudart method [124-126]. Because of its smaller size compared to other cations in the same family group (K^+ and Rb^+, e.g.), Na accesses confined environments with smaller apertures in the zeolite framework generally not accessible for reactants, but that are able to partially activate/interact with the reacting species [127, 128]. This accessibility allows Na to deactivate acid sites and it is not lost during the reaction due to the chemical character of the species used in the reactions. Here said, reactants and solvents are organic molecules and thus will not extract and change the BAS density and the nature of active site itself. Literature has reported that Na preferentially titrates intrinsically more active sites within the crystalline framework, whether it going to more confined environments, or in positions within the structure that favors reactivity, or at pairs sites [127, 129]. One example is the work done by Lercher et al., a gradual addition of Na in MOR titrated the active sites and a resulting drop in the

infrared spectroscopy peaks relative to BAS happened. Two identified locations of BAS in the catalyst are at peaks for in 8-membered rings (MR) pockets (3590 cm^{-1}) and in 12-MR channels (3620 cm^{-1}) (**Figure 10**) [130]. With an increase in the Na concentration the BAS peak shifts towards high wavenumbers ascribed to those sites located in main channels of MOR (12-MR), showing a Na titration preference towards sites located at the MOR pockets [131, 132]. Those different site locations had a particular activity, being each of them responsible for distinct formation of products.

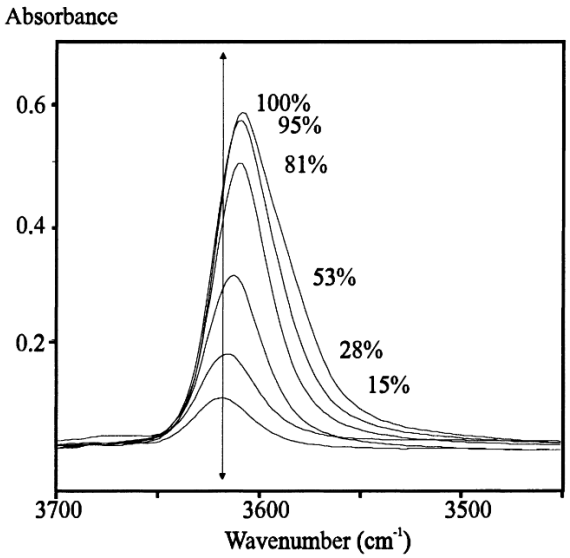

Figure 10: Spectra of hydroxyl region of various exchanged mordenites. Reproduced from Ref [130].

Parallel, pyridine is also used as a common probe to titrate Brønsted and Lewis acid sites in solid oxides and zeolitic materials [133-137]. This molecule is mainly recommended to titrate acidic materials due to its tendency to interact with surface protons, but once partially charged atoms serving as Lewis acidic spots are present over the catalyst surface a potential interaction with pyridine exists [138-140]. Due to that, the stoichiometry correlation belief of one added pyridine corresponding to one deactivated site is not true and its usage not recommended depending on the nature of the zeolite. The goal then is not

to use pyridine as a quantitively measurement for acid sites, rather its effect is solely analyzed as a titrant agent as its uptake increases inside the zeolitic structure. A molecule with an analogous capability could be used as an in-situ titrant: 2,6-ditertbutylpyridine. The spatial arrangement of both tertbutyl groups in the β-carbons of the amine group does not permit its interaction with a surface O-atom (i.e., Lewis acid sites), so its acid-titrant functionality in counting sites is more efficient when compared to pyridine, as observed in Baertsch's et al. work (**Figure 11**) [141]. The disadvantage relies on its size, usually facing diffusion limitations inside of confined frameworks and acting as a titrant only for those sites located in the outer surface of the catalyst particle [142, 143]. In summary, pyridine in confined environments seems to be a more appropriate molecule than 2,6-ditertbutylpyridine for in-situ acid titration even with its secondary function as Lewis acid site titrant, as well as the use of Na for the ion-exchange.

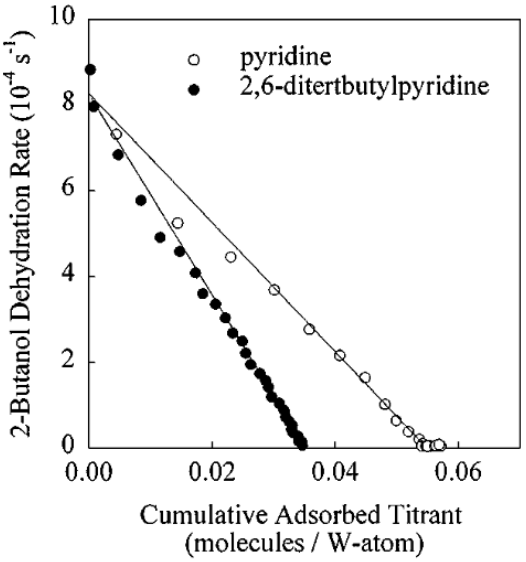

Figure 11: Catalytic titration of W30Z-14.8: 2-butanol dehydration rate as a function of the cumulative amount of titrant (2,6-di-tert-butyl-pyridine or pyridine) adsorbed during reaction. Reproduced from Ref [141].

It is expected that as the titrant amount increases, more sites will be inactive, and a continuous catalytic activity decay occurs. In the absence of MTL a linear decrease in

reaction rate is observed [125]. In this case, each site is exposed to the same reaction conditions and maintain an identical catalytic activity. Any modification over the site concentration will thus cause a proportional change in reaction rate. Contrarily, if MTL are present it is expected a non-linear decrease in rate with increasing number of titrates sites linear. As the majority of active sites have been titrated the variation approximates to linear since the concentration of remaining active sites is low-enough and most of the sites are exposed to equivalent conditions inside the crystalline framework. In order to prove the presented hypothesized rate behavior and to be able to identify quantify the extent of MTL at zeolitic systems, this study objectives to perform a set of experimental approaches by adjusting the initial site density of a catalyst and observing the respective rate drop. For this, a reaction-diffusion modeling is necessary to replicate the experimental results and allow such direct comparisons among different systems.

2.2 Reaction-Transport Modeling

To model and analyze the effect of diffusion limitations over the reaction rate a reaction-diffusion mole balance is done over a catalyst particle for a model reacting specie A. Here, the particle is considered to be spherical in all cases and the species diffuse radially within the particle channels and not in the polar and azimuthal coordinates. **Figure 12** illustrates a differential volume within a catalyst particle sphere that is integrated from the outer surface (r = R) to the center of the particle (r = 0).

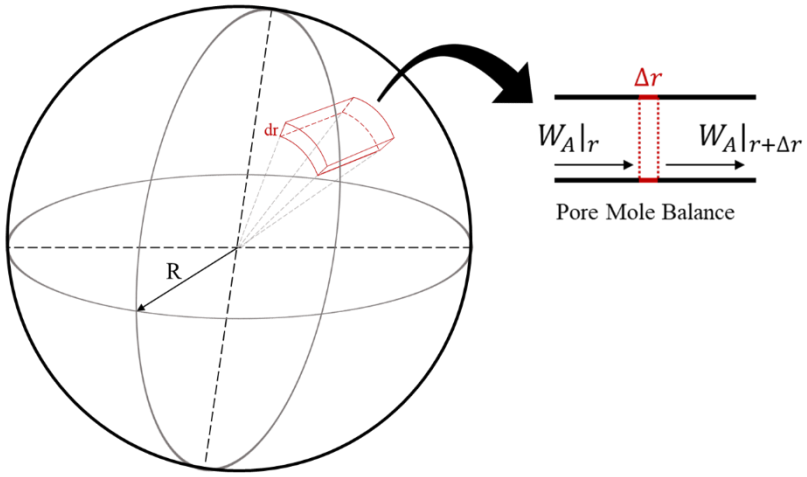

Figure 12: Catalyst spherical controlled volume description. Draw by the author.

In a differential volume a specie mole balance inside the spherical particle takes into account:

$$Accumulation = In - Out + Reaction$$

Each term has its own respective equation based on its nature. No accumulation exists and only diffusion and reaction occur along the the catalyst.

$$0 = W_{Ar} 4\pi r^2|_r - W_{Ar} 4\pi r^2|_{r+\Delta r} + r_A 4\pi r^2 \Delta r \qquad \div 4\pi\Delta r$$

$$0 = \frac{(W_{Ar}r^2|_r - W_{Ar}r^2|_{r+\Delta r})}{\Delta r} + r_A r^2$$

W_{Ar} is the diffusion flux of a component A in the particle according to the First Fick's law equation [73] , and r_A is the reaction rate equation of a component A. As the differential volume is approximate to zero (i.e., $\Delta r \to 0$), a differential form from the equation above appears.

$$0 = -\frac{d(r^2 W_{Ar})}{dr} + r_A r^2$$

According to the first Fick's law of diffusion equation, the flux is proportional to the negative of the effective diffusion coefficient of a component, multiplied by the concentration gradient of that component, along the diffusion path.

$$\text{Fick's first law of diffusion flux: } W_{Ar} = -\mathcal{D}_e \frac{dC_A}{dr}$$

The equation can be simplified and rearranged to be in a second order differential equation:

$$\frac{d\left(r^2 \mathcal{D}_e \frac{dC_A}{dr}\right)}{dr} + r_A r^2 = 0$$

$$\mathcal{D}_e \frac{d\left(r^2 \frac{dC_A}{dr}\right)}{dr} + r_A r^2 = 0$$

$$\frac{d^2 C_A}{dr^2} + \frac{2}{r}\frac{dC_A}{dr} + \frac{r_A}{\mathcal{D}_e} = 0$$

In order to be able to numerically solve this equation and for simplification purposes a first order reaction rate dependence on specie A (reactant) concentration will be used and dimensionless adjustments done. If needed, further modifications will be taken in the equation as the research results presents different considerations than those adopted. Assuming a first order type of reaction ($r_A = kC_A$), C being the dimensionless

concentration variable for A ($C = C_A/C_{A\,max}$; in where $C_{A\,max}$ is the A concentration at the outer particle surface), and λ, the dimensionless form of the radius ($\lambda = r/R$), the equation can now be resolved as follows:

$$\frac{d^2(CC_{A\,max})}{d(\lambda R)^2} + \frac{2}{(\lambda R)}\frac{d(CC_{A\,max})}{d(\lambda R)} + \frac{k(CC_{A\,max})}{\mathcal{D}_e} = 0$$

$$\frac{C_{A\,max}}{R^2}\frac{d^2C}{d\lambda^2} + \frac{2C_{A\,max}}{(\lambda R^2)}\frac{dC}{d\lambda} + \frac{C_{A\,max}kC}{\mathcal{D}_e} = 0$$

$$\frac{1}{R^2}\frac{d^2C}{d\lambda^2} + \frac{2}{(\lambda R^2)}\frac{dC}{d\lambda} + \frac{kC}{\mathcal{D}_e} = 0$$

And in order to become a first order differential equation, C' is considered accordingly, which is the dimensionless concentration gradient of A:

$$C' = \frac{dC}{d\lambda}$$

The final dimensionless reaction-diffusion equation is:

$$\frac{dC'}{d\lambda} + \frac{2}{\lambda}C' - \frac{kR^2}{\mathcal{D}_e} = 0$$

The last term in the equation is as Thiele modulus, a diffusion-reaction parameter used to evaluate the degree of diffusion constraint to which a molecule is subject in a confined environment; other way of interpreting it is the ratio of reaction rate and its diffusion along the catalyst particle [76]. For a reaction rate with a first order dependence on a specie A, Thiele modulus is represented by:

$$\phi^2 = \frac{kR^2}{\mathcal{D}_e}$$

Once the reaction constant is directly proportional to the density of active sites (L), any site modification will result in a change in Thiele modulus, as represented in the equation below.

$$\phi = \phi_0\sqrt{L/L_0}$$

where ϕ_0 is the original (or initial) Thiele modulus for the total number of sites (L_0), and ϕ the new Thiele modulus as sites are changed.

In the presence of a concentration gradient, that is, mass-transfer limitations, two reaction rates will coexist: a measured rate and a maximum rate. The last is the rate defined as the rate if all the sites were exposed to the same reaction conditions in the catalyst particle, e.g., the reaction rate found if no mass-transfer limitation exists. As the system distances from a system without mass-transfer limitations, more the measured rate distances itself from the maximum rate. The ratio between the two is understood to be the effectiveness factor (η), which also is expressed in terms of Thiele modulus:

$$\eta = \frac{r_A}{r_{max}} \qquad\qquad \eta = \frac{3(\phi \coth \phi - 1)}{\phi^2}$$

The last is resolved for a spherical catalyst particle. **Figure 13** shows a graphical correlation between η and ϕ [76]. Higher the Thiele modulus, lower the effectiveness factor. As the density of acid sites decreases a consequent decrease in ϕ occurs and a resulting increase in η.

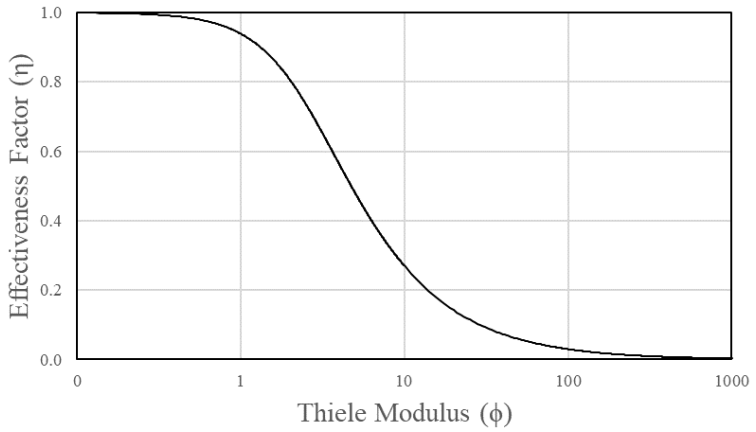

Figure 13: Graphical correlation of effectiveness factor as Thiele modulus changes in a spherical catalyst particle. Generated by the author.

It is expected that a combination of the presented equations offers a solution to find the Thiele modulus of a specific system as the concentration of active sites is changed within a particle catalyst. For this reason, the final dimensionless form of the first order differential equation that will be used in the reaction rate modeling is:

$$\frac{dC'}{d\lambda} + \frac{2}{\lambda} C' - \phi^2 = 0$$

Once it is experimentally easier to modify the site concentration through site titration, two models are proposed to represent the way sites are deactivated as the poison specie is added: a Uniform Titration model and a Shrinking Core Titration model. The Uniform model consists of a homogeneous distribution of titrant along the spherical catalyst particle, causing a proportional decrease in site density along the whole catalyst volume. Whereas the Shrinking Core considers a shell type of site titration, decreasing the active volume radius as the uptake occurs. The outer sites are first deactivated, resulting in an exterior dead shell volume composed of a diffusion component only, and an inner volume with an invariant site density compared to its free-of-titrant state but with a smaller radius compared to its non-modified form (**Figure 14**).

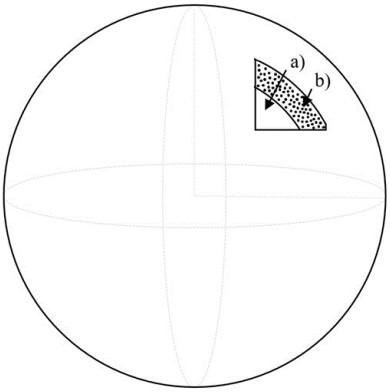

Figure 14: Image representation of a titrated catalyst particle with an inner active volume (‘*a)*’) and deactivated volume (‘*b)*’). Drawn by the author.

Mathematically, both models utilize the same final dimensionless form of the mole balance throughout the catalyst particle. The difference resides during the numerical integration. In Uniform model the Thiele modulus is altered as a function of the decrease in active site density, and the integration occurs along the entire catalyst particle, with the diffusion-reaction terms through the entire range of integration. In Shrinking Core, Thiele modulus changes as a function of the particle radius only, and the integration is divided in two regions: the first is comprised of diffusion only in the "*dead*" volume ($\phi = 0$, e.g. no reaction), and a following second volume which is active with an unchanged site density but the a lower radius. The radius is calculated based on the percentage of active sites remained after titration ($r = R\sqrt[3]{\frac{L}{L_o}}$).

In a regime free of diffusion limitations, e.g. $\phi \to 0$, no concentration gradient exists ($dC/d\lambda = 0$) and the variation of $\frac{r}{r_{\max\, at\, L_o}}$ as a function of the density of titrated sites is a decreasing straight line, i.e. constant TOF, as described by the Madon-Boudart criterion [123]. However, as such limitations are present, a non-linear decay in rate takes place. The effectiveness factor is calculated based on an initial guess on r_{max} and adjusted by decreasing the error between the modeled and the experimental reaction rate. Thiele modulus changes respectively as a function of both η and site density.

The numerical integration resolution is constituted of two boundary conditions for both models:

1st: $C'|_{\lambda=0} = 0$;

2nd: $C|_{\lambda=1} = 1$.

In words, the first considers no concentration gradient in the particle center, and the second affirm a unit value for the dimensionless reactant concentration ($C_A|_{R=1} = C_{A\,max}$) at the particle outer surface ($r = R$). The last agrees that no external diffusion limitations are present in the system. **Figure 15** shows the rate decay profile for both titration models as a function of percentage of titrated sites. The Shrinking Core model shows a sharp drop in rate even with a system with no MTL, not observed by Madon-Boudart and also in other works in literature. One might expect the Uniform type of titration, but the second model is considered and mentioned for research purposes. As observed, the two models has a different rate decay with or without titration which can be easily identified by plotting the experimental catalytic results as a function of titrant uptake. Thiele modulus is later calculated and optimized by using the proposed models.

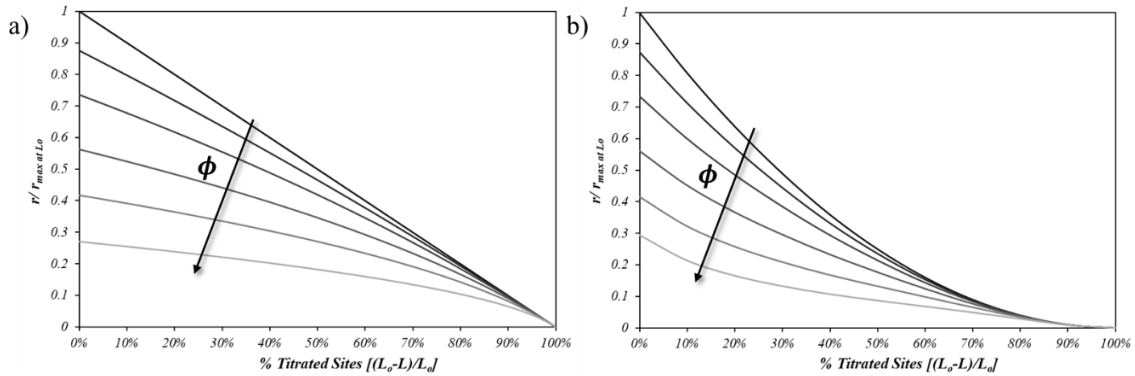

Figure 15: Reaction rate profile as a function of titrant uptake for Uniform Titration model (‘a)’) and Shrinking Core model (‘b)’). Generated by the author with representative values for Thiele modulus.

2.3 Experimental Methods

2.3.1 Chemicals and Materials

The zeolites used were obtained directly from Zeolyst International in their NH_4^+-form and used after thermal pre-treatment: ZSM5 (CBV 28014, Si/Al=140, and CBV 8014, Si/Al=40) and Y (CBV 760, Si/Al=30). The catalysts will be denoted here and on as Z140 (ZSM5 Si/Al=140), Z40 (ZSM5 Si/Al=140) and Y30 (Y Si/Al=30). All chemicals were purchased from Sigma Aldrich and used as provided: cyclopentanone (>99%), acetone (HPLC grade, >99%), cyclohexane (HPLC grade, 99.9%), phenol (>99%), pyridine (>99%), and sodium nitrate.

2.3.2 Catalyst Preparation

To obtain the proton form of the two zeolites, calcination of the ammonium form samples was performed at 550 ^oC for 5 h in 150mL/min air flow. A series of partially Na-titrated samples were obtained from each of these proton form zeolites by conducting Na-exchanges at varying concentrations. In each case, the parent H-Y or H-ZSM5 zeolite was exposed to a solution containing different $NaNO_3$ concentrations at room temperature for 1 h. Then, the exchanged sample was washed with deionized water and dried overnight in a vacuum oven at 80 ^oC. To reach higher levels of exchange avoiding Na precipitation and pore plugging some samples were subject to sequential exchanges. In these cases, intermediate calcination steps were performed at 300 ^oC to remove excess of water and impurities before the following exchange.

2.3.3 Site-density Quantification

BAS density of each zeolite was obtained through the temperature programmed decomposition of adsorbed isopropyl-amine (IPA-TPD). Such technique relies on the

stoichiometry adsorption of one IPA into one active site. At high temperatures IPA undergoes through Hoffman elimination and propylene leaves as one of the products (**Figure 16**). By using a mass spectroscopy (MS), one is able to track the propylene amount as a function of temperature (or time).

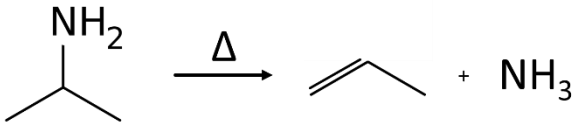

Figure 16: Isopropyl amine Hofmann elimination reaction representation.

The procedure consists of pelleting the catalyst and placing between two fine glass wool beds in a ¼" diameter quartz tube. In-situ pre-treatment was performed at 300 ^{o}C for 2 hours followed by cooling down to 100 ^{o}C. 2 μL IPA injections were done until the IPA signal at MS program remained unchanged. Temperature ramp-up occurred from 100 ^{o}C until 550 ^{o}C at a rate of 10 ^{o}C/min. Propylene signal was recorded and used to calculate the respective site density after following calibration.

2.3.4 X-ray diffraction Characterization

Crystalline pattern of the commercial samples were conducted on an XRD unit, D8 Series II X-ray diffractometer BRUKER AXS, in reflection geometry using CuKα radiation generated at 40 kV and 35 mA in the 2θ = 2-70° diffraction angle range.

2.3.5 Particle Size Measurements

The particle size estimations were done using a Scanning Electron Microscopy (SEM) analysis, conducted in a Zeiss NEON 40 EsB Field-Emission Scanning Electron Microscope at an accelerating voltage of 5 kV.

2.3.6 Catalytic Reaction Measurements

Catalytic reactions were conducted in the liquid phase in a Mini-Bench Top Parr high-pressure reactor (Model Parr 4565) equipped with a Parr 4848 reactor controller (**Figure 17**). Initially a specific amount of catalyst was placed with the solvent (cyclohexane) into a stainless-steel vessel and heated up to the desired temperature. Amounts relative to 1 mol of reactant (acetone and/or cyclopentanone) per liter of reaction solution was injected from a feeding cylinder when the reaction temperature was reached (200-250 ^{o}C) maintaining a constant reaction pressure of 700 psi using inert N_2 for the purging step. The time zero of the reaction period was then started. Conversion was kept low (<10%) to avoid secondary reactions and minimize equilibrium effects. Composition after reaction was determined both qualitatively and quantitatively using a combination of gas chromatograph-mass spectroscopy (GC-MS) and gas chromatography flame ionization (GC-FID).

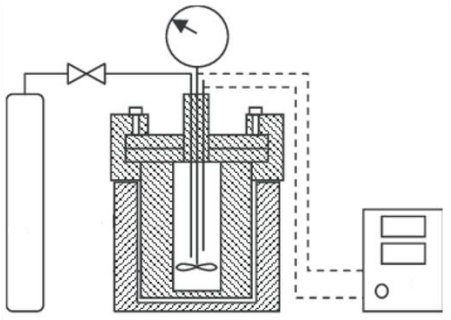

High Pressure Batch Reactor – Liquid Phase

Figure 17: Graphical representation of a high pressure batch reactor used for the catalytic measurements.

In all catalytic runs, each reactant and products concentrations were calculated based on a direct calibration using an external standard (phenol). For this, prior to the reactions, solutions containing different concentrations were generated with a similar amount of phenol and analyzed at the GC-FID. Correspondent linear correlations between

concentration and area were found for each compound and further reaction calculations were performed. The reaction rates (r_{exp}), conversion of reactants (X) and carbon balance (CB) were calculated as follows:

$$r_{exp} = \frac{n_{react}}{t * m_{cat}} \left[{mmol}/{g_{cat}.s} \right] \qquad X = \frac{n_{react}}{n_{tot\ ini}} [\%]$$

$$CB = \frac{(n_{non\ react} + n_{react})}{n_{tot\ ini}}$$

n_{react}: number of mols of reactant in products;

$n_{non\ react}$: unreacted number of mols of reactant;

$n_{tot\ ini}$: initial number of mols of reactant fed to the system;

t: time (s);

mcat: mass of catalyst (g);

$$n_{react} = (2 * C_{dimer} + C_{trimer}) * V_{tot}$$

C_{dimer} & C_{trimer}: calculated concentration of dimer and trimer formed in the self-aldol condensation reactions;

V_{tot}: total reaction volume.

2.4 Results and Discussions

2.4.1 Catalyst Characterization

2.4.1.1 Electron Microscopy and X Ray Diffraction

SEM pictures were taken in order to observe existing particle size differences between the studied zeolites and through **Figure 18** the calculated average particle size for the commercial samples were 0.8 µm in zeolite Y30 to 0.5 µm in Z40, and 1.3 µm in Z140.

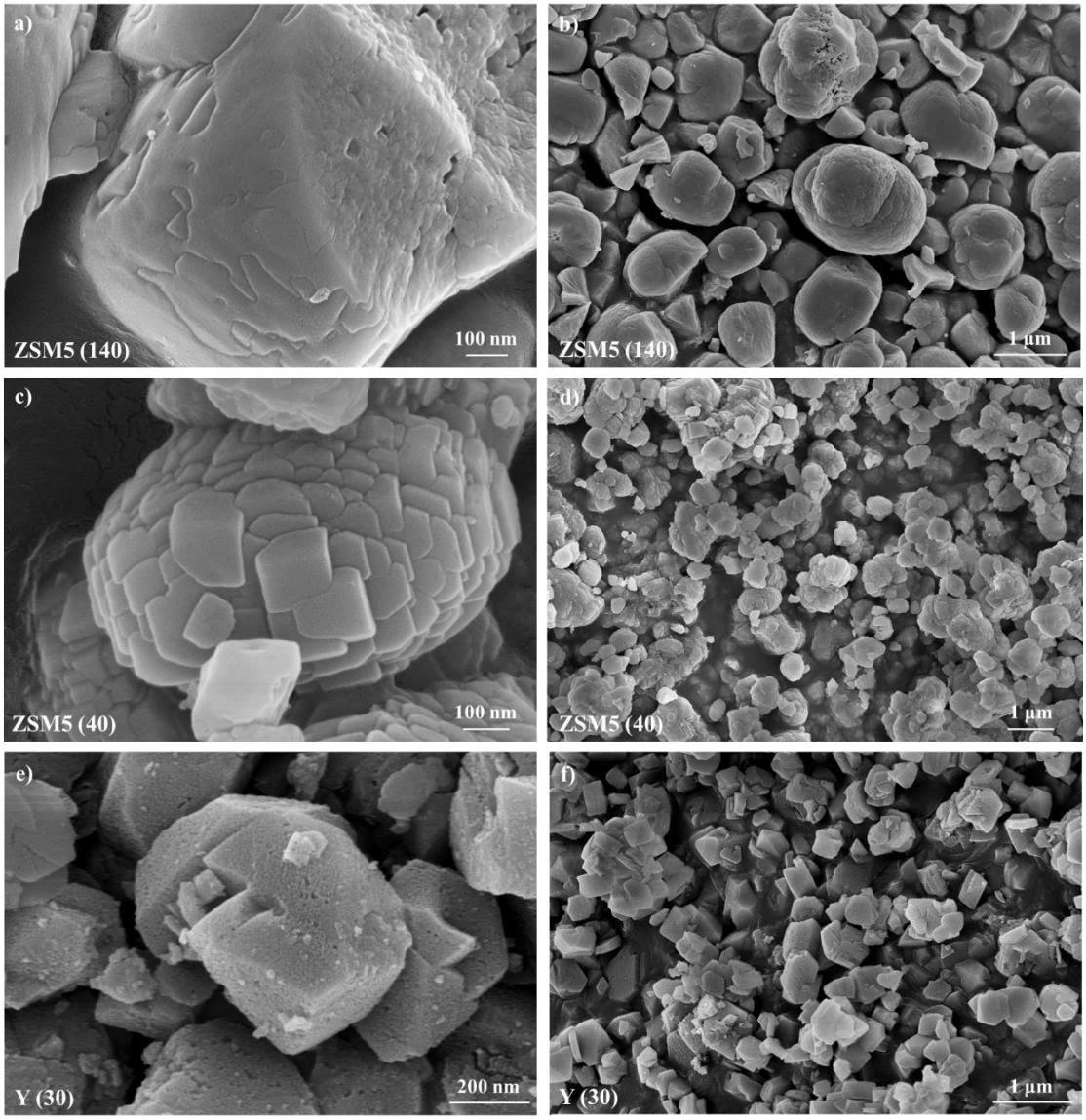

Figure 18: Scanning Electron Microscope pictures of ZSM5 (Si/Al) 140 ('*a)*' and '*b)*'), ZSM5 (Si/Al) 40 ('*c)*' and '*d)*') and Y (Si/Al) 30 ('*e)*' and '*f)*'). In which *a), c),* and *e)* are high magnification pictures, and *b), d),* and *f)* are low magnification pictures.

The Z40 picture at high magnification (**Figure 18.c)**) resembles a large particle resulted from an aggregation of small particles. One way to validate such assumption is to calculate the crystal size of a specific sample using the Scherrer equation, which requires the XRD spectrum of the sample and a standard pattern for that crystallography that is under study. A ZSM5 was synthesized with a large particle size (~30 μm) using a similar procedure as described in conventional methods [144]. The calculated crystal sizes for Z140 and Z40 based on their XRD spectra (**Figure 19**) are 265 and 115 nm respectively, different values than the "aggregates" observed in the SEM pictures and with those found in literature [145, 146]. With these calculation results and the high magnification images in **Figure 18** (***a)***, ***c)***, and ***e)***) it seems that each particle is a unique crystal rather than an aggregate of small ones and that the Scherrer equation fails to precisely calculate the crystal size of the used samples. To also support the assumption of a single large crystal, it is found in literature a transmission electron microscopy image of the commercial ZSM5 of Si/Al 140 and no particle aggregation is observed [147].

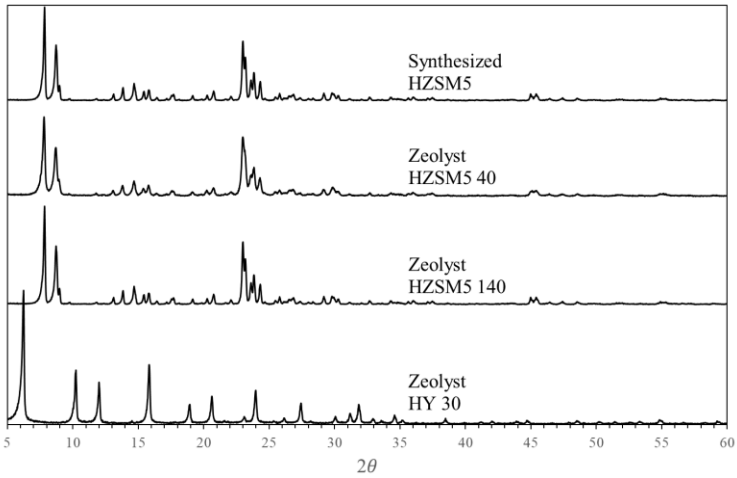

Figure 19: X-ray diffraction patterns for the synthesized ZSM5 and commercial samples of ZSM5 and Y zeolites.

2.4.1.2 Density of Acid Sites Quantification

The BAS density of each sample was obtained by IPA-TPD by quantifying the amount of propylene evolution from the fully saturated samples. **Figure 20** shows the MS signal corresponding to propylene as a function of temperature for IPA-covered samples of each parent and Na exchanged zeolite. Clearly, the amount of propylene adsorbed decreases as the number of Na-titrated sites increases. **Table 1** summarizes the BAS density (in mmol/g_{cat}) obtained for each sample where Na/H stands for the molar ratio of Na added into the exchange solution and each active proton in the parent zeolite. For high Na loadings sequential exchanges were performed to avoid pore plugging. [148].

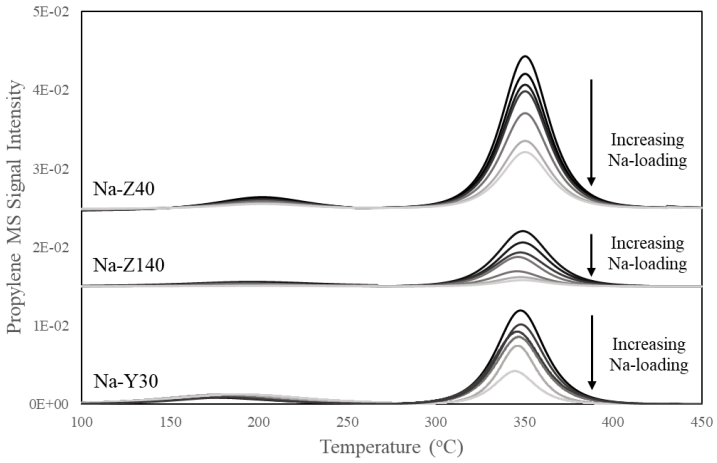

Figure 20: Temperature programmed decomposition of adsorbed isopropylamine (IPA-TPD) on the two Na-partially exchanged series of ZSM5 and Y zeolites. Propylene evolution in a 10 K/min heating ramp from IPA-saturated samples.

Table 1: Bronsted acid site density of Y and ZSM5 partially Na-exchanged series.

Na/H	IPA-TPD BAS (mmol/gcat)	Na/H	IPA-TPD BAS (mmol/gcat)	Na/H	IPA-TPD BAS (mmol/gcat)
Y30	0.23	Z140	0.10	Z40	0.40
0.4	0.20	0.4	0.09	0.1	0.35
1.7	0.17	0.8	0.08	0.2	0.33
5.2	0.15	1.2	0.07	0.5	0.31
13	0.11	2	0.06	2.5	0.25
43	0.06	9.6	0.04	2.5-2x	0.18
	-	9.6-2x	0.01	2.5-3x	0.15

2.4.1.3 Reaction Order

To accurately estimate the Thiele modulus, the reaction order with respect to the reactant concentration must be known. Therefore, catalytic rates were measured as a function of reactant concentration in Z140 and Y30. As shown in **Figure 21**, first order kinetics is observed in the range of concentrations for both zeolites. These two catalysts and reactants were chosen considering the nonexistence of MTL. However, even in the presence of MTL the observed order has a direct correlation with the true reaction order according to the following expression: $n_{observed} = \frac{n_{true}+1}{2}$ [76]. That is, if the observed order is 1 then the corresponding true reaction order is 1 as well. Thus, all the modeling here is conducted using a first-order reaction kinetics in respect to the reactant concentration.

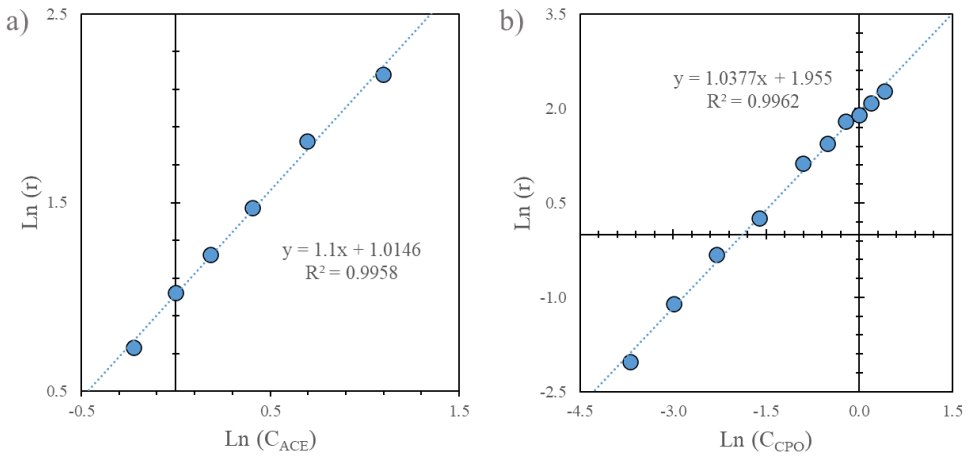

Figure 21: Natural logarithm of ketone consumption rate (r = [μmol/g_{cat}.s]) as a function of the natural logarithm of initial reactant concentration (C_{CPO} = [mol/L]); a) acetone condensation on zeolite H-Z140 and b) cyclopentanone on H-Y30.

2.4.2 Catalytic reaction measurements and assessment of MTL in Self-Aldol Condensation

2.4.2.1 Na-Titration

HZSM-5 (Si/Al 140) zeolite: **Figure 22** compares experimental rates of self-condensation of acetone (ACE) or cyclopentanone (CPO) per gram of catalyst on Z140 with varying Na loading, as measured in a liquid-phase batch Parr reactor at 250°C, using cyclohexane as a solvent at an initial reactant concentration of 1 mol/L. As expected, the observed rate decreases from the original sample to zero when the number of sites titrated by Na reaches the total number of acid sites (L_0). As mentioned above, only in the absence of MTL and for a sample with uniform activity in all sites one would expect a linear decrease. By contrast, a nonlinear decrease would indicate the presence of MTL [123]. Indeed, for the Z140 series, the reaction with the smaller reactant (ACE) exhibits a linear trend, but a slight deviation from linearity for the larger reactant (CPO).

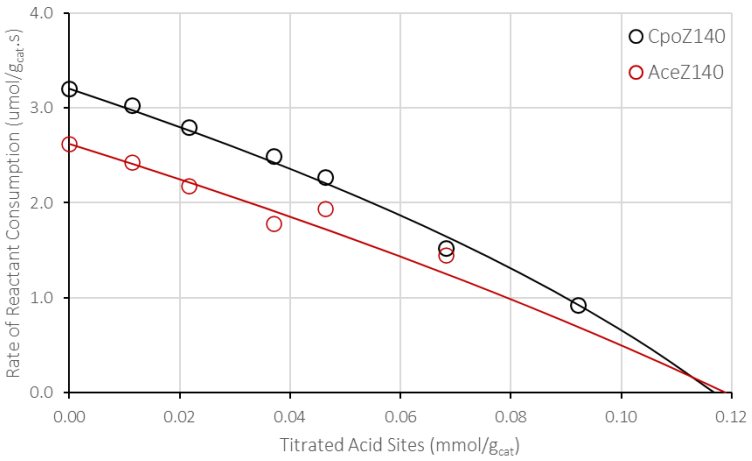

Figure 22: Self-condensation rates of CPO and ACE as a function of titrated site density in series of Na-exchange ZSM5 zeolite with Si/Al of 140. The lines represent the modeled profiles for each self-condensation result.

In regards of the amount of Na fed to the mixture prior to the exchange, high loadings as 0.25M and 0.50M of Na (Na/H = 50 and 100, respectively) will cause pore plugging and consequent lower activity as observed in **Figure 23**. Longer exchange times were performed to observe such effect.

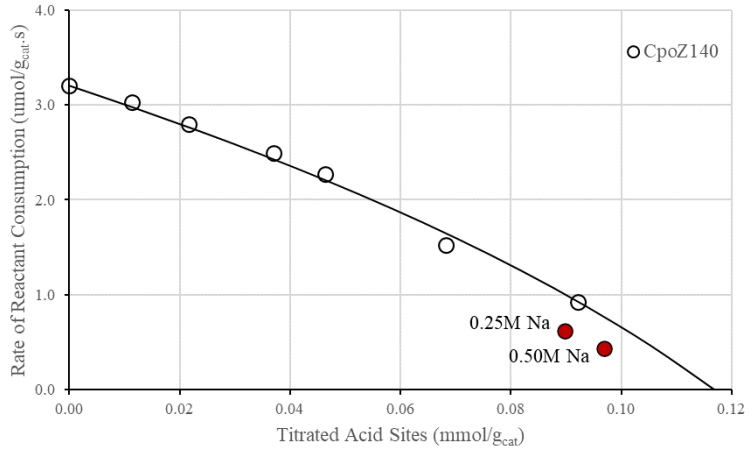

Figure 23: High Na-loadings exchanged samples in comparison with simulated trend in cyclopentanone self-aldol condensation in Z140. The line represents the modeled profile for the self-condensation result for cyclopentanone only.

HZSM-5 (Si/Al 40) zeolite: Analogously, **Figure 24** shows the self-condensation catalytic results over Z40 with different Na-titration levels. Again, CPO showed to

have a higher activity compared to ACE in the MFI structure. A more pronounced non-linear behavior was observed for both ketones when reacted in the presence of higher concentration of active sites, indicating a great effect of MTL. Here, high levels of titration were not obtained even with sequential Na-exchanges.

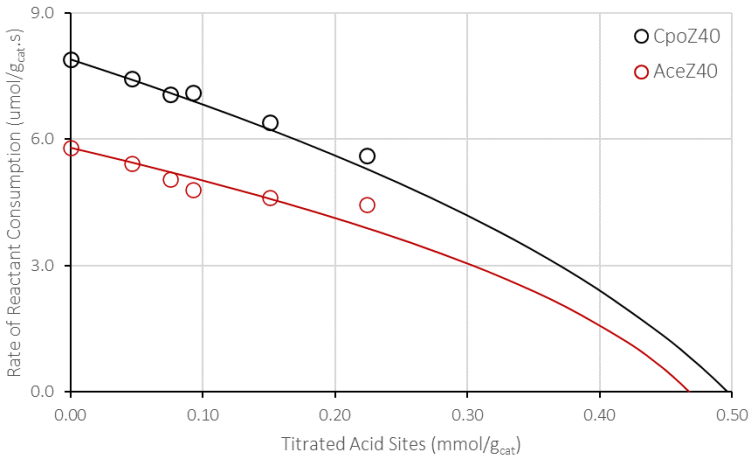

Figure 24: Self-condensation rates of CPO and ACE as a function of titrated site density in series of Na-exchange ZSM5 zeolite with Si/Al of 40. The lines represent the modeled profiles for each self-condensation result.

HY (Si/Al 30) zeolite: A similar set of experiments was conducted on six HY samples titrated with varying Na loadings. **Figure 25** shows the variation of self-condensation rate on the NaHY catalyst series as a function of density of sites titrated with Na, starting with the unmodified HY. Interestingly, in this case, contrary to the trend observed with the ZSM-5 zeolites, the observed rate for CPO is lower than that for ACE. The rate drop for CPO self-condensation is linear with increasing density of titrated sites, indicating the absence of MTL. While it is expected that the diffusivity of CPO is lower than that of ACE, it is possible that, contrary to the case of the ZSM5 zeolite, the intrinsic rate of CPO self-condensation is much lower than that of ACE.

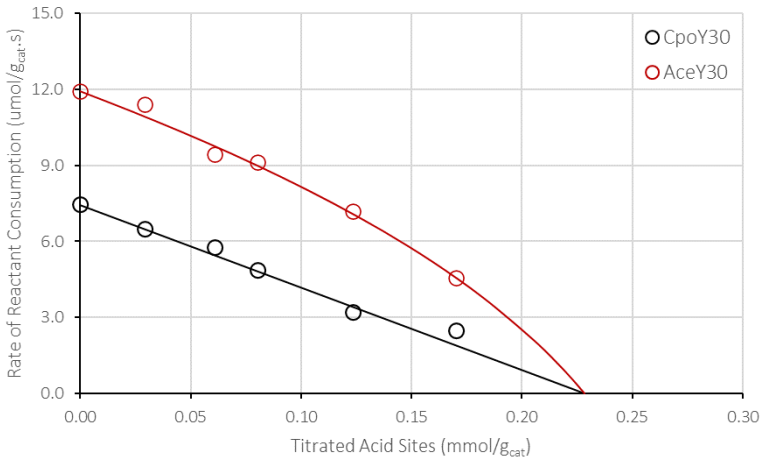

Figure 25: Self-condensation rates of CPO and ACE as a function of titrated site density in a series of Na-exchange FAU zeolite. The lines represent the modeled profiles for each self-condensation result.

2.4.2.2 Quantifications of MTL

With the experimental data, the rate profiles were simulated based on the reaction rate drop and their percentage of active sites. All the liquid-phase catalytic reactions were performed in duplicates to evaluate the results variance and an standard average error for those reported rates of 2.3% was found for ACE and 2.7% for CPO, thus it is assumed that the values used for modelling would not interfere on the results interpretation. The resulting profile is unique and has a particular Thiele modulus. According to the expressions described above the effectiveness factor and the theoretical maximum rate is found. The fitting optimization adjust both ϕ_0 and L_0 according to the rate decrease and minimizing the difference between the experimental and calculated rates. A higher degree of deviation from linear behavior results in a higher the Thiele modulus. The adjustable site density can be used as a reflection of how well the simulation agrees with the experimental data. If the final value for L_o deviates from what was found through IPA-TPD for the parent zeolite, then less representative those values are to that studied case.

The values of maximum density of sites (L_0) obtained from the fittings (0.12 and 0.47-0.50 mmol/g_{cat}) are in good agreement with those obtained experimentally by IPA-TPD (0.10 and 0.40 mmol/g_{cat}). These sets of values are reasonably similar, and the fitting quality is good. In the case of fixing L_o, a poor quality fitting is obtained as well as its respective values, being disregarded in the present work. The calculated maximum rates are summarized in **Table 2** as well as Thiele moduli and its respective effectiveness factors.

Table 2: Reaction-diffusion parameters obtained from fitting the titration model.

	Maximum Site Density (mmol/g_{cat})	Thiele Modulus of original sample (ϕ_0)	Effectiveness Factor (η)	Maximum Rate (r_{max}) (μmol/g_{cat} sec)	TOF_{max} (x10^{-3} sec^{-1})
ACE-140	0.12	2.0	0.80	3.3	31
CPO-Z140	0.12	3.3	0.64	5.0	48
ACE-Z40	0.47	6.4	0.39	14.7	37
CPO-Z40	0.50	10.3	0.26	29.9	74
ACE-HY30	0.23	4.7	0.50	23.8	102
CPO-HY30	0.23	< 0.1	1.00	7.4	32

On the ZSM5 series, CPO shows a higher Thiele modulus than ACE in both Si/Al catalysts. Of course, this is due to the combination of lower diffusivity and higher intrinsic reactivity of CPO. The first is obvious once CPO size provides more steric constraint inside the confined channels as it diffuses. But in contrast it better interacts with the framework structure and thus have a higher contribution to the rate due to the confinement effect [98]. In fact, the Thiele moduli ratio of CPO to ACE could be analyzed as follows $\frac{\phi_{CPO}}{\phi_{ACE}} = \sqrt{\frac{k_{CPO}}{k_{ACE}}}.\sqrt{\frac{D_{ACE}}{D_{CPO}}}$, in which the ratio of their effective diffusivities in the zeolite is essentially the ratio of their Knudsen diffusivities, which in turn can be expressed in terms of molecular weights ($\sqrt{\frac{MW_{CPO}}{MW_{ACE}}}$). On the other hand, the ratios of the rate constants is the

ratio of intrinsic (maximum) TOFs for the two reactants. Therefore, in Z140 we have $\sqrt{\frac{k_{CPO}}{k_{ACE}}} = \sqrt{\frac{48}{31}} = 1.24$ and $\sqrt{\frac{D_{ACE}}{D_{CPO}}} = \sqrt{\sqrt{\frac{MW_{CPO}}{MW_{ACE}}}} = 1.1$.

So, as above, ($\frac{\phi_{CPO}}{\phi_{ACE}} = 1.24 * 1.1 = 1.36$), which compares relatively well with the ratio of the moduli obtained from the fitting. In this case, $\frac{\phi_{CPO}}{\phi_{ACE}} = 3.3/2.0 = 1.62$. Doing the same analysis over Z40: $\sqrt{\frac{k_{CPO}}{k_{ACE}}} = \sqrt{\frac{74}{37}} = 1.42$ and $\sqrt{\frac{D_{ACE}}{D_{CPO}}}$ as found for Z140 (=1.1). Taking the Thiele moduli ratio, $\frac{\phi_{CPO}}{\phi_{ACE}} = 1.42 * 1.1 = 1.56$, which is also comparable with the found values, $\frac{\phi_{CPO}}{\phi_{ACE}} = 10.3/6.4 = 1.60$.

Interestingly, as shown in **Table 2**, the extrapolated values of $(TOF)_{max}$ for the self-condensation of CPO on Z140 and Z40 are higher than that for ACE, but the opposite is true on Y30. In ZSM5, both values for r_{max} in ACE are similar but there is a discrepancy in CPO. The higher $(TOF)_{max}$ in Z40 can be attributed to the presence of pair sites as already reported in literature [149]. There, cobalt was used to titrated Al pairs at low Si/Al ratio catalysts. Thus, here we assume their presence and influence over the catalytic activity of CPO but not for ACE.

The observed difference between the activity of ACE and CPO in ZSM5 and Y could be ascribed to the different confinement effects that these two reactants may be subjected to in the two zeolites. That is, in HY the active sites are located in the relatively large (13 Å) supercage, compared to the much smaller void space in the confined channels of ZSM5 (~ 5-5.5 Å). Such smaller voids seem to better interact with the intermediate species during the C-C bond formation and thus decrease the energy barrier needed for the

product formation. Inside the supercage of faujasite these species do also fit, however the interaction between molecule-framework are not as pronounced as in MFI.

In this regard, literature mentions a possibility of a change in the intermediate arrangement in order to react inside restricted confinements [150]. A computational calculations analysis of the high energy transition states (TS) related to the rate limiting step of transalkylation of diethylbenzene and benzene inside of a synthesized IWV and MOR. The main difference observed was a geometry distortion in the transition states molecules resulting in a higher energy barrier inside of the confined voids of MOR. In IWV the molecule had a more optimized arrangement and also better interaction with the framework which contributed to its higher turnover rate when compared to MOR. Such analysis if applied and hypothesized in the case of self-condensation of ACE and CPO in MFI and FAU could lead to two discussions: no change in the TS conformation inside of a confined void and change in the conformation. Due to the smaller size of ACE and its intermediates, it is plausible to imply that no change in conformation exists and that diffusion is major impact factor in both zeolites. Its high 4.7 Thiele modulus in HY compared to <0.1 for CPO supports this concept. A further explanation on trimer formation will later be discussed. Differently, in CPO, one might expect a more confined environment causes a change in the intermediate configuration to fit inside MFI voids. This distorted intermediate requires a higher energy to compensate its configuration change, plus the energy to overcome the barrier for the product formation. But seems that the interaction with the structure confined walls pays off such difference and shows a larger turnover rate when compared to ACE, both in true and measured rate. In FAU, the intermediate inside the large voids of supercage may have a more stable conformation but does not seem to

have a stronger confinement effect as compared to MFI. Oppositely, if no change of conformation is seen in CPO, the sole influence of confinement effect and easier diffusion is the explanation for the observed values in both MFI and FAU as previously discussed.

Other interesting result is selectivity of dimer and trimer in the self-aldol condensation of ACE and CPO in the two series of zeolites. **Table 3** shows the contributions of the dimer and trimer in ACE product selectivity, and it is clear that in zeolite Y it significantly impacts the consumption rate whereas in ZSM5 it is considered negligible. The already discussed high diffusion rates of ACE inside FAU structure influence such result because as the dimer is formed a nearby ACE molecule will be present and will further react to form the trimer. Not only that, the supercage allows its formation and seems to do not offer steric restrictions for its larger size. As conversions drops its contribution to ACE consumption does so just because the dimer presence influences its rate of formation. According to **Figure 26** it seems that the trimer formation has a second order or higher dependence on ACE concentration/consumption, but no kinetic study was finely performed about this matter due to purpose of this work.

Table 3: Dimer and trimer selectivity comparison in self-condensation of both ACE and CPO

Self-condensation Products		Conversion	Y30	Conversion	Z140
ACE	[A]A	9.0%	54%	2.0%	100%
	A[A]A		46%		0%
CPO	[C]C	5.6%	95%	2.6%	98%
	C[C]C		5%		2%

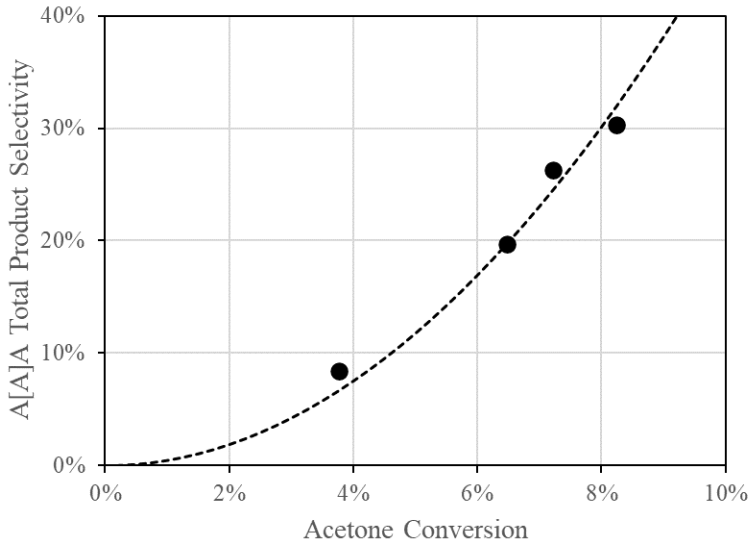

Figure 26: Trimer total product selectivity second order dependence on ACE conversion in the self-aldol condensation in Y30 zeolite.

As discussed before, in regard to the rate profile behavior with MTL, **Figure 27.a)** presents the rate deviation from a linear tendency as the diffusion constraint is more present. Gathering all results and using a scatter plot (**Figure 27.b)**) to evaluate the efficiency of the used method one can confirm the capability of both experimental and modeling approach to spot and quantify mass-transfer limitations when there is a change in feeding molecules, initial concentration of active sites and zeolite structure.

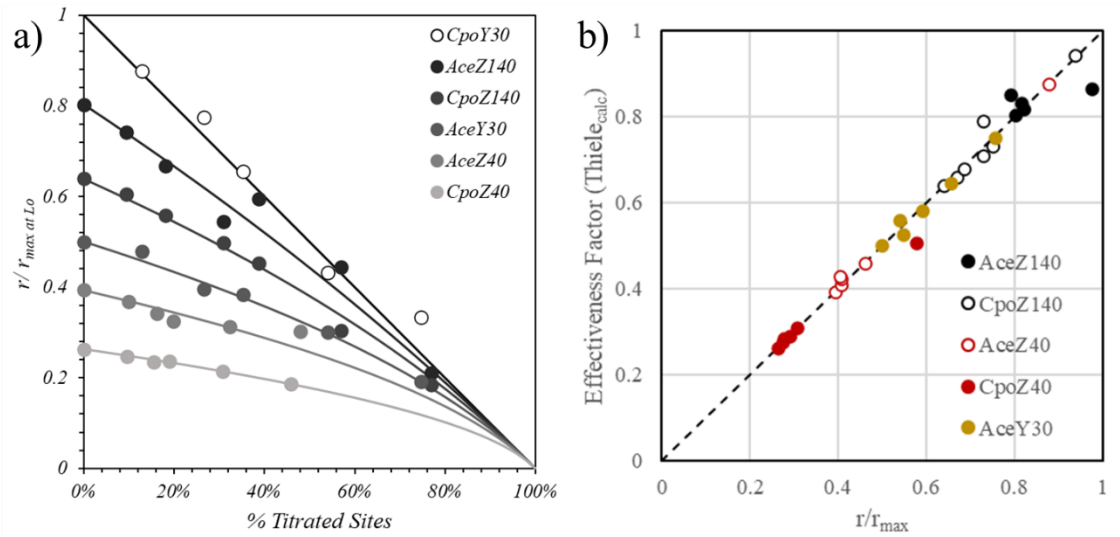

Figure 27: a) Experimental set of data for the studied zeolites and **b)** parity plot comparing the effectiveness factor calculated from Eq (1) and that obtained from the experimentally observed self-condensation rates relative to the maximum rate (no MTL).

2.4.2.3 A Reaction Mechanism Kinetic Study over Y30 with CPO Self-aldol Condensation

At this point, the analysis over CPO in faujasite catalyst (Y30) showed that no MTL are present under the applied conditions and the understanding of the kinetically relevant step is worth studying. As previously discussed, if confinement and structural parameters change within the catalyst the reaction relevant step does so. For a better mechanistic analysis, the elementary steps for the ketone aldol condensation mechanism are exploited below and understood to be: ketone adsorption, enol formation, C-C coupling, further sequential C-C coupling and/or desorption. 'C' represents cyclopentanone. [C] indicate the ketone's enol.

$$C + * \rightleftarrows C* \qquad \text{Cyclopentanone adsorption}$$

$$C* \rightleftarrows [C]* \qquad \text{Cyclopentanone enol}$$

$[C]* + C \rightleftarrows [C]C*$	C-C Coupling between an activated cyclopentanone and a bulk cyclopentanone (*Eley-Rideal mechanism*)
$[C]* + [C]* \rightleftarrows [C]C** $	C-C Coupling between an activated cyclopentanone and an adsorbed cyclopentanone (*Langmuir-Hinshelwood mechanism*)
$[C]C* \rightleftarrows [C]C + *$	Cyclopentanone dimer desorption
$[C]C* + C \rightleftarrows C[C]C*$	C-C Coupling between an adsorbed dimer and a bulk cyclopentanone
$C[C]C* \rightleftarrows C[C]C + *$	Cyclopentanone trimer desorption

Three kinetic steps are considered here to be the rate-limiting steps:

- Cyclopentanone adsorption or enol formation (unimolecular);
- C-C coupling with a nearby molecule (bimolecular Eley-Rideal mechanism – ER);
- C-C coupling with an adsorbed molecule (bimolecular Langmuir-Hinshelwood mechanism – LH).

Each rate-limiting step will have a representative equation as follows:

Enol Formation	*C-C Coupling ER*	*C-C Coupling LH*
$r = \frac{kK_{ads\ CPO}C_{CPO}}{(1 + K_{ads\ CPO}C_{CPO})}$	$r = \frac{kK_{ads\ CPO}{C_{CPO}}^2}{(1 + K_{ads\ CPO}C_{CPO})}$	$r = \frac{k{K_{ads\ CPO}}^2{C_{CPO}}^2}{(1 + K_{ads\ CPO}C_{CPO})^2}$

In where: r is rate of reaction, k is the reaction constant, $K_{ads\ CPO}$ is the adsorption constant of CPO, and C_{CPO} is the cyclopentanone concentration. By linearizing these equations, one obtain:

Enol Formation *C-C Coupling ER* *C-C Coupling LH*

$$\frac{1}{r} = \frac{1}{k} + \frac{1}{kK_{ads\ CPO}}\frac{1}{C_{CPO}} \qquad \frac{C_{CPO}}{r} = \frac{1}{k} + \frac{1}{kK_{ads\ CPO}}\frac{1}{C_{CPO}} \qquad \frac{1}{\sqrt{r}} = \frac{1}{\sqrt{k}} + \frac{1}{\sqrt{k}K_{ads\ CPO}}\frac{1}{C_{CPO}}$$

Plotting the inverse of the feeding concentration of CPO and the respective reaction rate for each equation, k and $K_{ads\ CPO}$ can be found through the slope and the intercept, as well as R^2. **Figure 28** shows the respective plots for each case and it is clear that the fitting results point to either a unimolecular type of mechanism in which the enol formation or adsorption is the rate-limiting step, or a bimolecular mechanism in which the C-C coupling with an adsorbed molecule.

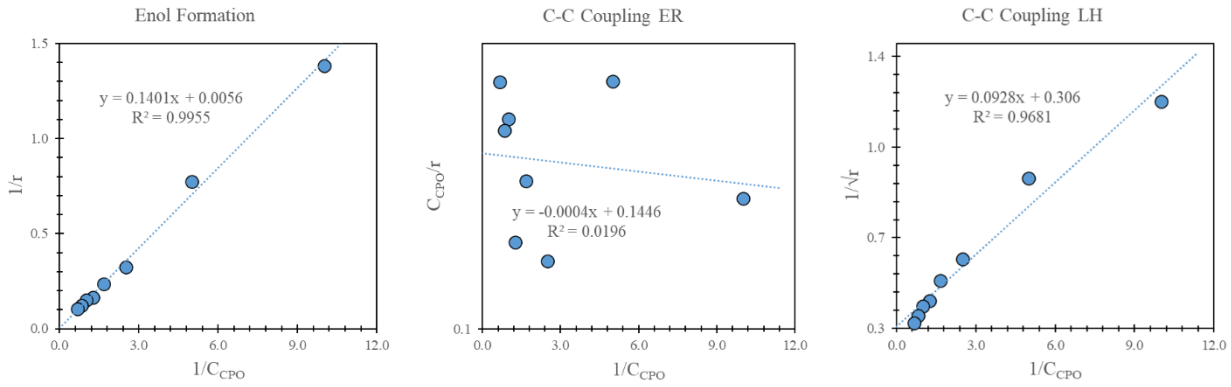

Figure 28: Linearized plot of each kinetic model for the CPO self-aldol condensation in Y30.

The C-C coupling following an Eley-Rideal type of mechanism does not seem to be the mechanism in which CPO reacts over Y30 surface. However, in such CPO concentrations, one can consider a full coverage of active sites ($K_{ads\ CPO}C_{CPO} \gg 1$). In the rate equation it means that the ratio between r/C_{CPO} is simply the reaction constant:

$$\frac{r}{C_{CPO}} = k$$

By taking the average of the linearized values and minimizing the error between experimental and calculated values, a resulting k and $K_{ads\ CPO}$ are found for this particular

mechanism. **Table 4** presents the calculated values of the reaction parameters for each kinetic model.

Table 4: Calculated reaction and adsorption constant for CPO self-aldol condensation over Y30 from the reaction equations.

	Enol Formation	C-C Coupling ER	C-C Coupling LH
k	179.56	6.97	10.68
$K_{ads\ CPO}$	0.040	106.54	3.30

Prior to conclusions solely based on the reaction parameter values, the calculated reaction rate versus CPO concentration was plotted and confronted with the experimental results (**Figure 29**). It is clear from the plot that the C-C coupling occurring with an adsorbed molecule (LH) might not be the mechanism in which the CPO-condensation occurs, leaving the reaction to be limited to either CPO adsorption or enol formation or C-C coupling with a nearby non-adsorbed molecule.

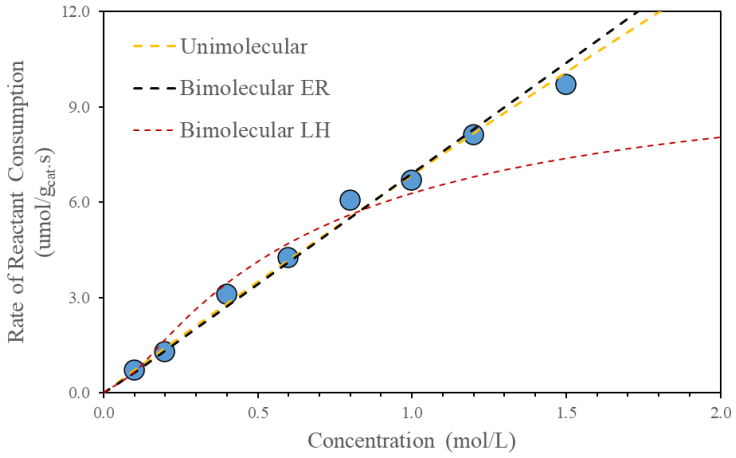

Figure 29: Linearized plot of each kinetic model for the CPO self-aldol condensation in Y30.

From Transition State theory, it is known that the reaction constant is a function of the temperature and the Gibbs free energy at the transition state [151]. Once the models

assume a first-order reaction dependence on CPO concentration, the equations will assume the form of:

$$\frac{r}{C_{CPO}} = k_{TST} = \frac{k_B T}{h} \exp\left(\frac{\Delta S_0^{\neq}}{R}\right) \exp\left(\frac{-\Delta H_0^{\neq}}{RT}\right)$$

In where k_B is the Boltzmann constant, h is the Planck constant, T is the reaction temperature, $\Delta S_0^{\neq}$ is the entropy of activation, $-\Delta H_0^{\neq}$ the enthalpy or activation (or energy of activation, E_{act}), and R the gas constant. Linearizing the equation as a function of the reaction temperature:

$$ln\left(\frac{r_{T_i}}{C_{CPO} BAS} \frac{h}{k_B T_i}\right) = \frac{\Delta S_0^{\neq}}{R} - \frac{\Delta H_0^{\neq}}{R} \frac{1}{T_i}$$

Here, changing the temperature and observing the respective reaction rate, one is able to calculate the entropy and the enthalpy of activation of a reaction under the applied reaction conditions. **Figure 30** shows the change in Napierian logarithm of rate versus the inverse of the temperature (in Kelvin). The values for E_{act} and $\Delta S_0^{\neq}$ are 11.04 kJ/mol and -256.76 J/mol.K, respectively.

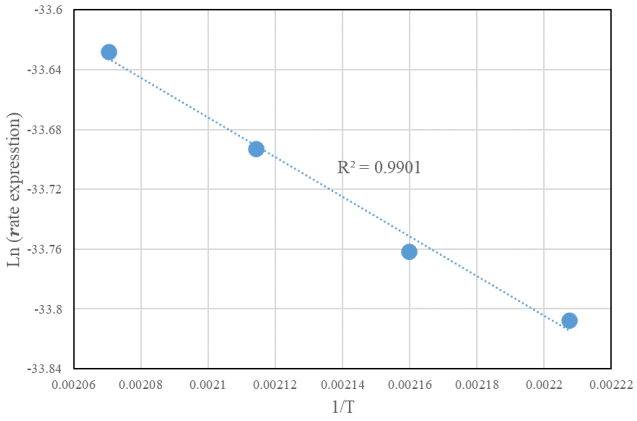

Figure 30: Linearized plot of the Transition State Theory versus the inverse of reaction temperature. C_{CPO} = 1 mol/L.

The delta entropy value found is large negatively enough to be referred as adsorption energy values, commonly found in this elementary step in which has none or

very low activation energies. Literature reports CPO formation entropy at 298 K to be 313.68 J/mol.K, similar to the measured value [152]. If one assumes that this is not the case, the calculated activation energy value is sufficiently low and considered as an apparent energy of activation which exists when the surface has a low reactant coverage. There, the activation energy has contributions of the enthalpy of adsorption resulting in a lower barrier compared to the true activation energy ($E_{app} = \Delta H_{ads} + E_{act}$). If such coverage consideration is true, the experimental results do not follow the other proposed C-C coupling mechanism due to the second order dependence over CPO concentration. Once a first order relation between the experimental rate and concentration was found, and by elimination, CPO adsorption or enol formation is the rate limiting step in CPO aldol-condensation over zeolite Y30.

2.4.2 Cross-condensation Product Selectivity Shifts under Different Regimes

After validating the use of the Na titration method to quantify MTL in self-aldol condensation reactions, the same method to investigate the effects of MTL was applied on cross-aldol condensation between ACE and CPO to observe selectivity differences as different governing regimes actuate.

Selectivity were monitored as gradual Na-titration moved the reaction regime from mass-transfer limited to kinetic controlled. In all cases, dimers represented the largest majority (> 90%) of the product and analyzed accordingly. This pattern is different from the self-condensation of ACE on HY, which exhibited significant amounts of trimers. Therefore, in the case of cross-condensation on both zeolites selectivity will only refer to the four dimmers [A]A, [A]C, [C]A, and [C]C, where the brackets indicate the reactant that

has been activated first to form the enol intermediate and the one without brackets represents the electrophile attacked by the enol [98].

2.4.2.1 HZSM-5 and NaHZSM-5 (Si/Al:140) zeolites

On this catalyst, the Thiele moduli obtained for the two self-condensation reactions were relatively low ($\emptyset_{ACE}$ = 2.0, $\emptyset_{CPO}$ = 3.3) indicating only a small influence of MTL on either reactant, but somewhat higher in CPO. In agreement with this behavior, the cross-condensation results show a measured rate-drop very close to the ~ 60 % drop in BAS (see **Table 5**). In this case, with a minor extent of MTL, the changes in selectivity are also moderate, but changing in the direction that one might expect. That is, the product involving the smallest reactant ([A]A), which is favored under MTL become less favored when MTL are removed by Na titration. By contrast, the selectivity to the one derived from the larger reactant ([C]C) becomes enhanced without MTL. However, in all cases the selectivity changes upon Na titration are unexceptional since both Thiele modulus values are similarly low.

Table 5: Cross condensation reaction result outputs in Z140.

Catalyst	BAS ($mmol/g_{cat}$)	Product Selectivity				Overall Consumption Rate	
		[A]A	[A]C	[C]A	[C]C	ACE ($umol/g_{cat}.s$)	CPO ($umol/g_{cat}.s$)
Z140	0.10	25%	15%	16%	44%	2.61	3.70
Z140 0.05M Na	0.04	18%	17%	16%	48%	0.87	1.62

2.4.2.2 HZSM-5 and NaHZSM-5 (Si/Al:40) zeolites

A similar set of analysis is done over Z40. Here the effect of MTL is clearly higher and thus the changes over the cross-condensation results are more pronounced as shown in

Table 6. Within the CPO activated products the increase in [C]C selectivity in contrast with [C]A decrease highlights the regime effect on this catalyst. The ACE activated products showed an unexpected behavior with an increase of both [A]A and [A]C products as titration occurs. A hypothesis for such is a correlation between the concentration gradient of ACE and CPO and their diffusion inside the MFI framework. Because ACE has less effect over MTL compared to CPO, by decreasing MTL along the particle ACE concentration increases rapidly compared to CPO, then more products containing ACE appear. However, as the MTL is mitigated CPO products are more favored as observed in Z140.

Table 6: Cross condensation reaction result outputs in Z40.

Catalyst	BAS ($mmol/g_{cat}$)	Product Selectivity				Overall Consumption Rate	
		[A]A	[A]C	[C]A	[C]C	ACE ($umol/g_{cat}.s$)	CPO ($umol/g_{cat}.s$)
Z40	0.40	16%	12%	36%	35%	5.55	7.39
Z40 0.05M3x Na	0.15	20%	14%	24%	41%	4.31	6.44

2.4.2.3 HY and NaHY (Si/Al:30) zeolites

The effect of Na titration on selectivity is more pronounced on the NaHY series than on the NaH-ZSM5. As shown in **Figure 31**, the removal of MTL causes an interesting shift in selectivity for both [C]C vs. [C]A as well as [A]C vs. [A]A. The product preference shifts from [C]A > [C]C and [A]A > [A]C under MTL to [C]C > [C]A and [A]C > [A]A when MTL are removed. That is in the kinetic regime, the C electrophile is preferred rather than A. This is caused by the easier accommodation of a positive charge in a secondary β-carbon near the carbonyl as the ketone is activated in a confined environment. Previous study on cross aldol selectivity with ACE and CPO was done in functionalized mesoporous

MCM-41 at low and high density of sites [98]. The steric factor was determining in that case which no specie-framework interaction existed, which might be the decisive factor at present zeolite.

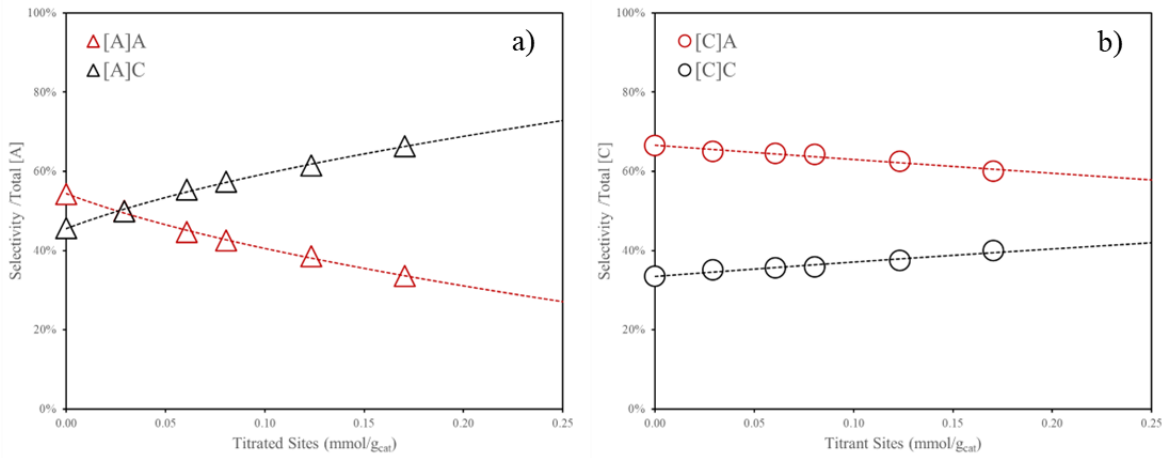

Figure 31: Selectivity distribution of cross-aldol condensation of Ace-CPO in NaHY 30 series.

The Thiele modulus estimation for cross-condensation were calculated from the catalytic experiments following the same methodology as for self-condensation. The results are shown in **Table 7** and **Figure 32**. Once again, the large Thiele numbers were found on CPO products as a reflection of its large diffusion constraint in confined environments when compared to ACE. An analysis in regards of the diffusion influence over the cross condensation products formation considers the already discussed three decisive factors that lead to the observed trends in mass-transfer limited and kinetic limited systems: enol activation, steric influence at C-C coupling formation, and confinement effect. From the catalytic results it is clear that CPO is preferentially activated when ACE is present, existing in >80% of the products formed. In a MTL regime, the steric influence CPO faces is higher compared to ACE, and as a result [x]A products dominates in the Na-free catalytic runs. The two times higher turnover rate between [C]A and [C]C highlights the faster acetone diffusion that was previously discussed in the self-condensation case,

which was one of the factors that influenced in MTL. As titration progresses towards a more kinetic driven regime the shift in products selectivity occurred in the very beginning of titration for the [A]x products whereas for [C]x seems to shift at very high levels of site titration according to the simulations represented in **Figure 32**. Such titration levels could not be obtained experimentally. The steric effect is responsible for the preference towards [C]C and thus the higher the confinement effect.

Table 7: Parameters obtained by fitting experimental data of cross-aldol condensation on the NaHY(Si/Al:30) series with the reaction-diffusion model.

	Thiele Modulus (ϕ)	Effectiveness Factor (η)	Maximum Rate (μmol/g_{cat} sec)	TOF_{max} ($x10^{-3}$ sec^{-1})	TOF_{meas} ($x10^{-3}$ sec^{-1})
[A]A	0.0	1.00	0.66	3	3
[A]C	8.9	0.30	2.17	9	2
[C]A	3.0	0.67	6.25	27	18
[C]C	8.1	0.33	6.42	28	8

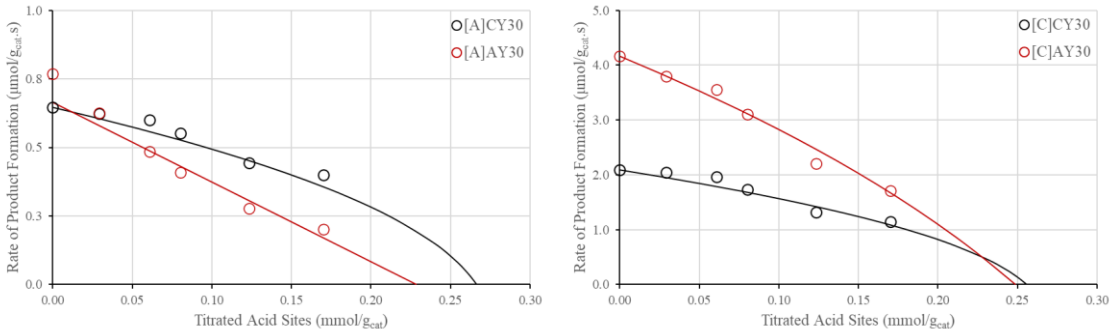

Figure 32: Rates of products formation as a function of Na-titrated site density in the NaHY (Si/Al:30) zeolite series (symbols) compared to calculated rates derived from the reaction-diffusion model. The lines represent the modeled profiles for each self-condensation result.

Other result is the similar values for Thiele moduli obtained for [A]C and [C]C. At this point it seems reasonable to infer in the present case of the cross condensation between ACE and CPO that the extent of MTL in the HY 30 series is a result of both high surface coverage of [C] and CPO diffusion and further reaction as a secondary/nearby molecule. In an imaginary case that either ACE or CPO is activated, CPO has a lower preference for

reacting because of its lower concentration inside the internal structure of the catalyst, when in fact ACE presents lower concentration gradients. And as such constraints are removed, the steric effect coupled with the confinement effect generated by the structure results in the preferential formation of [x]C products in contrast of [x]A.

2.4.2.4 Analysis of true TOF for cross-condensation free of MTL

Additionally, if both the maximum and measured turnover rates are compared (Table 6) the explanations given for the influence of MTL in Y series are plausible. [A]A does not seem to be affected by diffusion limitations due to its lower activity, mainly if compared to the self-condensation results (TOF_{self} Prod Formation = $17x10^{-3}$ sec^{-1} vs. TOF_{cross} Prod Formation = $3x10^{-3}$ sec^{-1}). [A]C and [C]C *true* TOF comparison shows the clear preference towards CPO as a nucleophile, resulted from its interaction with framework within a confined space. And last, the similar *true* TOF found for [C]A and [C]C. No kinetics were studied to better understand the contributions on both ketones in the cross-condensation due to the purpose of this work; however, it seems that the rate limiting step of these two condensation reactions are related to a unimolecular dependence on CPO rather than a bimolecular reaction pathway.

2.4.3 In-situ Pyridine Titration

After a deep investigation of MTL in porous zeolites using Na as a titrant added prior to the catalytic reactions, the use of an in-situ procedure will be investigated next. The same series of zeolites are used, and the discussions are more relative towards a qualitatively effect rather than quantitative.

HZSM-5 (Si/Al 140) zeolite: **Figure 33** shows the condensation rates of ACE and CPO over Z140 as a function of an increase in the in-situ pyridine uptake. Primary observations are mainly the inability of pyridine to cease the catalytic activity at higher loadings, leading to think that the titrant is desorbing from the acid surface rather than inactivating the active site. If a comparison between the pyridine experimental rates and modeled curves found in Na-titration is done, a confirmation from such desorption behavior is set and more pronounced in CPO. (**Figure 34**).

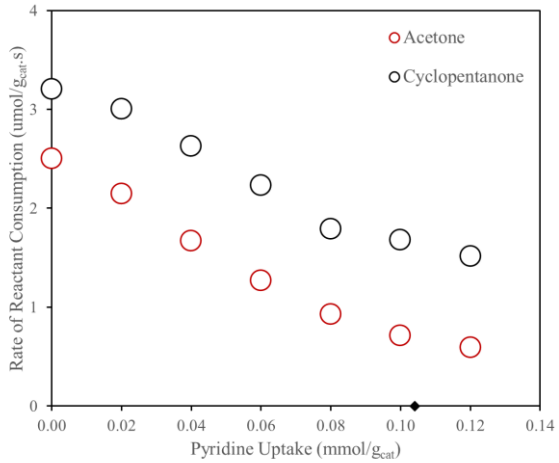

Figure 33: Self-condensation rates of CPO and ACE as a function of in-situ pyridine uptake in ZSM5 zeolite with Si/Al of 140. The black point over the graph points to at zero rate at the measured IPA-TPD BAS density relative to Z140.

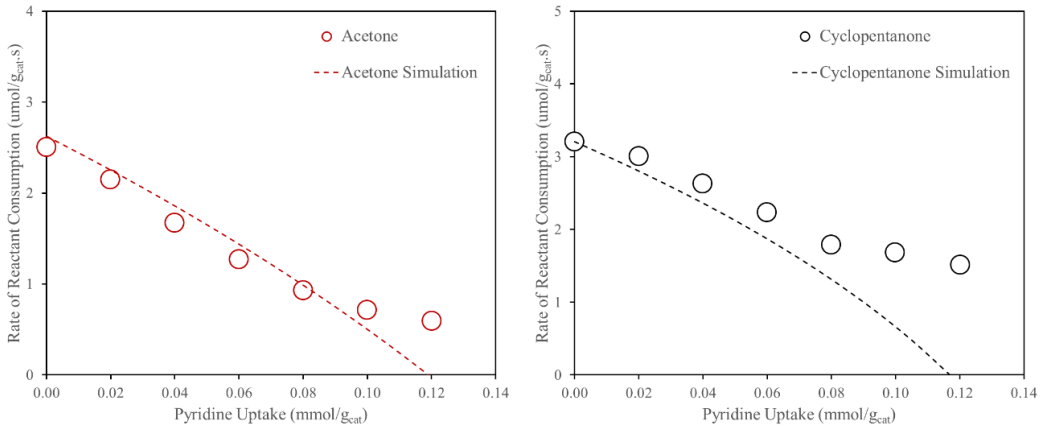

Figure 34: Comparison between experimental rates on pyridine with modeled Na-titration rates in ZSM5 zeolite with Si/Al of 140.

HZSM-5 (Si/Al 40) zeolite: In a higher site density ZSM5 it was proven the increase of MTL in both ketones, being more pronounced in CPO case. Here, the non-titrant behavior of pyridine in both cases is more obvious, shown by the plateau in CPO catalytic rates. It points out that an existing synergy in the liquid phase reactions between the reacting species and pyridine is possible either from a competitive adsorption between these two molecules or a solvent interaction between pyridine and cyclohexane. It is also important to highlight that in a lower BAS density the remaining activity was 28% of its initial rate compared to 42% in Z40. The same plot performed in Z140 comparing the modeled rate versus experimental rates with pyridine are shown in **Figure 35**. As occurred in Z140, the titrant over ACE occurred more effective in comparison to CPO.

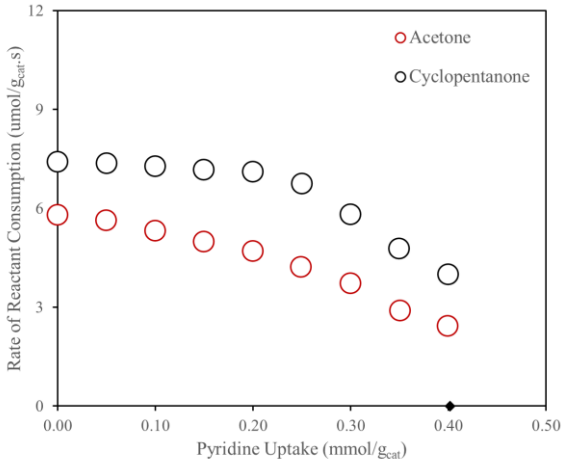

Figure 35: Self-condensation rates of CPO and ACE as a function of in-situ pyridine uptake in ZSM5 zeolite with Si/Al of 40.

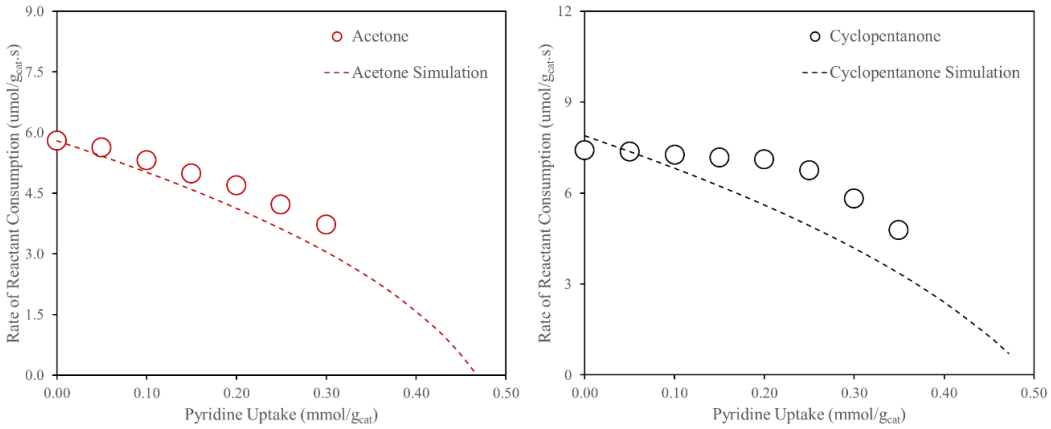

Figure 36: Comparison between experimental rates on pyridine with modeled Na-titration rates in ZSM5 zeolite with Si/Al of 40.

HY (Si/Al 30) zeolite: Previous observations in regards of pyridine desorption from the surface are clearer in Y30, mainly with the pyridine evolution over CPO-condensation showing a plateau throughout the whole range of titration (**Figure 37** and **Figure 38**). ACE distanced itself from the modeled curve, but showed an adequate rate drop as put next to the modeled curves.

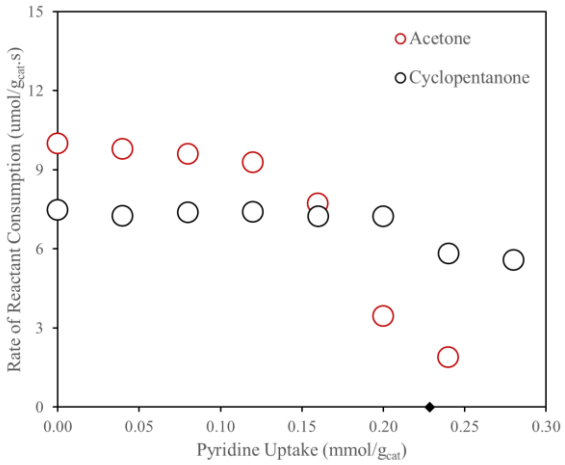

Figure 37: Self-condensation rates of CPO and ACE as a function of in-situ pyridine uptake in Y zeolite with Si/Al of 30.

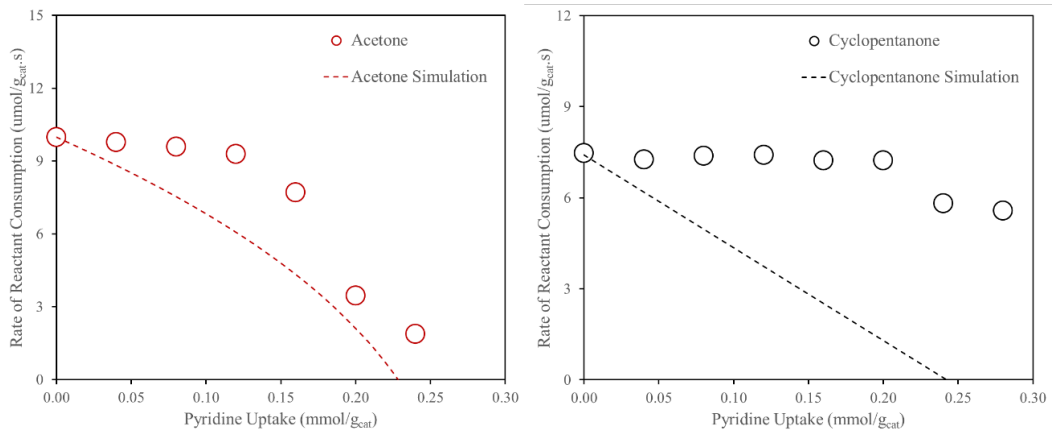

Figure 38: Comparison between experimental rates on pyridine with modeled Na-titration rates in Y zeolite with Si/Al of 30.

2.4.3.1 Role of Pyridine as a Titrant in Liquid Phase Reactions

Differently than what was performed with the Na-titrated data, no modeling is done in the sake of understanding the role of pyridine in the zeolite active surfaces. To recall the conclusions taken from the titration graphs, pyridine seems to do not effectively titrate the active acid sites in all the zeolites performed resulted from a desorption. This behavior is affected due to a correlated synergy with the system characteristics in general: acid site density, intramolecular interaction with reactants and solvent, or the nature of each zeolite.

A different way to observe the differences is plotted in the **Figures 39**, **40**, and **41**, bringing the relative activity drop within each zeolite as a function of either pyridine uptake or Na-titrated sites. The purpose of these plots are mainly to show the deviation from the "*expected*" (i.e. modeled) result as obtained during the Na-experiments. While in MFI the deviation is less evident, in faujasite it is notable for both ketones. Two hypotheses will be discussed next, whether the pyridine is being desorbed due to reaction temperature or because of an intermolecular interaction with the system species.

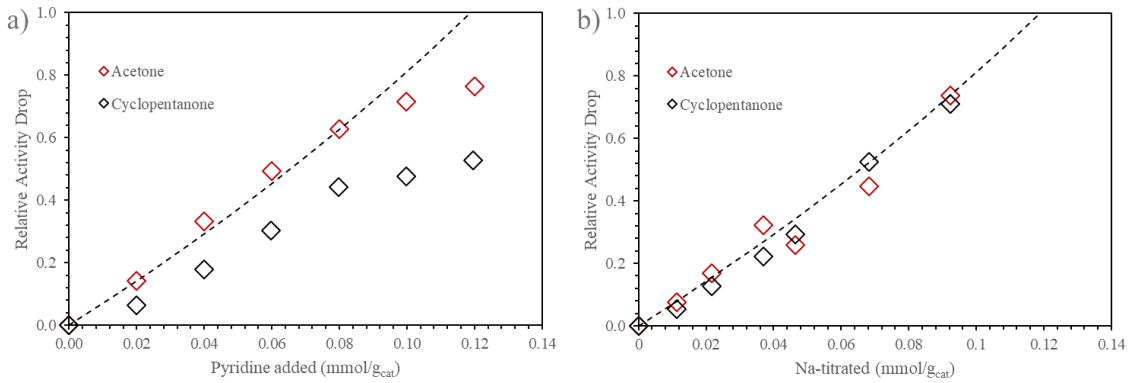

Figure 39: Relative activity drop as titrant agent is added in ZSM5 zeolite with Si/Al of 140 with **a)** pyridine addition, and **b)** Na-titration.

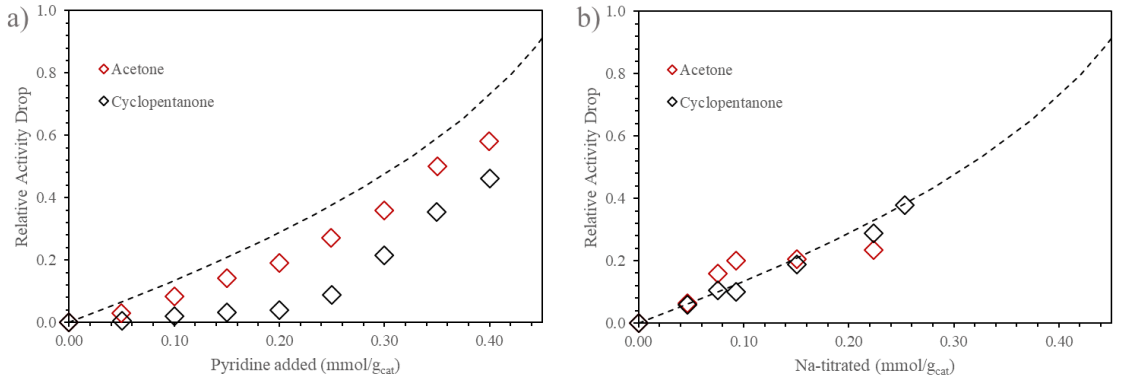

Figure 40: Relative activity drop as titrant agent is added in ZSM5 zeolite with Si/Al of 40 with **a)** pyridine addition, and **b)** Na-titration.

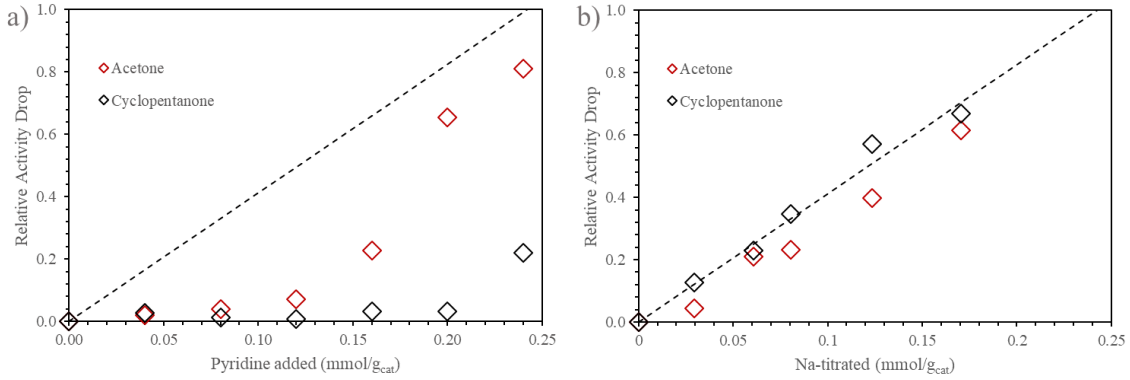

Figure 41: Relative activity drop as titrant agent is added in ZSM5 zeolite with Si/Al of 40 with **a)** pyridine addition, and **b)** Na-titration.

The chemical adsorption of species over active surfaces and its analysis using infrared or ultraviolet-visible spectroscopy is a commonly used technique to characterize Bronsted or Lewis acid sites in catalysts [153-155]. In acid sites, infrared spectroscopy can

use pyridine addition over the catalyst sample to observe peak disappearances relative to titrant adsorption and the growth of new peaks relative to the interaction with the surface atoms [156, 157]. Busch et al. had identified the peaks assigned to pyridine interaction with BAS in both zeolite Y and ZSM5 (**Table 8**), and observed their spectra after heating the sample chamber at high temperatures [158]. After a thermal treatment at 250 ^{o}C for 15 min physisorbed pyridine peaks disappeared while chemisorbed pyridine at peaks position of in the Bronsted and Lewis sites remained (**Figure 42** and **Figure 43**). Based on this example, temperature is not likely to be the reason pyridine is desorbing from the BAS surface, so the idea of an interaction with the system species might cause of non-titrant behavior.

Table 8: Classification of chemi- and physisorbed pyridine on acidic solids. Adapted from Ref [158].

Position of the band [cm-1]	Linkage of pyridine
1638	Bronsted acid sites
1620	Lewis acid sites
1580	Physisorbed
1545	Bronsted acid sites
1490	Bronsted and Lewis acid sites
1450	Lewis acid sites
1439	Physisorbed

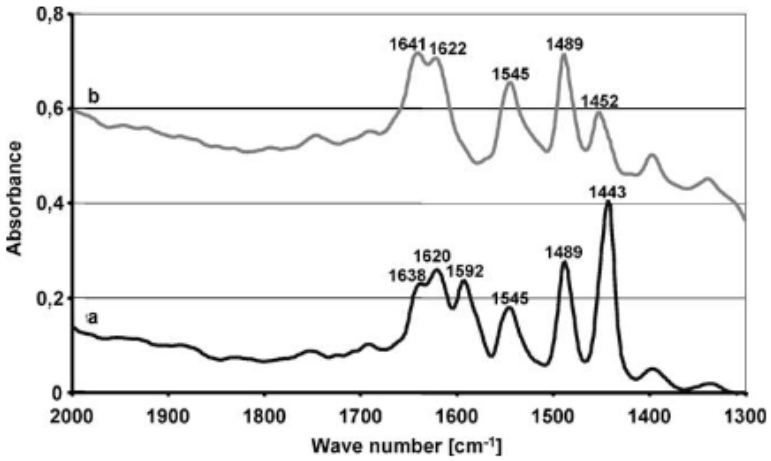

Figure 42: R spectrum of sorbed pyridine on the surface of zeolite Y (10 mg/cm^2) before heating (trace a) and after heating at 250 ◦C for 15 min (trace b) recorded in parallel mode with the FPA detector. The spectra are for the same sample at the same position in the cell. Reproduced from Ref [158].

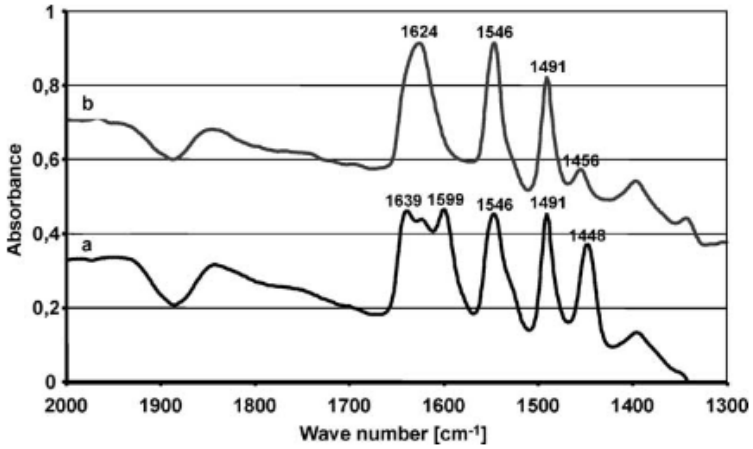

Figure 43: IR spectrum of sorbed pyridine on the surface of H-ZSM-5 (10 mg/cm^2) before heating (trace a) and after heating at 250 ◦C for 15 min (trace b) recorded in parallel mode with the FPA detector. The spectra are for the same sample at the same position in the cell. Reproduced from Ref [158].

A question could exist in regards of this interaction, whether it happens in the bulk phase or inside the zeolite framework around the site environment. In MFI, the tortuous channels have a constant diameter of around 5.5 Å which could impede the existence of a large concentration of species around the active site. However, the supercages in zeolite Y have an intern diameter of 13 Å with a pore aperture of 7.4 Å, being more permissive for

the species transit and aggregation inside the framework. Thinking about these differences, solvent interactions appears to cause pyridine desorption.

In order to prove the presented hypothesis, a mixture containing catalyst, solvent and pyridine at high loadings was stirred for 30 min at room temperature and analyzed in ultraviolet-visible spectroscopy (UV vis). **Figure 44** displays the UV vis spectra of both zeolite ZSM5 and Y used in the catalytic reactions. The peaks in the gray spectra are due to catalyst-solvent interactions that exist in the filtered mixture, and the subtracted line represents pyridine and its interactions with either the solvent or the catalyst. Once UV vis does not capture pyridine inside the zeolite framework, it is assumed that the existing difference is due to dissolved pyridine within the mixture. It is clear from the UV vis results the stronger effect of solvent towards pyridine in zeolite Y, which inside ZSM5 due to the lack of space this solvent-pyridine effect is minimal. To comply such conclusion the plateau in CPO catalytic results over Z140 with pyridine uptake only occurs at higher loadings of pyridine, enough to titrate a portion of the sites but enough to be located in the bulk liquid phase, while in zeolite Y such plateau exists early in the titration.

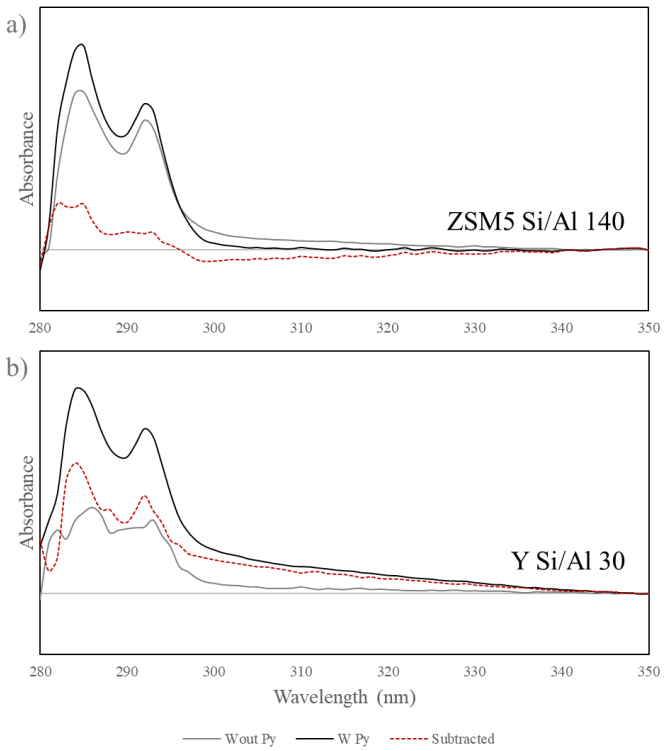

Figure 44: Ultraviolet visible light spectra of a mixture containing 400 mg of catalyst (‘a)’ respective to zeolite ZSM5, and ‘b)’ to zeolite Y) in 100 mL of cyclohexane as solvent with 0.20 mmol/g_{cat} of pyridine added.

To prove that pyridine that those peaks are assigned to dissolved pyridine, two and threefold amount of titrant were added into the blank volume. Their respective UV vis spectra in **Figure 45** displays the substantial increase of the 292 nm peak, an indication of more pyridine in the solution.

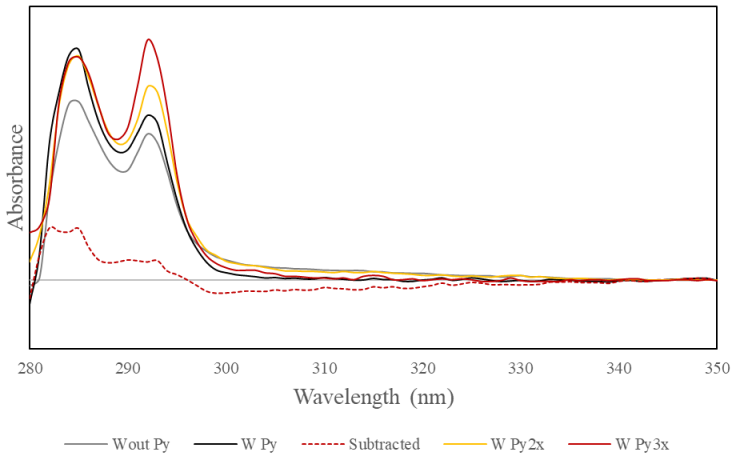

Figure 45: Ultraviolet visible light spectra of a mixture containing 400 mg of zeolite ZSM5 in 100 mL of cyclohexane as solvent with 0.20 ('W Py'), 0.40 ('W Py2x') and 0.60 ('W Py3x') mmol/g_{cat} of pyridine added.

The proposed solvation effect might happen due to the similar structure cyclohexane has compared to pyridine, what could also occur in CPO. These three molecules share a geometry which favors their intermolecular interactions [159, 160]. ACE in the opposite direction, does not have a geometry favoring such interaction and in the presence of pyridine its catalytic activity drops progressively. So, a synergy among cyclohexane, cyclopentanone and pyridine can explain the reason for its non-titrant behavior over CPO-condensation. Another possibility resides in the stronger adsorption of cyclopentanone and for this step be the rate limiting step in zeolite Y. Even with high pyridine loadings the competitive adsorption hypothesis exists due to the observed plateau in CPO consumption over Y30. Due to the large volume of Y supercages the existence of cyclohexane, cyclopentanone and pyridine is possible and a solvation effect perturbing pyridine adsorption might occur. Once CPO adsorption is a possible rate-limiting step for CPO condensation as discussed previously, a weakening of the pyridine adsorption strength competing simultaneously with CPO adsorption opens the possibility of its continuous reaction over an acid site even with the presence of a titrant specie. Some future

studies in this regard could comprehend of using different titrant and also different solvents to investigate their effect on pyridine solvation and titration over acid sites in porous catalysts, e.g., toluene. Toluene and pyridine share a planar conformation favoring the interchanging electron clouds interactions which could favor pyridine desorption and higher concentrations at liquid phase [160-162].

2.4.3.2. Pyridine Effect on Cross-condensation Product Selectivity

After understanding pyridine role as a titrant in the presence of both ketones separately, the titration over cross-aldol condensation between the two reactants is analyzed next. Here, pyridine addition can overcome the total number of active sites of the catalyst, while in Na-series it was restricted by the total amount of sites within that material. The results over zeolite Y30 will be analyzed alone once the majority of the previous discussions were done in the Na-Y30 series.

Figure 46 displays the rate of products formation as a function of the pyridine evolution. The shift in selectivity led by pyridine has a more pronounced effect due to the possible interactions the titrant has with ACE and CPO, and due to the lower reactant concentration gradient. A faster change in [C]C vs. [C]A selectivity as in [A]C vs. [A]A is observed, favored by the plateau over the formation of products acquiring CPO as a secondary molecule ([x]C) (**Figure 47**). At higher loadings the shift in [C] products occurred, not observed previously. It seems, pyridine impedes ACE electrophile attack over the formed enol while CPO continuously condenses throughout the whole range of titration.

The MTL discussion remains analogous mainly when it is noted the same products preference in both MTL region and kinetic region, with a higher selectivity towards [A]C and [C]C compared to Na-titration. At this point, it is fair to assume a better titrant behavior from pyridine in tailoring selectivity when both ketones were cofed if compared to Na-titration.

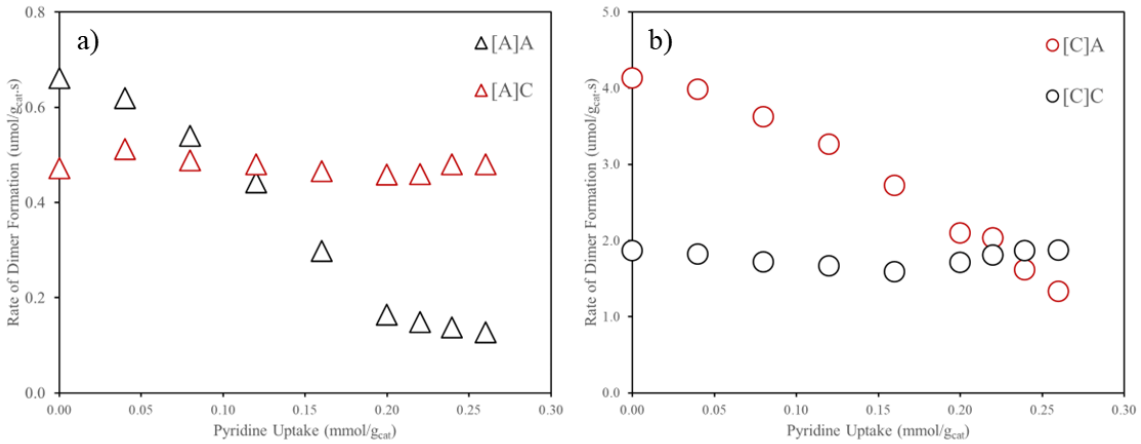

Figure 46: Rates of products formation as a function of pyridine uptake in Y30 zeolite in respect to [A] products (*'a)'*) and [C] products (*'b)'*).

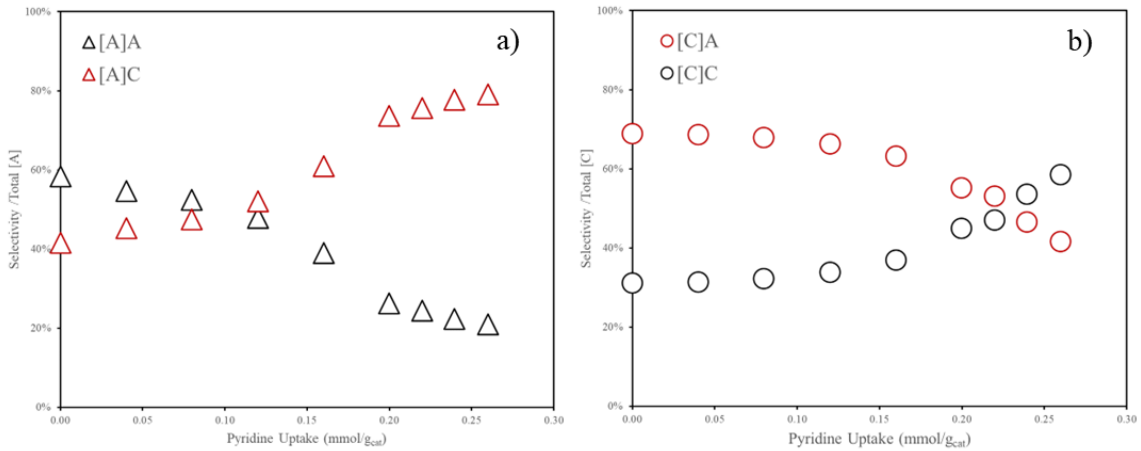

Figure 47: Selectivity distribution of cross-aldol condensation of ACE-CPO in Y30 through in-situ pyridine titration.

2.5 Conclusion

The study of mass-transfer limitations on acid catalysts using the proposed experimental titration approaches and diffusion-reaction modeling proved effective in representing the catalytic drop as the density of acid active sites is modified in regard to understanding, quantifying, and controlling MTL over a catalytic system. Over the studied zeolitic structures the Uniform type of titration is the one that realistically represented the titrant distribution along the catalyst volume, whereas the Shrinking Core model was not observed throughout the studied series. Such model can be investigated using a synthesis approach, in where a catalyst is synthesized in two batches, the first at different temperatures to control the particle size at a constant Si to Al feed (and a resulting constant concentration of active acid sites) and a secondary diffusion-only volume grown at the outer surface of the first particle simulating what is described for the Shrinking Core model as titrant is added. Each synthesized catalyst would have a corresponding activity and could be compared to the expected modeled curve.

Both Na-exchanged ZSM5 series modeling results presented higher mass-transfer limitation values for CPO self-aldol reactivity than for self-ACE reactions. The molecule size seems to be the determining factor inside the 5.4 Å MFI constricted channels which also conferred greater reactivity due to the large volume interaction with the framework structure, also known as confinement effect. As the concentration of acid sites increase by 4-fold in ZSM5 Si/Al of 40 an increase in MTL was also observed, confirming the activity effect in broadening the reactant concentration gradient inside a particle. There, the presence of nearby sites could also have influenced such increase, but further studies in inactivating these pair-sites are required to fully understand their extent as compared to

single sites influence. The use of calcium and cobalt as pair-site titrants seems convenient. Still, fine characterization techniques are required to certify the inexistence of CaOH and CoOH groups that can serve as weaker acid sites that are able to partially activate the reacting species [163]. This is to restrict the titrant role as deactivating pair-sites only. In the Na-zeolite Y series, ACE was affected by MTL, whereas CPO was not. A lower activity for CPO was found and a straight drop was resulted as sites were titrated. The greater volume extent of the supercage did not provide much confinement effect as in ZSM5 to proceed with the observed activities, however the smaller ACE size might had allowed its interaction with hindered sodalite sites which facilitated its consumption as supercage sites were proximate. This hypothesis seems possible once partial interactions were already observed in literature [65]. The use of Na to titrate acid sites and its use to understand the diffusion impacts of each molecule was appropriate and recommended to precisely tune the extent of MTL of a catalyst system.

Regime control between a mass-transfer and a kinetic-limited system was investigated in the Na-Y30 series in the cross-aldol condensation of ACE and CPO. In the Na-free catalyst, e.g. in the presence of MTL, the product preference sequences of [C]A > [C]C and [A]A > [A]C were observed and explained by the faster ACE diffusion and thus lower concentration gradient inside the faujasite catalyst volume. As Na-exchange levels were raised, a shift was observed in the ACE-activated products, and a similar [C]A and [C]C maximum formation rate was found. It seems that as kinetics controls the activity in catalytic site environments, a C-C coupling with a nearby CPO is more favorable. The reactions over both ZSM5 series showed this preference with a slight increase in the percentage of CPO selectivity in a Na-exchanged catalyst, however, it must be

acknowledged that the extent of MTL found in the self-condensation results could have increased over the cross-condensation reactions due to a higher presence of reacting species around the active site. Even though, tuning the MTL extent with Na, once is able to favor the reaction over a preferential product as shown.

When pyridine was used as a titrant agent during the self-aldol condensation of both ketones, reversible adsorption was detected, which was not expected. Two factors were used to explain the pyridine desorption: a solvation effect caused by its similar shape with cyclohexane, and a competitive adsorption with the reacting ketones. In the last, at similar concentration of pyridine uptake, cyclopentanone retained a higher rate of consumption indicating to have a stronger effect of adsorption inside the ZSM5 channels. In the analysis of the higher BAS concentration zeolite (ZSM5 Si/Al of 40), the desorption effect was more pronounced, highlighting the stronger preference of CPO adsorbing in confined acid sites as compared to pyridine. However, its use in the cross-condensation of cyclopentanone was more effective as compared to Na. The regime control provided by pyridine allowed at higher loadings a preference towards more kinetic relevant products showing a direct shift in the CPO active products, which did not occur in Na-titrated series results. Na-exchanged was limited by the amount concentration of sites whereas pyridine addition occurred as it pleased. Pyridine might also had restrained ACE adsorption and further reaction, being competitive with CPO only. Still, the behavior observed by the Na- results were reproduced using pyridine, proving its performance in controlling MTL.

In summary, the proposed experimental approach together with the titration modeling served well in representing the catalytic behavior in acid zeolites. Na was an effective cation to quantitatively titrate and determine the MTL extent in a zeolitic structure

whereas pyridine was successful in qualitatively switch the governing regime to favor the formation of more kinetic relevant products. The stronger adsorption of CPO still a concern in pyridine uptake once the change in selectivity was due to both decreasing the concentration gradient of the reacting molecules and also restricting ACE adsorption.

Chapter 3 – MFI Synthesis: A Particle Size Effect Over Ketone-Condensation and Diffusivity Perspectives

3.1 Introduction and Literature Review

It is not recent that catalyst synthesis studies are used to optimize process efficiency Those studies investigate individual systems, focusing on their fundamental comprehension by analyzing either the reaction chemical aspects or the physical particle properties [164-166]. Both aspects differently impact the results, requiring particular examination. In zeolites, extensive research has been done in the last decades aiming at the design of catalysts with improved thermal stability, longevity, and activity [167-172]. All these aspects point in a direction where the framework structure should permit molecules diffusion without constraint, unless secondary reactions resulted from high residence times are desired.

The influence and impact of mass-transfer limitations (MTL) over ketone-condensation at reaction conditions were shown for the commercial MFI zeolite with different Si/Al ratios. However, it was not feasible to make any direct comparison because of differences in particle size, and the conclusions were directed to each zeolite specifically. The control of these particle physical parameters are of a great importance and commonly done during catalyst synthesis or catalyst post-treatments. The last in rather drastic and not well controlled as compared to synthesis. In example, methods focusing on creating mesoporous pathways significantly diminishes diffusion limitations [15, 173-175]. Desilication is one resource used to generate mesoporosity, consisting of a chemical treatment under alkaline conditions [176, 177]. The drawback stands in the poor catalyst's

stability under severe chemical and thermal treatments [178]. Alternatively, this mesoporosity could also be managed to be produced through an incorporation of polymer or surfactant particles during the synthesis, which can be bound with the framework structure in the presence of -SiO_3 functional groups; the organic content are further removed with thermal treatments [179].

Due to the impact on catalyst stability, synthesis stands as the preferred route for fundamental studies on particle properties. Besides controlling operational parameters, a key element in synthesis is the molecule responsible for directing crystal growth, known as the structure directing agent (SDA) [180, 181]. Each individual zeolite requires a particular SDA in which the silicon-alumina bonds are formed around its spatial arrangement (or molecule volume), and in which the proton settles around the charge position within this agent molecule [180]. These primary building units are formed during the nucleation step, and with enough energy provided, their growth occurs, resulting in a particle sufficiently stable to not rupture under thermal or mechanical treatments [182]. Not last, the feeding amount and chemical conditions these molecules are exposed to are essential to the resulting crystal, with enhanced properties.

The synthesis of zeolite nanoparticles also ensures the minimal diffusion path possible for reactive species in a catalyst particle. One way to obtain smaller size particles was found through controlling the SDAs amount and type during MFI synthesis [183, 184]. Soltanali et al. showed that the concomitant feed of tetra propylammonium bromide (TPABr) and hydroxide (TPAOH) resulted in different crystal sizes as the ratio between these templates changed. An amorphous solid was obtained when TPABr was fed alone, resulted from a decrease in synthesis gel alkalinity, an essential condition for crystal growth [185]. There,

transmission electron microscopy (TEM) images showed the formation of a single crystal rather than aggregates, as one might suggest based on images generated through scanning electron microscopy (SEM) (**Figure 48** and **Figure 49**). The drawback on the nanocrystal synthesis resides on the use of large amounts of organic templates, resulting in substantial economic and environmental impacts.

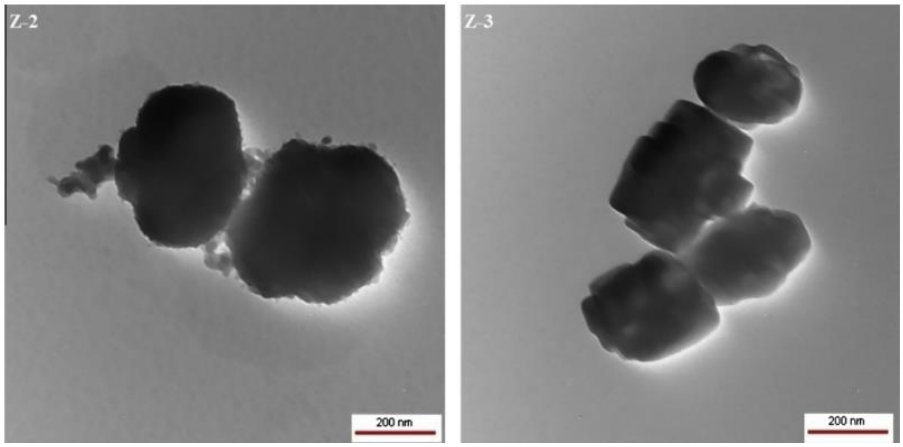

Figure 48: Transmission electron microscopy images of nano ZSM-5 samples Z-2 and Z-3. Reproduced from Ref [183].

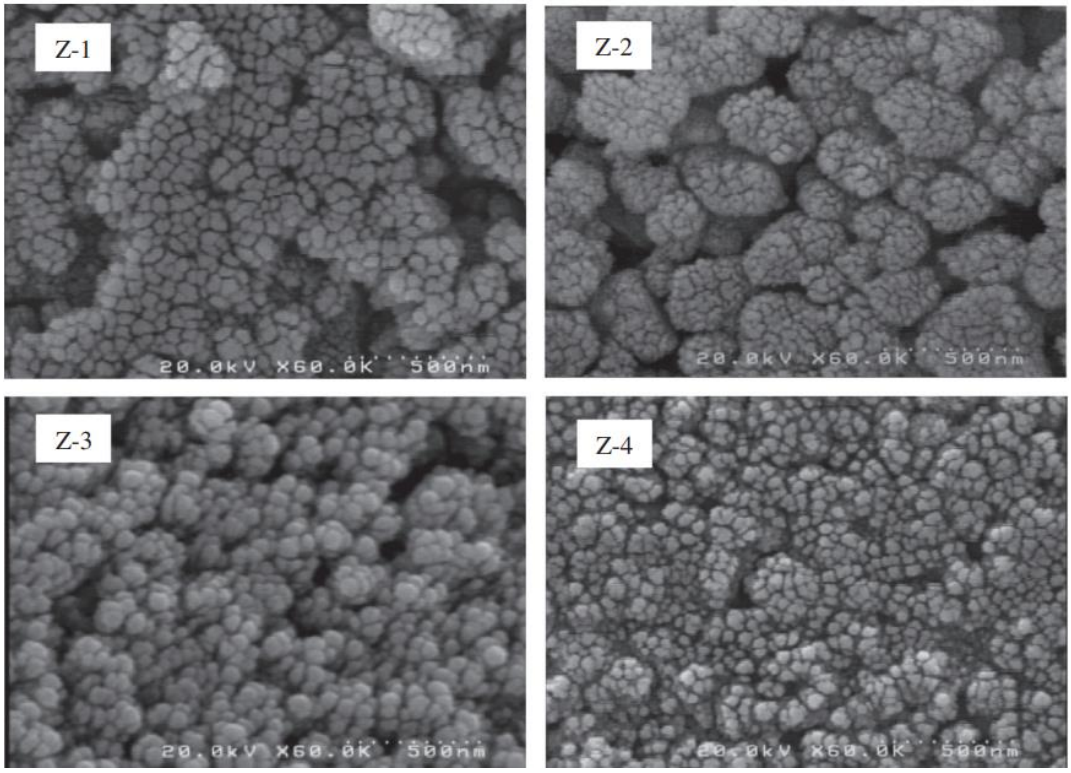

Figure 49: Synthesized ZSM-5 zeolites FE-SEM images in various template ratios. Adapted from Ref [183].

Aluminum as well does play a key role in the crystal formation besides its incorporation on zeolite framework. It has been shown that higher aluminum contents cause the formation of multi-nuclei sites in the synthesis gel inducing several small particles growth whereas fewer single nuclei exists where a small or no aluminum is present [186-188]. These numerous nuclei result in a rough surface, as shown in **Figure 49**, and are avoided at lower Al content; this is an expected result, as a single nucleus growth occurs more homogeneously as the nutrients are slowly incorporated without the interference of a secondary nucleus nearby [189, 190]. Such aluminum control is also beneficial to the absence of extra-framework alumina, existed in early stages of zeolites formation, amorphous silica-alumina solids or at high loadings [191, 192].

Similar to nanoparticle studies, the work performed by Dai et al. involved the growth of rough protrusions (so-called "fins") over the exterior surface of a particle with

identical crystallography [193]. **Figure 50** shows how the fins are likely to be distributed along the seed particle. A 2.5-fold decrease in benzene residence time was observed as the fins were introduced, but as the distance between the protrusions increased a proportional increment in residence time occurred.

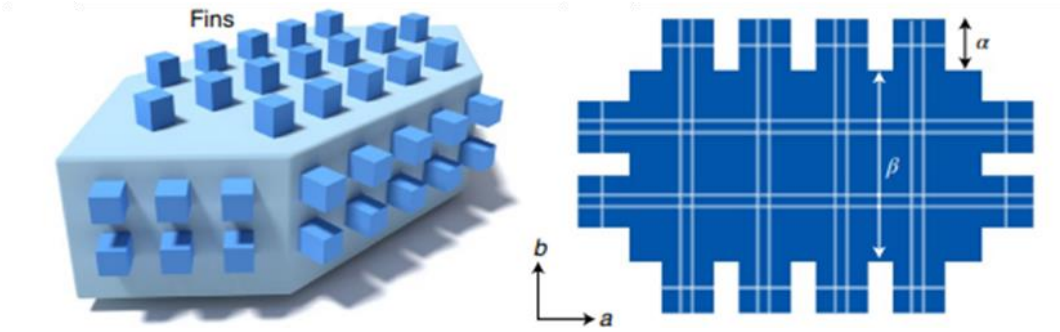

Figure 50: Idealized schematic of a finned zeolite in which the fins have the same crystallographic registry as the seed (left image). Illustration of a finned zeolite that comprises continuous channels throughout the seed (size β) and fins (size α) with characteristic fin dimensions of α×α×α. Adapted from Ref [193].

All these results summarize diverse designed systems with enhanced diffusion. Different paths could be taken however synthesis seems to be the appropriate way to efficiently comprehend diffusion effects on ketone-condensation. The goal here is to control the particle dimensions through zeolite synthesis maintaining constant other structural aspects to investigate their effects on diffusion limitations. The Na-titration approach will be used to quantify the MTL extent existed on each synthesized zeolite.

3.2 Experimental Methods

3.2.1 Chemicals and Materials

The chemicals were purchased from Sigma Aldrich and used as provided: acetone (HPLC grade, >99%), aluminum (III) hydroxide (reagent grade), cyclohexane (HPLC grade, 99.9%), cyclopentanone (>99%), phenol (>99%), tetraethyl orthosilicate (TEOS, reagent grade 98%), and tetra propylammonium hydroxide (TPAOH, 1.0M in H_2O).

3.2.2 MFI Synthesis

In order to obtain the desired particle size appropriate for the proposed study, the molar synthesis ratio was adopted: 1 SiO_2: 0.025 Al_2O_3: 0.4 TPAOH: 10 H_2O: x $NaNO_3$ where x stands for the Na molar ratio used during the course of the study. The synthesis was performed in absence of alkaline species (Na^+, K^+, e.g.) in the mixture composed mostly of deionized water, aluminum hydroxide and TPAOH in a stirring polyethylene container. The stirring remained until a clear solution was obtained. TEOS was slowly added into the mixture and stirred overnight at room temperature to ascertain the complete hydrolysis of TEOS, and more water was added to compensate for the loss. The gel mixture was transferred to a 30 mL Teflon-lined autoclave and heated at the crystallization temperature for 24 hours. After cooling, the solid content was washed 4-5 times to remove solution impurities and dried overnight at 80 ^oC under vacuum environment. Calcination was further performed to obtain the H-form at 550 ^oC for 8 hours to remove the carbon content within the SDA.

3.2.3 Zeolite Characterization and Catalytic Reaction Measurements

Site density quantification was done using the isopropyl-amine temperature programed decomposition (IPA-TPD) and the procedure was detailed previously. To

confirm the crystalline evolution for the synthesized zeolites X-ray diffraction was conducted on a D8 Series II X-ray diffractometer BRUKER AXS, in reflection geometry using CuKα radiation generated at 40 kV and 35 mA in the 2θ = 2-70° diffraction angle range. A commercial MFI sample purchased from Zeolyst International (CBV 28014, Si/Al=140) was used as a standard for crystallography comparison. To evaluate particle size Scanning Electron Microscopy (SEM) images were taken in a Zeiss NEON 40 EsB Field-Emission Scanning Electron Microscope at an accelerating voltage of 5 kV.

Liquid phase batch reactions were performed in a Mini-Bench Top Parr high-pressure reactor (Model Parr 4565) similar to the one previously detailed. The reaction procedure consisted of adding the solvent (cyclohexane) and the synthesized catalyst in the reaction vessel and heated until reaction temperature. After temperature stabilization the reactant was added, and the reaction time recorded as the temperature was reestablished. Final mixture content and concentration was determined using a gas chromatography mass-spectrometry (GC-MS) and flame ionized detector (GC-FID). Both GC's were equipped with a Zebron ZB-1701 column with dimensions of 60 m x 0.25 mm x 0.25 mm.

3.3 Results and Discussions

3.3.1 Synthesized Zeolite Characterization

A series of MFI zeolites were synthesized varying the temperature from 150 to 165 ^{o}C during the crystallization step, maintaining constant the Si/Al ratio and other operational conditions. The characterization methods performed will be analyzed separately as the course of the work is discussed and needed. The S-ZSM5 notation will be used to refer to synthesized zeolites.

3.3.1.1 X-Ray Diffraction

The X-ray diffraction crystallography pattern of the four synthesized batches are shown in **Figure 51**. The commercial sample purchased from Zeolyst International of ZSM5 with Si/Al of 140 is used as a standard pattern for comparison matters. The characteristic peaks to MFI structure are in good agreement with the S-ZSM5s and the commercial sample. Based on this, it is fair to assume that at 24 hours of crystallization the catalyst particle is already stable and well crystallized. A successful synthesis is achieved using the proposed synthesis method.

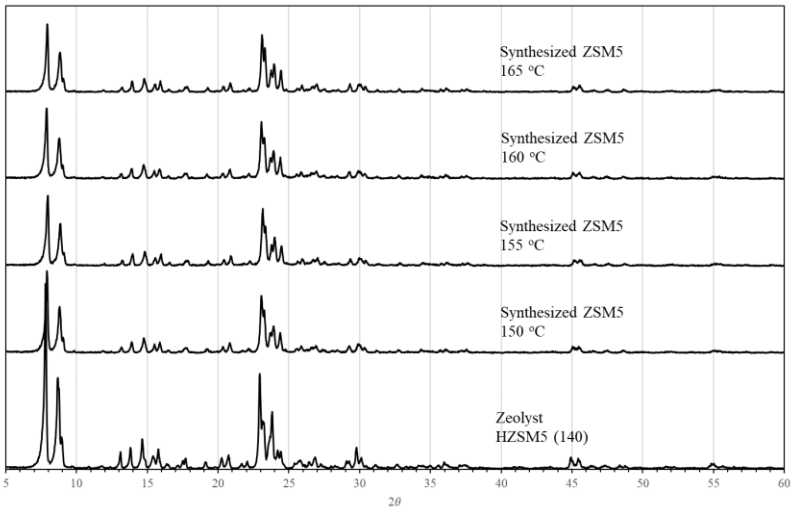

Figure 51: X-ray diffraction spectrum of synthesized ZSM5 zeolites and commercial ZSM5 sample.

To understand the effect of aging time, longer crystallization periods were performed with 72 and 120 hours at the temperature of 150 ^{o}C. The X-ray diffraction spectra in **Figure 52** confirms that in at 24 hours the crystalline structure is detailed enough to confirm the crystallinity pattern for ZSM5 but not as much defined as in 72hrs of crystallization.

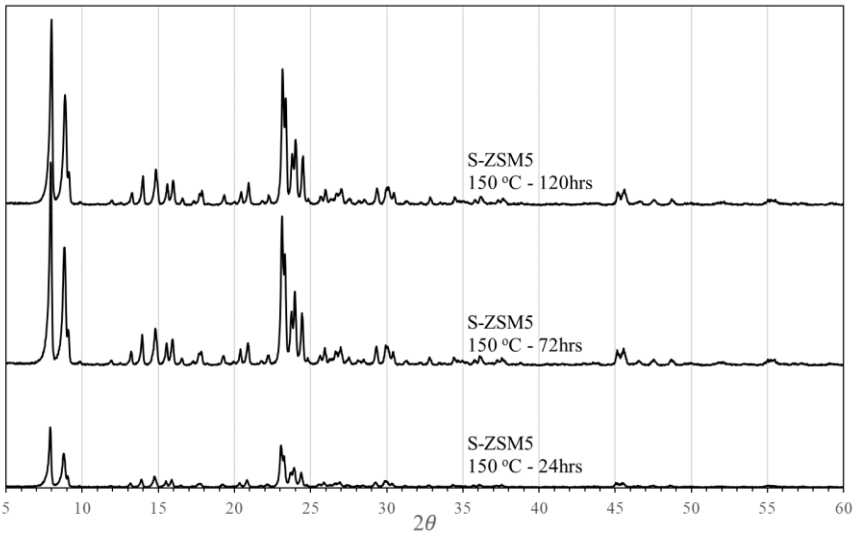

Figure 52: X-ray diffraction spectrum of synthesized ZSM5 zeolites at 150 ^{o}C with different crystallization periods.

3.3.1.2 Side Density Quantification

Besides the crystallography pattern, Al incorporation is also important in this work. The synthesis method must be successful to integrate an unchanging Si/Al ratio as that fed to the mixture gel. With an initial Si/Al of 80 a theoretical Brønsted acid site (BAS) density of 0.206 mmol/g_{cat} is obtained. Once the samples do not use any alkaline metal during synthesis, after calcination the catalysts will be in the H-form and ready for site density measurements. Calculating the site concentration after sample calibration using each respective propylene MS signal (shown in **Figure 53**), an average of 0.20 mmol of protons

per gram of catalyst is found with low deviations among the samples (± 0.01 mmol/g_{cat}). With this, the present synthesis method is efficient in preserving the Al incorporation.

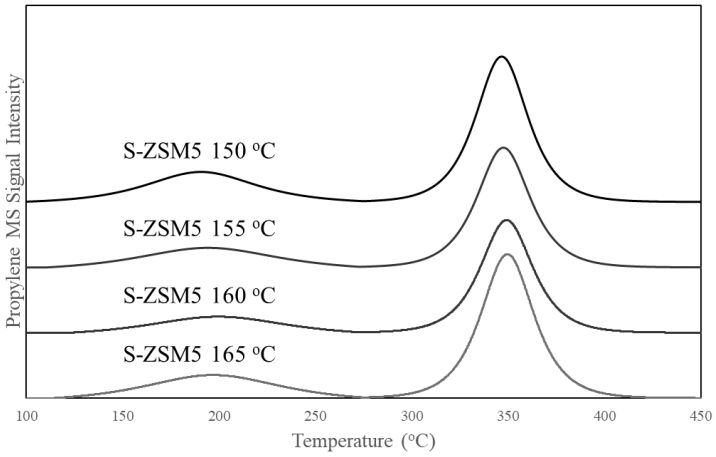

Figure 53: Temperature programmed decomposition of adsorbed isopropylamine (IPA-TPD) on four synthesized ZSM5 samples. Propylene evolution in a 10 K/min heating ramp from IPA-saturated samples.

3.3.1.3 Scanning Electron Microscopy

It is expected that a difference in the particle size appears as crystallization temperature changes. For such, Scanning Electron Microscopy (SEM) images were taken to observe dimensional and surface differences. Using two different magnifications **Figures 54** and **55** show structural features of the four batches of S-ZSM5. It is noted that a homogeneous distribution of particle size in each batch with an average size of 480 nm is all the samples (**Figure 54**). Similar to what was observed in Dai's et al. work, small protrusions are deposited over the outer surface of the main particle and, here, their size changes as a function of temperature [193]. These particles are solely formed during the crystallization step, while after nucleation, before transferring to the Teflon-lined, a homogeneous, dense, and clear gel is obtained. Thus, no solid formation. The low temperature and slow mixing during nucleation assure only the homogeneous distribution

of nutrients and formation of the primary units, with a lack in energy to overcome the crystallization barrier and thus form small particles.

Table 9 presents the average size of the observed small aggregates as well as the respective BAS for each S-ZSM5 zeolite. The uncertainty shown next to the particle size values represents the standard deviation of more than 30 measurements for each sample within the SEM operational program. An increase in the average size is clear and reactivity will be further analyzed.

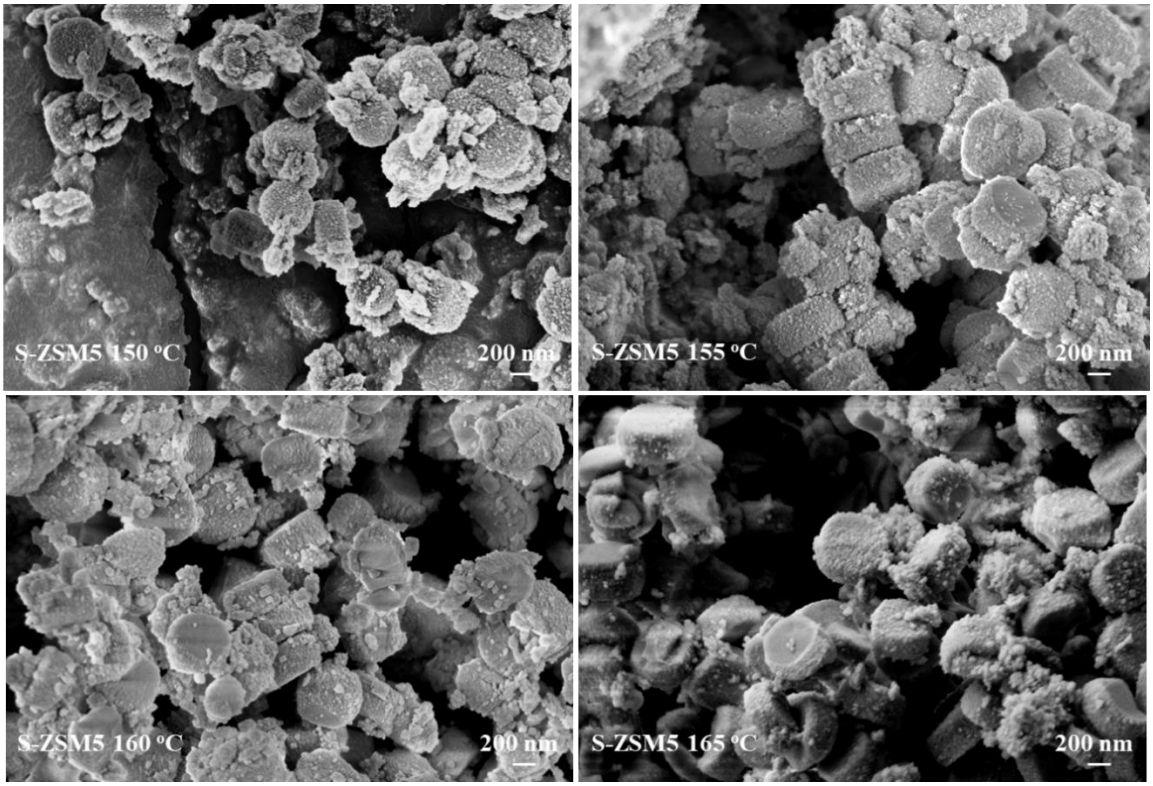

Figure 54: Scanning Electron Microscope pictures of four S-ZSM5 (Si/Al =80) at similar magnification (27 KX).

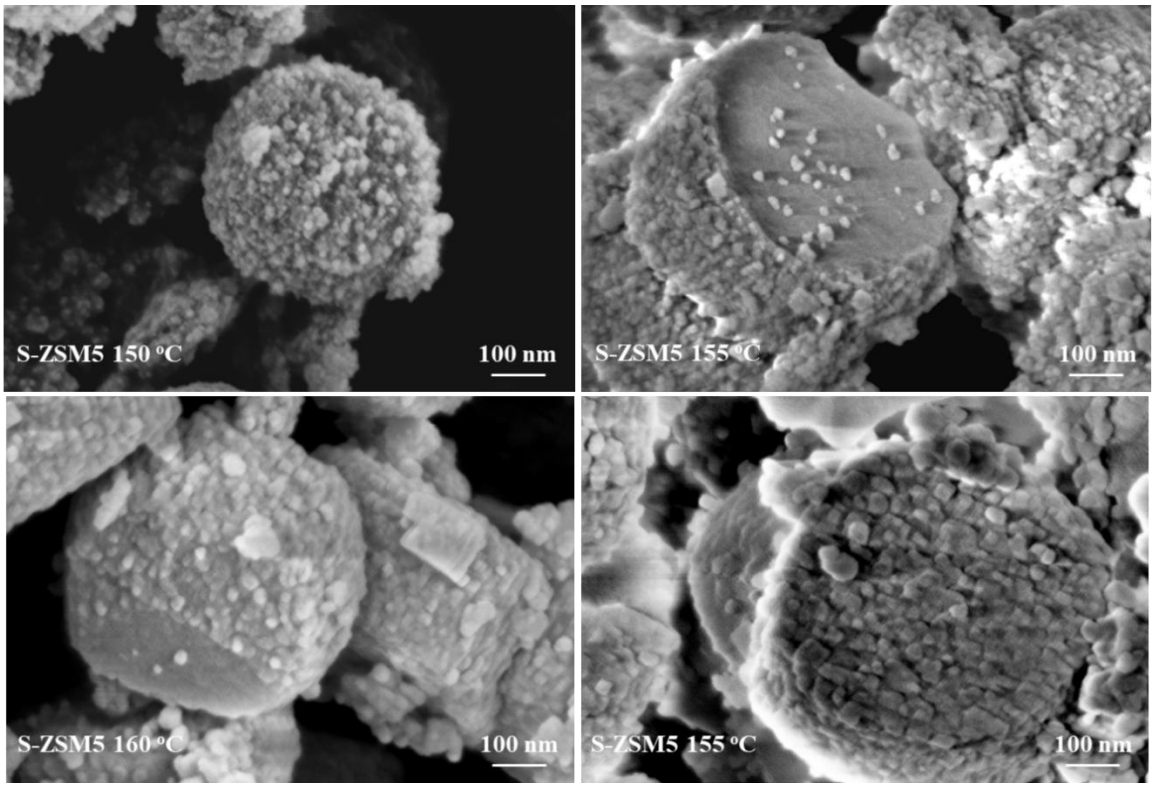

Figure 55: Scanning Electron Microscope pictures of four S-ZSM5 (Si/Al =80) at similar magnification (120 KX).

Table 9: Site density and average particle size of the synthesized ZSM5 zeolites.

	Batch	IPA-TPD BAS ($mmol/g_{cat}$)	Small Particle Size Average (nm)	Main Particle Size Average (nm)
	1st	0.20		
S-ZSM5 150 °C	2nd	0.20	16 ± 2	479
	3rd	0.19		
S-ZSM5 155 °C	-	0.21	21 ± 3	492
S-ZSM5 160 °C	-	0.20	28 ± 3	473
S-ZSM5 165 °C	-	0.20	33 ± 5	488

While the crystallography patterns for the S-ZSM5 samples with 72 and 120 hours of crystallization time showed to be more characteristic than those compared to 24 hrs, the SEM pictures exhibit no major differences (**Figure 56**). The average particle size for 72 and 120 hrs are 473 and 468 nm considering the whole particle volume, and 27 (± 2) and 31 (± 3) nm for the small aggregates on the outer surface. The well-developed XRD spectra

and a very similar morphology and structural dimensions confirm that at 72 hours of crystallization most of the nutrients responsible for the crystal growth are consumed. Once the goal is to analyze the effect of particle size in reactivity, the crystallization period of 24 hours is considered enough to have a well-developed crystallography to be characterized as MFI.

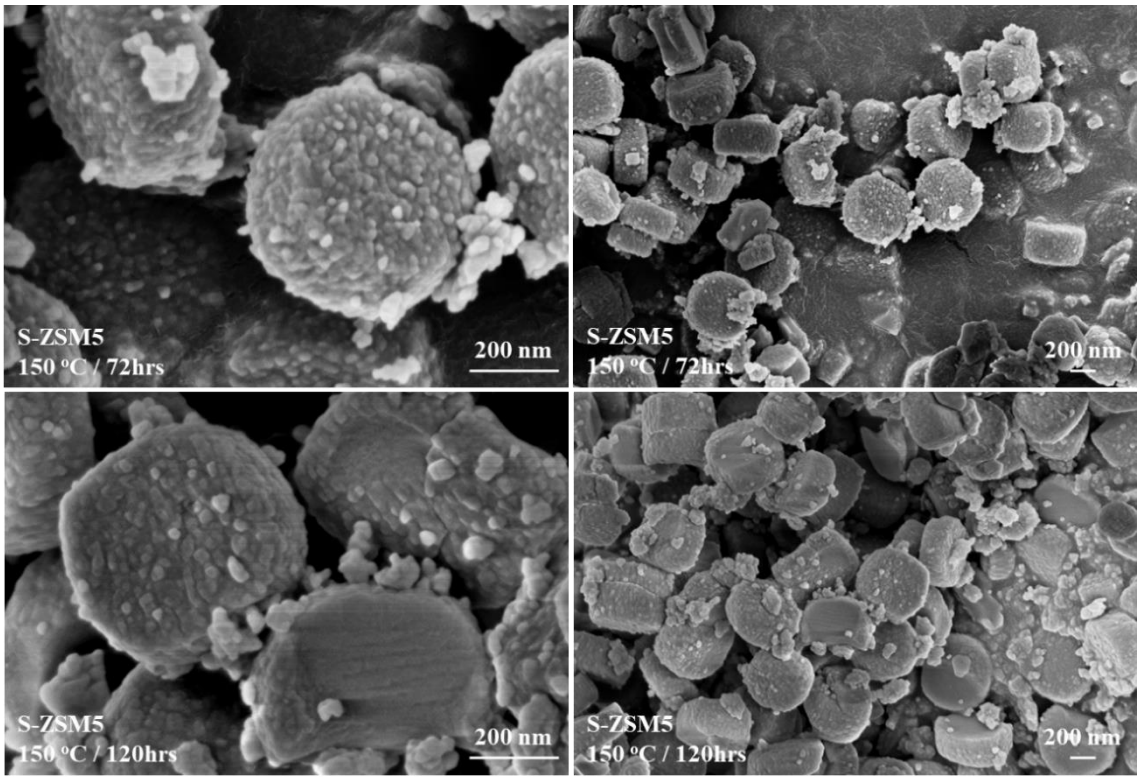

Figure 56: Scanning Electron Microscope pictures of S-ZSM5 150 °C (Si/Al =80) at different crystallization periods (72 and 120hrs).

3.3.2 Catalytic Activity and Diffusion Discussions

In the previous chapter, the self-aldol condensation of acetone and cyclopentanone were used as model reactions to quantify the extent of MTL in different catalysts. In those experiments, low conversion levels were maintained to avoid catalyst deactivation and equilibrium effects, using conversion as a fingerprint to identify possible diffusion limitations in catalyst activity. If MTL is absent in a particular range of particle size, no

effect on rate or conversion exists due to a non-variant internal diffusion rate in the studied catalyst. However, if a drop in rate is observed, an existing concentration gradient drives the course of reaction and as particle size increases, a resulting decrease in catalytic activity occurs. This was noticed in the four S-ZSM5 series, as shown in **Figure 57**.

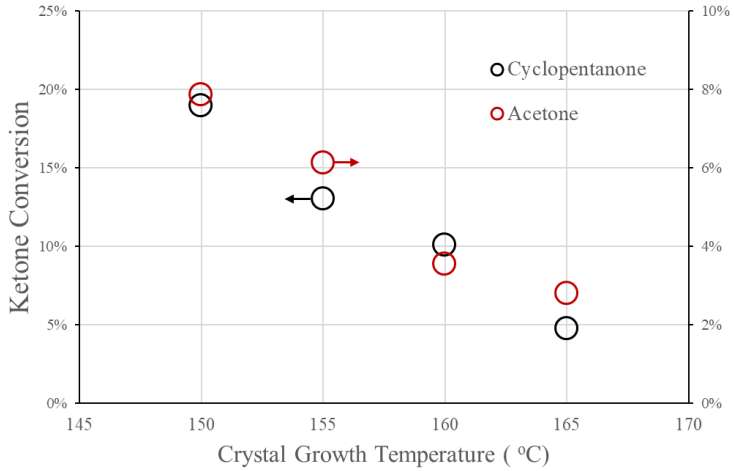

Figure 57: Self-aldol condensation rates of acetone and cyclopentanone over S-ZSM5s. Reaction conditions: 250 ºC, 1 mol/L feeding reactant, 1 hour of reaction time. 250 mg of catalyst.

From the observed results and catalysts characterization it can be inferred a major contribution coming from the small aggregates on activity, once no change in the overall particle size is seen and active site density is constant. This assumption is also supported by the catalytic condensation reactions with the S-ZSM5 150 ºC samples with 72 and 120 hours (**Figure 58**). A constant conversion with similar particle sizes and in the same range as the S-ZSM5 at 160 and 165 ºC implies that, in the present synthesis procedure and feeding amounts, the nutrients are fully consumed and no particle growth exists, resulting in constant conversion.

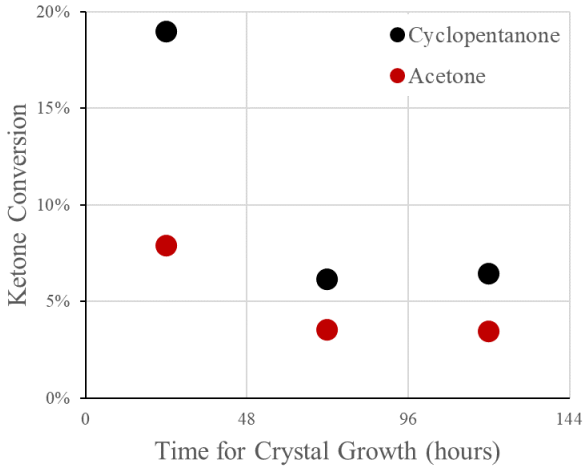

Figure 58: Self-aldol condensation rates of acetone and cyclopentanone over S-ZSM5s with different crystallization periods. Reaction conditions: 250 ^{o}C, 1 mol/L feeding reactant, 1 hour of reaction time. 250 mg of catalyst.

3.3.2.1 MTL Assessment on S-ZSM5 Zeolites

The presence of MTL is investigated by generating a Na-titrated series on the S-ZSM5 at a constant crystallization temperature of 150 ^{o}C. The procedure consists of a usual synthesis method, followed by calcination and the application of $NaNO_3$ with different salt concentrations. This procedure was previously studied and proved to be efficient in determining the amount of MTL that exists in a zeolitic system. **Table 10** shows the active site density and respective consumption rates of acetone (ACE) and cyclopentanone (CPO) of each synthesized and Na-exchanged sample, and **Figure 59** plots the consumption rate versus concentration of titrated acid sites.

Table 10: Site density and consumption rates of Na-titrated S-ZSM5 150 ºC.

Na/H	BAS IPA-TPD ($mmol/g_{cat}$)	Titrated sites ($mmol/g_{cat}$)	%Titrated Sites	ACE Consumption Rate ($\mu mol/g_{cat}.s$)	CPO Consumption Rate ($\mu mol/g_{cat}.s$)
-	0.20	0.00	0%	8.2	21.9
1	0.14	0.06	31%	6.0	15.8
2	0.12	0.08	39%	5.8	19.0
4	0.11	0.08	43%	5.0	18.1
10	0.08	0.12	59%	4.1	13.2
19	0.08	0.12	62%	4.2	11.5

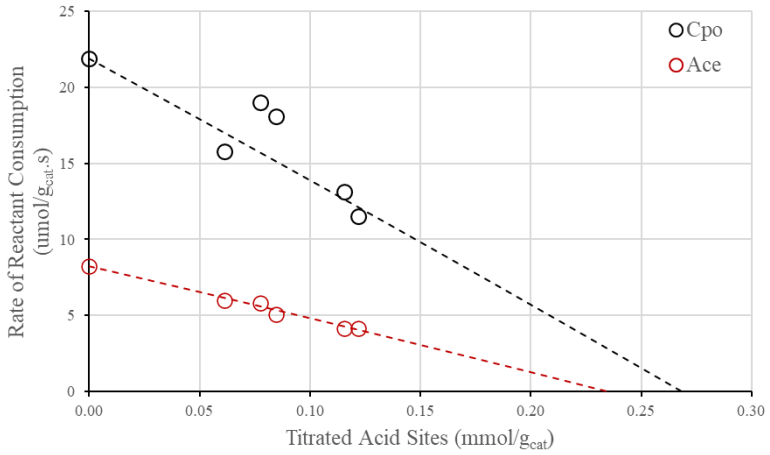

Figure 59: Self-aldol condensation rates of acetone and cyclopentanone over Na-titrated S-ZSM5 150 ºC samples as a function of titrated acid sites. Reaction conditions: 250 ºC, 1 mol/L feeding reactant, 1 hour of reaction time. 250 mg of catalyst.

Due to the variation in conversion as the aggregate size changed, MTL is found to be present in both ketone systems. The Thiele modulus found for ACE and CPO are 0.9 and 2.2, respectively, which are considered low and very close to an MTL-free regime mainly in acetone. However, due to the observed drop in reactant consumption, an increase in diffusion limitations is inferred. Theoretically, we can observe the increase in this extent using the Thiele modulus equation and its proportional correlation with particle radius ($\phi_{d_{p2}} = \phi_{d_{p1}} \frac{R_2}{R_1}$).

For a higher Thiele Modulus, a lower effectiveness factor ($\eta = \frac{r_{obs}}{r_{max}}$) is followed. Since these zeolitic systems are intrinsically identical, r_{max} is fixed, and a decrease in η is resulted from a drop in r_{obs}. Using these assumptions and correlating the equation with the experimental values, theoretical values for Thiele modulus and effectiveness factor are found, presented in **Table 11** and graphically in **Figure 60**.

Table 11: Calculated Thiele moduli and effectiveness factors for the S-ZSM5 series.

S-ZSM5 Sample	Acetone			Cyclopentanone		
	Consumption Rate (μmol/g_{cat}.s)	ϕ	η	Consumption Rate (μmol/g_{cat}.s)	ϕ	η
150 ºC	8.2	0.87	0.95	21.9	2.20	0.78
155 ºC	6.8	2.13	0.79	14.5	4.56	0.51
160 ºC	3.9	5.33	0.46	11.2	6.36	0.40
165 ºC	3.1	7.16	0.36	5.3	14.99	0.19

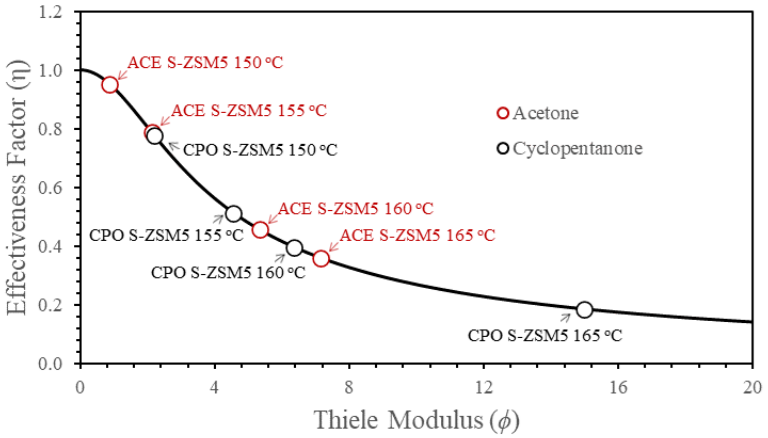

Figure 60: Theoretical Thiele modulus and correspondent effectiveness factor calculated based on consumption catalytic rates of acetone and cyclopentanone.

Therefore, the observed decrease in the 150-165 ºC S-ZSM5 samples points to a decrease in the effectiveness factor and an increase in Thiele modulus, theoretically proving the structural influences over zeolite catalytic activity.

To confirm the theoretical higher Thiele modulus with a larger aggregate size, a following Na-titration is performed in synthesized zeolites at the temperature of 160 ºC. Unexpectedly, the behavior is different from what it has been observed for the commercial zeolite series and the S-ZSM5 150 ºC trends, where the drop is sharp and with a lower calculated BAS densities than the value found through IPA-TPD as reaction rate zeros (0.10-0.12 mmol/g_{cat} vs. 0.20 mmol/g_{cat}, **Figure 61**). Cyclopentanone consumption decreases more pronouncedly than acetone (36% drop relative to the Na-free rate versus 24%) relative to the first Na-titrated sample, evidence of its higher dependence on diffusion through the aggregates.

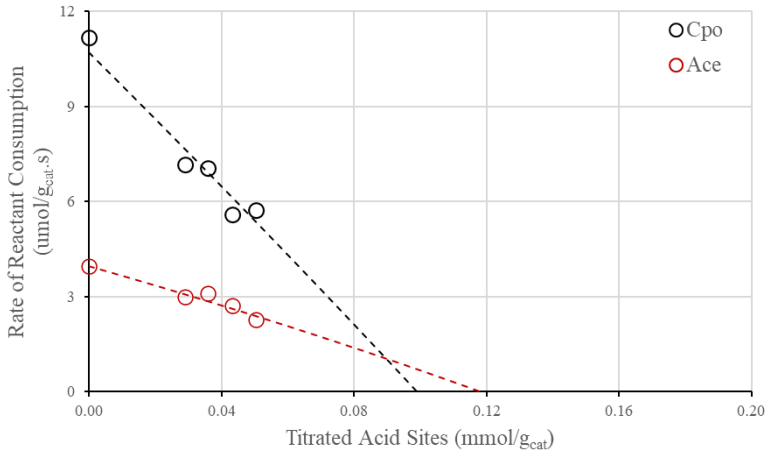

Figure 61: Self-aldol condensation rates of acetone and cyclopentanone over Na-titrated S-ZSM5 160 ºC samples as a function of titrated acid sites. Reaction conditions: 250 ºC, 1 mol/L feeding reactant, 1 hour of reaction time, 250 mg of catalyst.

It is inferred here that a considerable contribution in activity is derived from those small zeolites over the particle surface and as their size increases the activity drops consistently. The assumption is that the titration firstly occurs on the nano-zeolites formed over the catalyst surface rather than through the whole particle as expected. The behavior observed in the Na-series in S-ZSM5 150 ºC is very similar to what was observed with the commercial samples of ZSM5 (Si/Al = 40 & 140) because such contribution in activity

coming from the nanoaggregates is large compared to the big particle, and the titration levels achieved were not sufficient enough to observe the consistent drop. Once in the S-ZSM5 at 160 ^{o}C zeolites the concentration of aggregates are smaller compared to those at 150 ^{o}C any small extent in titration results in a considerable decrease in rate.

Even though the catalytic results did not follow the expectations from the Thiele Modulus equation relation as particle size increases, the greater extent of MTL is interpreted differently and hypothesized to be higher at the S-ZSM5 160 ^{o}C Na-titrated series samples.

3.3.2.2 Na-Effect over Zeolite Synthesis

A second approach is also investigated to understand the effects Na may have during synthesis. At this point Na is assumed to work as a titrant agent and replace the proton, inactivate that specific site location. This occurs mainly in a post-catalyst treatment, after zeolite formation and no extreme condition is applied to force any structural change in the framework. However, due to positive charge in the Na cation it may not operate as a titrant only. The hypothesis stands once TPAOH (MFI structure directing agent) has a positive charge in its center, position in which the Al is said to be located at once TPAOH is preferentially placed at the framework intersections [194-196]. By using Na during synthesis in a water-solution, the existence of Na^{+} may direct the Al sitting in different locations rather than those expected using TPAOH, generating sites in different environments and with possible different catalytic activities [197].

Two S-ZSM5 samples were prepared maintaining the standard synthesis procedure at 150 ^{o}C with added Na loadings calculated based on TPAOH molar amount, being:

Na0.0625 and Na0.25, in which 0.0625 and 0.25 are the mols of $NaNO_3$ added for each mol of TPAOH. No NH_4NO_3 exchange is performed after calcination to restore the protons titrated by Na. In **Figure 62** no structural changes is observed compared to those taken for the S-ZSM5 150 ^oC Na-free zeolite (**Figure 55**, upper left image). The concentration of acid active sites measured by IPA-TPD are 0.065 and 0.099 mmol/g_{cat} for each Na-sample, and the catalytic measurements compared to those formerly shown in **Figure 59** (**Figure 63**).

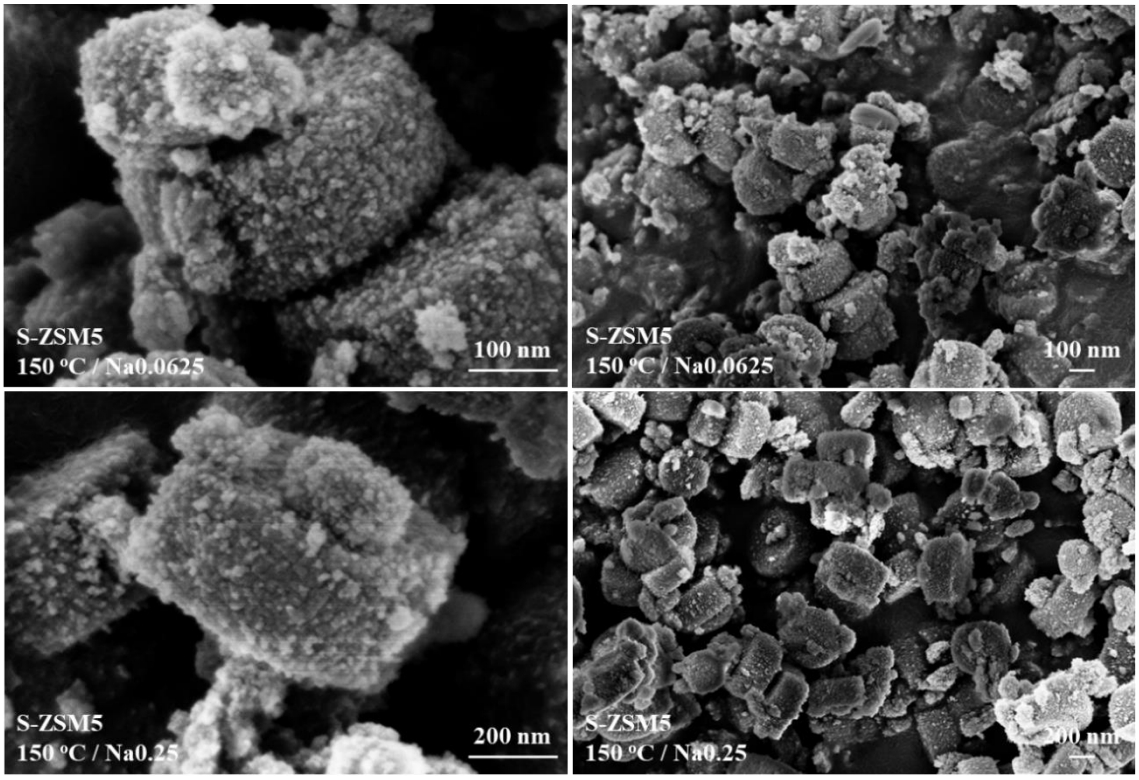

Figure 62: Scanning Electron Microscope pictures of S-ZSM5 150 ºC (Si/Al =80) with different Na loadings (Na0.0625 and Na0.25) calculated based on a TPAOH molar amount.

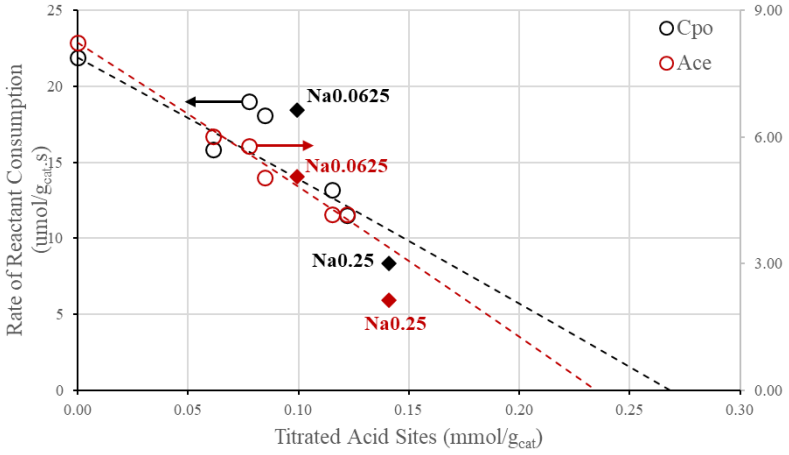

Figure 63: Catalytic measurements of the self-aldol condensation rates of acetone and cyclopentanone with Na-added during synthesis compared to Na-titrated S-ZSM5 150 ºC samples as a function of titrated acid sites. Reaction conditions: 250 ºC, 1 mol/L feeding reactant, 1 hour of reaction time. 250 mg of catalyst.

As observed in the graph, the Na0.0625 catalytic runs for acetone and cyclopentanone condensation are consistent with the S-ZSM5 150 ºC Na-titrated modeled trends, a lower activity is found for Na0.25 assigning a possible pore plugging due to the high loading of Na which impedes molecules diffusion through the pores. Still, the hypothesis of different proton-location inside the channels due to presence of Na is also valid. Higher the Na loadings in the synthesis mixture, higher the probability of an Al sitting in a different location. In the Na0.25 sample for each Al atom in the gel mixture, 8 atom of Na are present, compared to 2 atoms in Na0.0625. Thus, it is possible that Al could be located at different positions in the MFI structure rather than those formerly known due to TPA^-. These sites seem to have an apparent lower activity and differently contribute to activity. In regards of their influence of MTL, a lower extent of diffusion limitations is expected based on the lower catalytic activity. Further studies are needed to support this concept in where relative comparable amounts of Na and TPAOH are fed simultaneously, and catalytic measurements compared to those with post-synthesis Na-exchanged zeolites.

A third possibility in regards of the lower activity in the Na0.25 sample is the sharp drop in rate as observed in the Na-titrated S-ZSM5 160 ^{o}C series. At a certain limit the activity contribution from the small aggregates are minimal and the catalytic rate decays drastically to exhibit the rate relative to the main big particle, assuming a preferential titration occurring first in the nanoaggregates. One way to separate the aggregation contribution over activity is to synthesize a zeolite with a "smooth" surface particle so the activity can be considered homogenous along the catalyst volume, then, a Na-titration technique to observe the rate decay profile. Here, the explanations seem feasible to the presented results, but further studies are required to fully comprehend each hypothesis.

3.3.2.3 Structure Directing Agent Effect on Zeolite Morphology

Up to now, it has been observed the reaction rate dependence on the diffusion through the synthesized zeolites, a combination of the molecule transport in each separate catalyst volume: formed aggregates and bigger support particle in where the aggregates lie on. An increase in the aggregate diameter as shown in **Table 9** resulted in a drop in activity (**Table 11**), showing that it is the determining factor as MTL dominates the limiting regime. In order to observe the impact of the main particle size the template amount added to the synthesis gel is investigated. It is known that template is responsible for directing the zeolite growth towards a well-defined framework structure, and the amount fed within the mixture allows a certain number of nucleation sites prior to crystallization [198]. If a lower amount of template is present during nucleation, fewer growing unit sites will exist, but more nutrients will be available for their growth; this results in fewer number of particles but with a larger size. This assumption is tested with 0.25 and 0.5 the usual amount of

TPAOH added into the synthesis mixture, maintaining constant all the other operational conditions and standard amounts, the crystallization temperature of 150 ºC is used. In the 0.25TPAOH case, no solid was formed. Apparently, this amount of template is not enough to cause the formation of the primary growing units and to sustain a stable crystal size. However, in the 0.5TPAOH, a substantial increase is seen in particle size according to the SEM pictures (**Figure 64**). An increase of 4-fold in diameter (1.9 µm) compared to 1.0TPAOH (0.5 µm; i.e., S-ZSM5 150 ºC zeolite sample) at the same crystallization temperature, but with a very similar shape and surface roughness. With this, the growth and size of aggregates to not appear to be dependent on the template amount, but rather the crystallization aging times and temperature, whereas the main particle size is a result of the number of primary growing units spread along the synthesis volume.

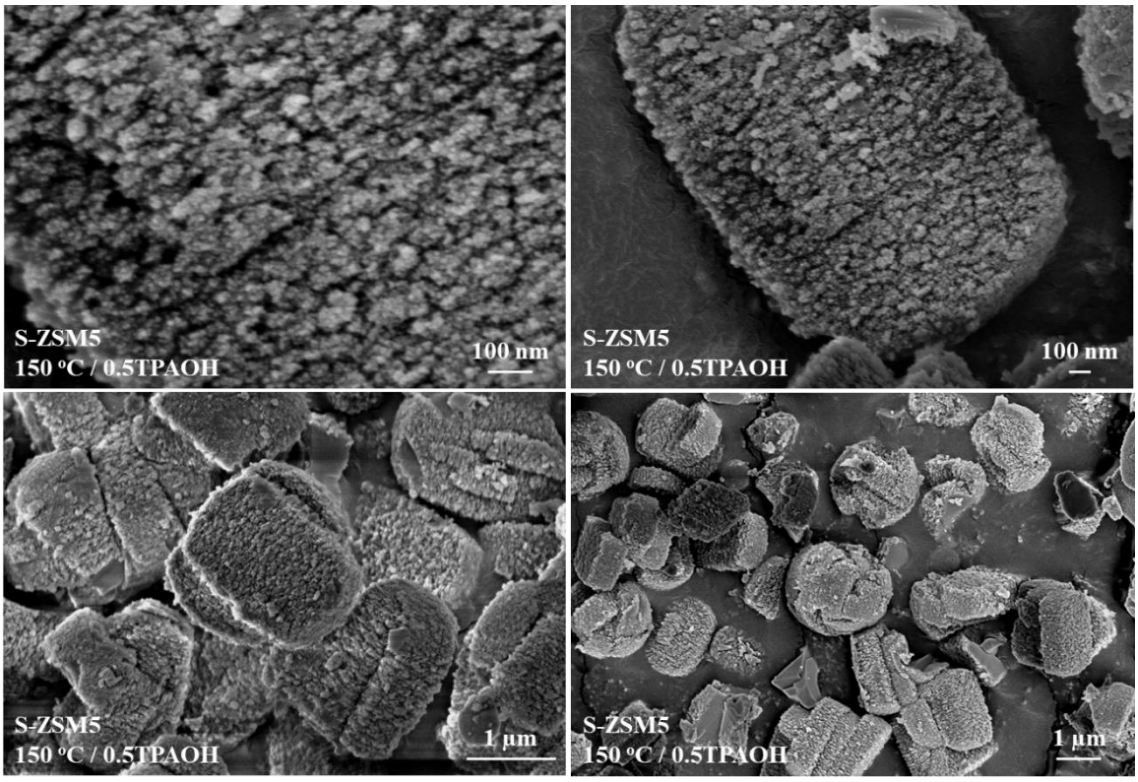

Figure 64: Scanning Electron Microscope pictures of 0.5TPAOH S-ZSM5 150 ºC (Si/Al = 80).

The aldol condensation reactions over the 0.5TPAOH sample showed an acetone conversion of 4.4% compared to 7.4% in the 1.0TPAOH, and 20.6% in cyclopentanone compared to 19.7% respectively. The two observed behaviors require different analyses due to their size and different diffusion inside the constrained MFI framework. The drop in acetone conversion reflects its dependence on the molecule diffusion and reaction through both aggregates and main particle. This is acceptable also because in the Na-titrates S-ZSM5 160 ^{o}C series the drop in acetone was not pronounced as in cyclopentanone. Differently, cyclopentanone activity seems to be dominantly bounded to the nanoaggregates only. Then, larger molecules are shown to be limited by nanoaggregates at the outer surface possibly due to the lower diffusion path compared to the large particle volume, whereas smaller molecules are affected by both catalyst particle volumes (nano and large) but impacted in different extents depending on each size.

3.4 Conclusions

Particle size control through synthesis showed to be a valuable approach to investigate diffusion effects over catalytic rates on zeolites. Here, the proposed synthesis method was able to incorporate the feeding Si/Al ratio throughout the batches in a consistent and homogenous way, resulting in a constant density of Bronsted acid sites of 0.20 mmol/g_{cat} among the samples. Crystallography demonstrated to be well developed at 24 hours of crystallization time where as in 72 hours more defined X-ray diffraction peaks were found. Once the goal is controlling the particle size and observe their change over the temperature range chosen, the 24 hours was chosen as the fixed time for the study.

The activity changed considerably as the nanoaggregates (or nanosized zeolites) sizes over the main surface of zeolite particle changed. Such small dimensions were not expected to be influenced by MTL, but it opens up discussions of their influence even at nanosized confined environments. The observed drop in rate indicates a catalytic activity dependence on the molecule diffusion path along the catalyst material, as a consequence a proportional increment on MTL occurs resulted from an increase on Thiele modulus. The explanation was performed theoretically due to the Thiele modulus correlation with effectiveness factor and its dependence on the observed consumption rates. Once only in this study the zeolitic structure units were intrinsically equivalent, a maximum rate is invariable and thus used to explain the observed results.

The experimental approach developed in previous chapters to investigate MTL was used here. Na-titration over the highest activity synthesized zeolite (S-ZSM5 150 ^{o}C Na-series) presented moderate diffusion limitations which increased as the particle size changed. The titration over the 160 ^{o}C S-ZSM5 Na-titrated series displayed a behavior not

noticed before with a modeled BAS density lower than the one calculated by IPA-TPD. That showed a fingerprint of the nanoaggregate's activity contribution over the overall activity once it was hypothesized the titration preference towards the small catalyst volumes preferably than the main particle.

Decreasing the amount of template during synthesis occurred to increase noticeably the particle size, four-fold compared to what was obtained in a standard synthesis procedure, agreeing with the hypothesized lower amount of nucleation sites and consequently more nutrients left for crystal growth. Cyclopentanone reactivity remained constant whereas acetone dropped, supporting the proposed ketone activity dependence over sections of the catalyst volume.

Chapter 4 – Insights on Hydrocarbon Catalytic Cracking Over Zeolite Y, The Impact of Mesoporosity Introduction

4.1 Introduction and Literature Review

The catalytic use of zeolites in industry is predominantly in reactions involving hydrocarbon synthesis, cracking, and isomerization [51, 199]. While isomerization and synthesis concentrate on mechanistically change the molecule spatial arrangement or elongate the hydrocarbon chain aiming for stable and energetically valuable products, cracking is characterized for breaking large organic molecules into smaller and valuable materials. These three reactions are commonly performed over acid catalysts through primarily generating a positive charge in the hydrocarbon chain, undergoing to one of the three main known routes: (1) a direct protonation of a saturated C-C bond, forming a penta-coordinated carbocation; (2) a protonation of an unsaturated C-C bond, leaving the positive charge close to a more central or branched C; or (3) a proton extraction from a C in the chain, characteristic of a H-transfer to a nearby specie (**Figure 65**). The resulted protonated specie in the last two routes is known as carbenium ion; both carbonium and carbenium ion are understood to be transition state (TS) like species rather than intermediates of the reaction, but for easier comprehension of reaction mechanisms they are commonly shown as intermediates [200].

Frequently, prior to synthesis or cracking, a concerted isomerization occurs for better positioning the positive charge in the molecule chain, followed by a C-C cleavage

step, which depends on the nature of the resulting ionic molecule. This isomerization reaction might also occur due to steric restrictions a porous system imposes over the reacting species, this because of the presence of tertiary carbons within the hydrocarbon backbone provides higher stability and is less energetically demanding for C-C scission when compared to primary and secondary carbons [201]. For this, catalyzed cracking of linear alkanes are expected to undergo skeletal isomerization through a penta-coordinated carbonium ion mechanism for further cracking or either β-C-C bond scission, while branched molecules or olefins usually go through a carbenium ion type of mechanism [202-204]. Still, the fundamental comprehension of the reaction mechanism in confined environments and the impact the elements of a zeolite have over the products formation are a matter of study.

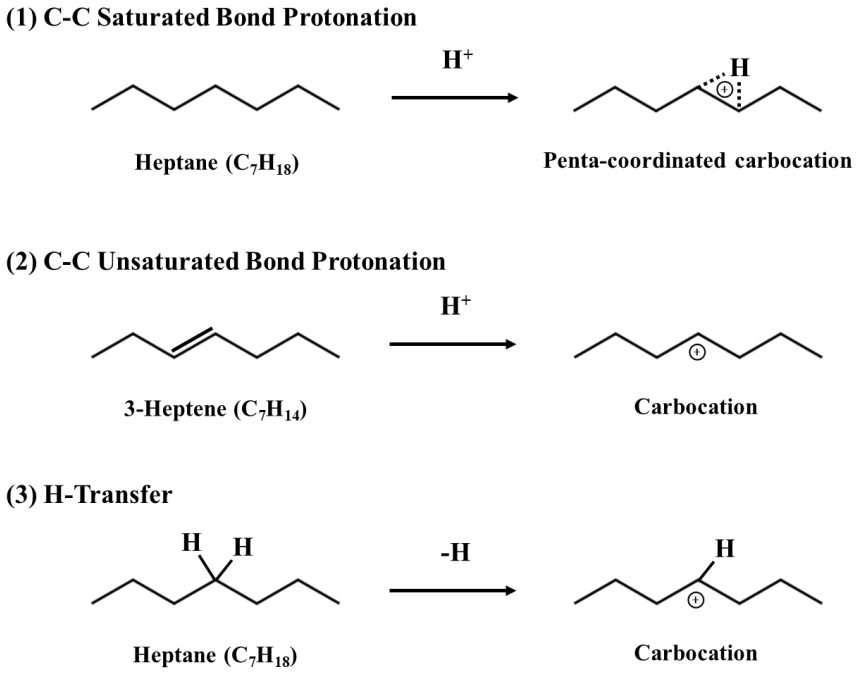

Figure 65: Carbocation initiation in heptane (model molecule), a first elementary step onto catalytic cracking reaction. A model representation.

It is understood, that the product selectivity depends on the nature of the reacting species (e.g., chain length or branched alkyl groups) and the environment around the acid site [205]. In regards of the nature of the hydrocarbon itself, within the same zeolite, cracking rates of different molecules were demonstrated to be determined by entropic differences existed between the (late) TS and adsorbed alkanes rather than difference on mechanistic arrangements of the main hydrocarbon chain [65]. This "late" TS was explained by its arrangement being analogous to the products, resulting in entropic rotational and translations gains, not existed in the longer hydrocarbon chain. The enthalpic contributions from the van der Waals interactions with the framework were found to be similar to both the adsorbed molecule and the TS, in such a way that the entropic contributions were more relevant in cracking reactions under confined domains. These differences in entropy are also observed in the adsorption of these molecules in an acid site as the number of carbons changes. A linear correlation between the enthalpies and entropies of the alkane sorption with the carbon number is found in where higher the molecular weight of the hydrocarbon higher the entropy and enthalpy loss compared to the gas phase [206]. Also, less demanding is the energy requirement for cracking reactions to occur as the number of carbons within a chain increases [207]. Taking advantage of these energy observations in respect to the molecule itself and the interactions contributions a porous catalyst provides, one might find more feasible to profit from these reactions under a confined environment of a zeolite due to the properties and reaction performance control.

The catalytic cracking on zeolites are advantageous due also to the high thermal stability of the crystalline structure and the confinement effect the zeolite has over high energy species. Faujasite (FAU, or zeolite Y) presents itself as an important catalyst to the

industry in this case due to its pore opening, allowing relatively large molecules to diffuse through resulting in high conversion rates as compared to more confined structures [208]. However, the presence of extra-framework aluminum species (EFAL) and their unknown synergistic effects alongside with the acid sites incite the need of the catalyst understanding and upgrading [128]. These features are a consequence of the high Al feeding during Y synthesis, and methods to mitigate their presence are performed both at the synthesis stage or in a post-treatment process, generating further effects as mentioned before in early chapters (e.g., acid washing and steaming). Since the control of operational and chemical parameters during the zeolite synthesis are challenging, post-treatments are selected as excellent approaches to diminish the concentration of such elements.

The aforesaid steaming treatment is commonly performed over catalysts structures to create mesoporous channels inside the framework to facilitate reacting species diffusion and their contact with the active environment sites [209]. As a consequence, diffusion limitations are severely diminished, and the reaction control and its study becomes practical. Indeed product selectivity differences were observed as the pore dimension changed among different zeolites [210]. The observance of lower amounts of large hydrocarbons in more confined zeolites could be explained by the higher tendency of secondary cracking reactions of these species due to their higher residence time inside the reacting catalyst volume, being this is an indication of a mass-transfer limitation (MTL) effect.

This chapter focus on discussing these diffusion impacts on FAU using hydrocarbon catalytic cracking product selectivity and catalytic rates. By exposing the parent ammonium form of a commercial zeolite Y sample with a Si/Al = 2.5 to steaming

and acid leaching conditions, a resulting generation of mesoporous channels occurs. Complementary to the creation of mesoporosity is the impact on Si/Al ratio, consequently affecting the concentration of acid sites (BAS) [211, 212]. The resulting catalyst presents a clear presence of large channels as shown in **Figure 66**. Through a differential hysteresis scanning of Ar sorption to observe bulk porosities properties in the treated zeolites, an increase in mesoporous volume from 0.09 to 0.23 cm^3/g_{cat} is observed and continued as the severity of treatment increased [213]. This higher extent of mesoporosity is understood to reduce the diffusion pathway of reacting molecules and thus decrease the possibility of a re-adsorption and further reaction.

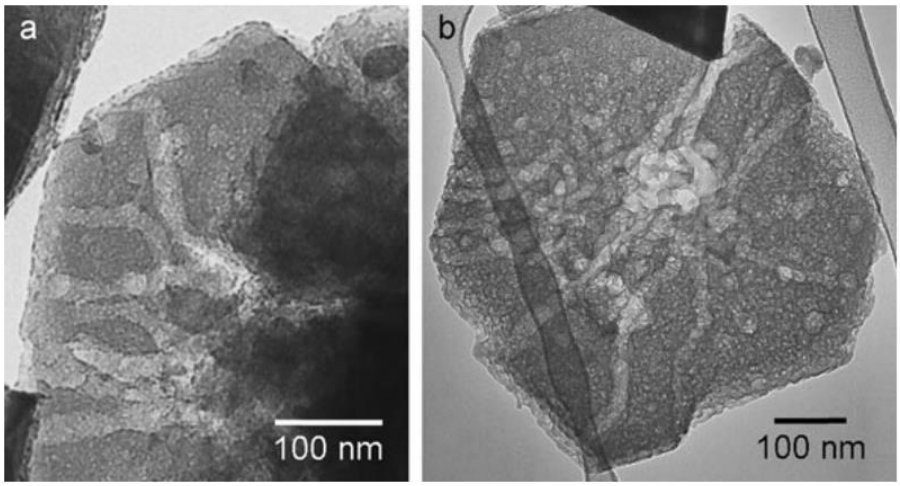

Figure 66: Conventional TEM images of severely steamed and subsequently acid-leached zeolite Y crystals with Si/Al ratios 15 (a) and 30 (b), commercially available as CBV-720 and CBV-760, respectively, from Zeolyst. Reproduced from Ref [214].

The study will utilize the use of commercially available FAU samples CBV-300 (Si/Al = 2.5), CBV-720 (Si/Al = 15) and CBV-760 (Si/Al = 30), in which the parent form goes through steaming procedures for the creation of mesoporous channels as observed in **Figure 66**. The gas-phase flow cracking reaction of 2,2,4-trimethylpentane is used as model reaction as well to interpret diffusion impacts that might exist among the samples. The presence of MTL can impose a significant effect on isooctane diffusion and its

reactivity in zeolite Y. Although it can be hypothesized that mesoporous samples may not have MTL, its presence on zeolite Y2.6 is not known. Therefore, investigating MTL is necessary to better comprehend the cracking results over zeolite Y. Na-titration was performed on three commercial Y samples with varying Na-loading according to each parent BAS and determining the concentration of acid active sites in each series through IPA-TPD. The catalytic activities were compared, and modeling was performed when possible, considering a Uniform type of titration, which assumes a homogeneous distribution of the titrant species along the catalyst particle. This concept has been demonstrated in previous studies with the self-aldol condensation of acetone and cyclopentanone in zeolite Y30. An expectation is relative to the product selectivity shift from the mesoporosity introduction and the concomitant effect on BAS density.

4.2 Experimental Methods

4.2.1 Chemicals and Materials

The chemicals were purchased from Sigma Aldrich and used as provided: 2,2,4-trimethylpentane (HPLC grade, >99%, isooctane), heptane (ReagentPlus 99%), ammonium nitrate (NH_4NO_3), calcium nitrate tetrahydrate ($Ca(NO_3)_2.4H_2O$), cobalt (II) nitrate hexahydrate (reagent grade, $Co(NO_3)_2$), silica gel (high-purity grade, 90A, 70-230 Mesh), sodium aluminate (NaAlO), sodium hydroxide (NaOH), sodium nitrate ($NaNO_3$), tetrabutylammonium hydroxide solution (40wt. % in H_2O, TBAOH). The commercial Y zeolites used were obtained from Zeolyst International in their NH_4^+-form: CBV 300 (Si/Al = 2.5), CBV 720 (Si/Al=15) and CBV 760 (Si/Al=30). The Y2.5, Y15 and Y30 are the notations relative to the Y zeolite and their respective Si/Al.

4.2.2 Site Density Counting

Quantification of active site concentration was performed using the isopropyl-amine temperature programed decomposition (IPA-TPD), the procedure was detailed in previous chapters.

4.2.3 Gas-Phase Catalytic Reactions

Gas phase flow reactions were conducted in a quartz tube reactor (1/4" OD). The catalyst was first pelletized (350-400 μm), packed between quartz wool in the quartz reactor, and placed inside a controlled-temperature oven. A thermocouple was placed aside the quartz reactor and beneath the catalyst bed. The reactant feeding occurred through a heated stream (170 ^oC) connected to a 6-port manual switching valve, connecting the inlet stream with the reactant, the quartz reactor, and the outlet stream directed to either the ventilation line or the Hewlett Packard 6890 gas-chromatography equipped with a flame-

ion-detector analyzer and a HP-AL/S column with dimensions of 50m x 0.32 mm x 8 μm. Prior to the catalytic reactions the catalyst was pre-treated in-situ at 300 ^{o}C for 2 hours with a ramping rate of 5 ^{o}C/min under nitrogen environment (100 mL/min). After the reaction temperature was reached, the reactant was injected to the reactor setup through a septum on a heated vaporization zone using KD Scientific syringe pumps, and then time zero was set. An initial ten minute constant feeding was performed, followed by sample collections at different reaction times on stream or pulses, depending on the mode in which the reaction was analyzed (flow or pulse mode). To prevent the condensation of reaction products on the downstream tubing, the outlet of the reactor was heated to 170 °C. Conversions were calculated on an area basis, as well as products selectivity. No reactant or product calibration were necessary because the reacting hydrocarbon molecules are broken down into individual carbon atoms and hydrogen atoms by the high-temperature flame in the detector. The number of ions produced in the detector is directly proportional to the number of carbon atoms in the hydrocarbon molecule. Therefore, by measuring the number of ions produced, the concentration of the hydrocarbon can be determined based on relative peak area. By using a stoichiometry correlation for each carbon atom, the FID can accurately determine the concentration of the hydrocarbon in the sample.

4.3 Results and Discussions

4.3.1 Isooctane Cracking Mechanism over Acid Sites in Zeolites

The catalytic cracking of isooctane, also denoted here as iC_8, over acid sites have two possible mechanistic routes resulting in methane (C_1), propylene ($C_{3=}$), butane (C_4) and butene ($C_{4=}$) as major products, and their respective isomers [215, 216]. The C_4 products that are formed tend to have a specific spatial arrangement, with one tertiary carbon connected to three primary carbons, this arrangement is more stable and is therefore found in relatively large amounts[217]. This structure has the highest stability among the isomers due to the presence of tertiary carbon. Other products as C_2s, C_5s, C_6s, C_7s, and C_8+ have negligible selectivity compared to other products.

The first reaction route discussed is shown in **Scheme 2,** characterized for an initial carbon protonation at the quaternary carbon, also acknowledged as 2nd C in the hydrocarbon chain. Arguments relative to whether this protonation occurs at the tertiary and quaternary carbon can be proved through the catalytic cracking of isobutane (iC_4) and 2,5-dimethylhexane over zeolites Y, once these molecules replicate the tertiary structure found in iC_8. Keeping track on the products distribution in **Figure 67.a)** it can be observed in the cracking of 2,5-dimethylhexane negligible amounts of C_1s, instead it is detected a major presence of C_3s, C_4s and C_5s paraffins and olefins. This result confirms that as the tertiary carbon receives the H from the acid site, protolytic cracking dominantly occurs either between the α- (protonated carbon) and β-Carbon (neighboring carbon) forming C_3s and C_5s, or between the β-Carbon and its adjacent C forming C_4s (**Figure 67.b)**). Thus, extinguishing the possibility of C-C cleavage with the primary C forming C_1. Isobutane differently does not crack significantly on zeolites Y at the present reaction conditions

according to **Table 12** results, rather dehydrogenation is more likely to happen. Indeed its cracking activity is compared to neopentane's over zeolite Y in literature [218]. While cracking was dominant over neopentane forming C_1 and $iC_{4=}$, in iC_4 it was found a large rate towards dehydrogenation and formation of other species rather than C_1s and C_3s. These results support the protonation over the quaternary carbon forming a penta-coordinated carbocation (also known as carbonium ion) instead of protonation the tertiary carbon in the iC_8 structure.

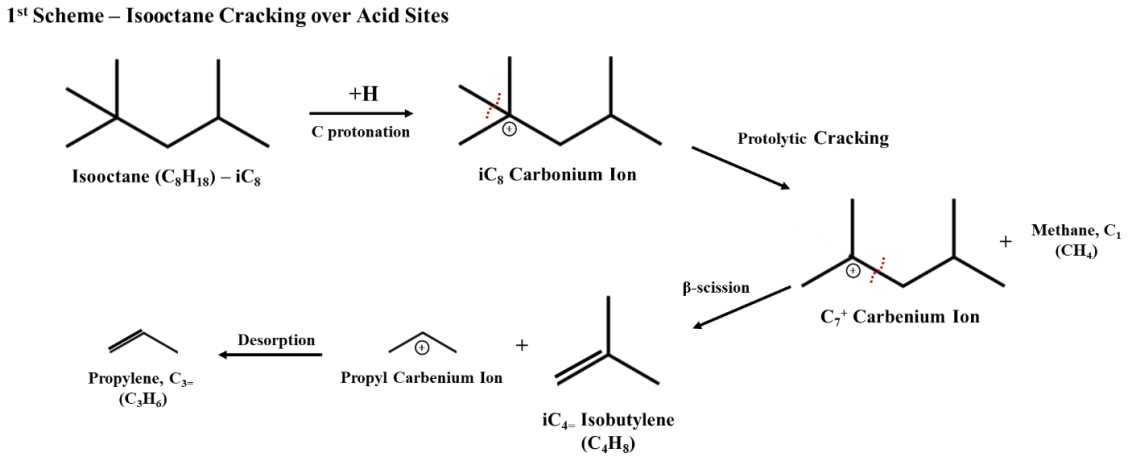

Scheme 2: Isooctane cracking over acid sites through quaternary carbon protonation and carbonium ion protolytic cracking.

Table 12: Molar product selectivity distribution on isobutane cracking over zeolite Y with varying Si/Al.

	Product Selectivity		
	Y2.6	Y15	Y30
C_1	26%	14%	19%
$C_{3=}$	20%	14%	19%
$C_{4=}$	43%	64%	58%
C_5	10%	8%	5%
Conversion	0.033%	0.040%	0.020%
$\frac{Dehydrogenation\ Products\ [mols]}{Protolytic\ Cracking\ Products\ [mols]}$	1.9	4.6	3.0

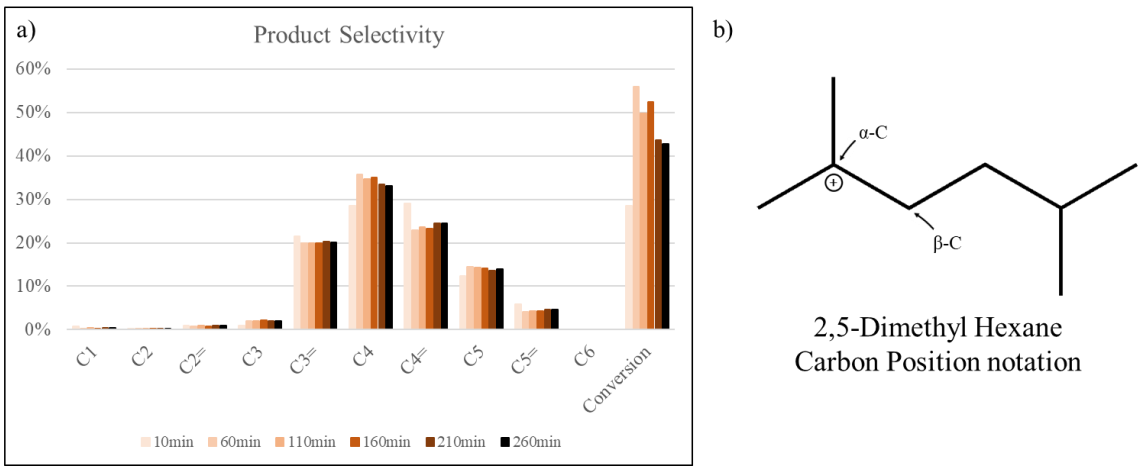

Figure 67: a) Product distribution of 2,5-dimethylhexane catalytic cracking over zeolite Y15 in flow mode. Bar representation is relative to product distribution within progressing reactant time on stream. Reaction conditions: 400 ºC, 50 mg of catalyts, 0.5 mL/hr of reactant injected, 100 mL/min of N_2 inert flow. Pretreatment under N_2 at 300 ºC for 2 hours prior injection. **b)** 2,5-dimethyl hexane carbon positioning notation.

The following protolytic cracking of that carbonium iC_{8+} forms C_1 and a C_7^+ carbenium ion species adsorbed on the catalyst surface. The next step is a C-C β-scission with a resulting $C_{3=}$ and an adsorbed C_4^+ specie as products, which this C_4^+can further receive a proton from a H-donor forming an alkane or desorb as a $C_{4=}$. This structure is reported to be an isobutoxide specie with a covalent bond with the oxygen on the surface, a more stable surface molecule compared to its isomers [219]. Such mechanism requires a stoichiometry product distribution in where for each C_1 and $C_{3=}$ formed an equal amount of C_4 or $C_{4=}$ must be present. It is assumed here that once iC_8 is present over the reaction environment C_4 adsorption is not likely to occur because larger the number of Cs in the chain stronger it is its adsorption, thus any possibility of C_4 paraffin adsorption and sequential cracking forming C_1 and $C_{3=}$ is not considered. If C_1 and $C_{3=}$ is present it will be due to iC_8 prototylic cracking.

Differently than an initial iC_8 adsorption and protolytic cracking, the second mechanism (shown in **Scheme 3**) considers either a first H-transfer from that iC_8 to an

adsorbed H-receptor or protonation of a dehydrogenated iC_8. The last is less likely to happen due to lower dehydrogenation conversions found for iC_4 under reacting conditions, considering here that H-transfer of isooctane the dominant step. The resulting iC_8^+ carbenium ion undergo β-scission, forming a $C_{4=}$ and an adsorbed C_4^+. Depending on the environment around the active site, this isobutoxide can either desorb as a $C_{4=}$ or receive a H from a nearby iC_8 and desorbs as a C_4 alkane. Further protolytic cracking of the C_4 paraffin is disregarded due to the preferential iC_8 adsorption and competition inside the catalyst voids. Therefore, the only products coming out of this reaction pathway are C_4 paraffins and olefins only. Both routes are feasible over zeolite Y and conclusions whether one is more dominant will be discussed through the course of the study.

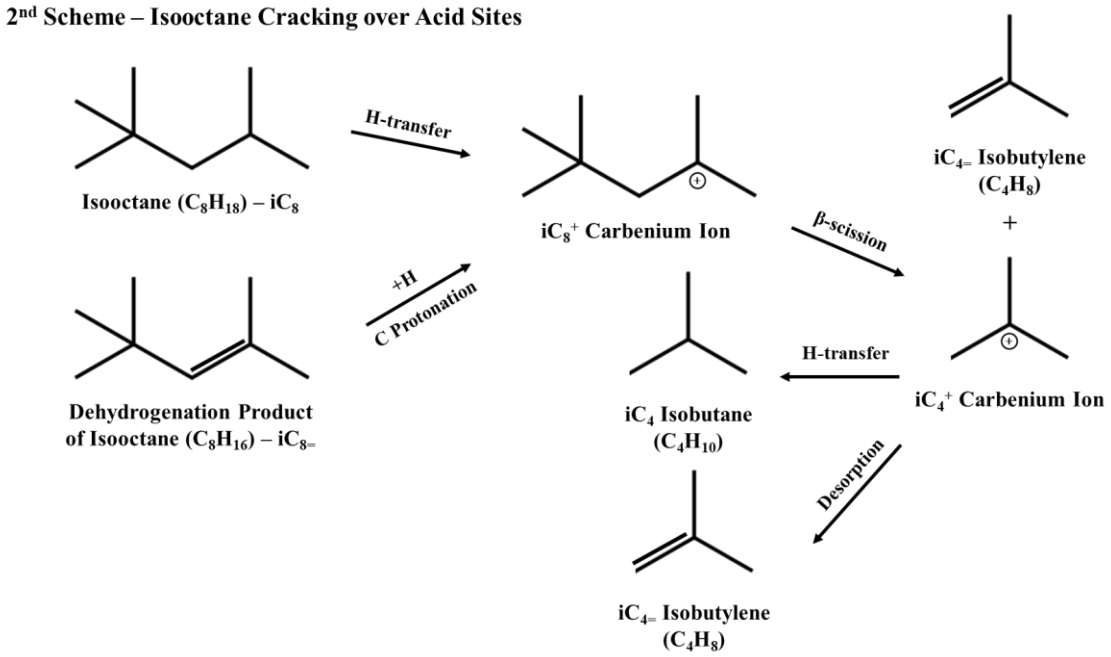

Scheme 3: Isooctane cracking over acid sites through H-transfer and carbenium ion β-scission.

4.3.2 Catalytic Cracking Differences Between Non-Steamed and Steamed Commercial Zeolite Y

The commercially available zeolite Y samples have three different Si/Al ratios and consequently different BAS densities. **Table 13** displays the concentration of active acid sites calculated by IPA-TDP. The results indicate that steaming the parent Y2.6 yields Y15 zeolite, which experiences an 84% drop in BAS, whereas Y30 experiences a 90% drop due to a more severe steaming process. A drawback of the zeolite steaming is the creation of EFAL species, which are likely to happen once such degree of Al extraction occurred in both zeolites. Reports on literature about ^{27}Al magic-angle spinning (MAS) nuclear magnetic resonance (NRM) results over the two steamed commercial samples confirming the presence of EFAL but in a lower percentage as compared to that structural incorporated Al and thus will not influence over the catalytic results [220, 221]. The NMR technique identifies the aluminum coordination in the catalyst volume, referring to a tetrahedral coordination relative to the structural aluminum incorporated in the catalyst framework, and a partial or octahedral coordination to that aluminum that is either partially or fully extracted but still is present in the framework.

Table 13: Concentration of Brønsted acid sites on the commercial zeolite Y samples with different Si/Al ratios from Zeolyst International.

	Theoretical BAS density (mmol/g_{cat})	IPD-TPD BAS density (mmol/g_{cat})
Y2.6	4.63	2.30
Y15	1.04	0.37
Y30	0.54	0.23

Gas-phase pulse reactions for the catalytic cracking of iC_8 demonstrate significant differences in conversion for three samples with the same amount of catalyst mass used (as

shown in **Figure 68**). The abrupt increase from 3.9% (Y2.6) to 64.3% (Y15) is attributed to the creation of mesoporous channels within the catalyst particle, enabling a substantial increase in iC_8 diffusion and reaction over active sites. This difference evidences the presence of mass-transfer limitations in Y2.6, indicated by an increase in cracking conversion as the concentration of active sites dropped in Y15. If the system was free of diffusion limitations, a proportional decrease would have been observed, however, other catalyst aspects seem to affect iC_8 reactions over the Y zeolite. The decrease observed from 64.3% in Y15 to 15.7% in Y30 is due to the reduction in BAS concentration once mesoporous channels are present in both zeolites. However, the conversion drop is not proportional related to the drop in BAS density, such is attributed to lower the concentrations of proximate sites as BAS decreases. These proximate sites are hypothesized to facilitate iC_8 consumption assisting in stabilizing high energy species during the course of the reaction. Such synergy between sites can enhance kinetic rates or even adsorption of one specie [222].

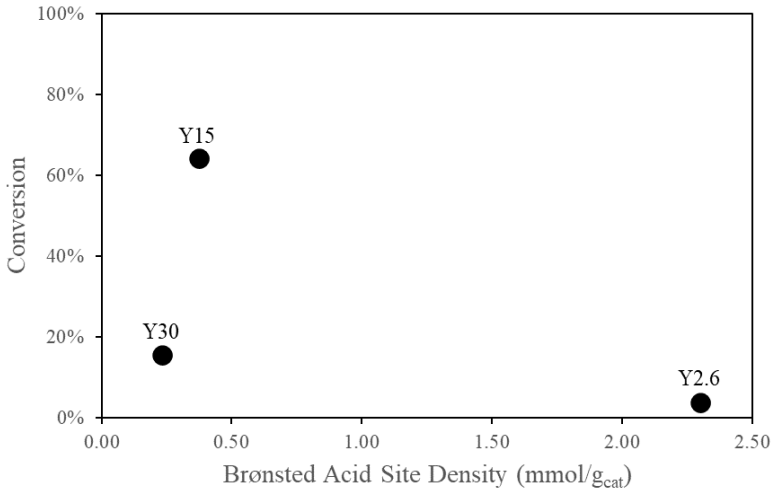

Figure 68: Isooctane cracking conversion comparison among the commercial zeolite Y samples. Reaction conditions: 400 ^oC, 50 mg of catalyst, 0.5 mL of reactant injected per hour, 100 mL/min of N_2 inert flow. Pretreatment under N_2 at 300 ^oC for 2 hours prior injection.

To better comprehend the functionality of these synergistic sites, the product distributions are analyzed for the three samples as a function of pulse number are shown in **Figure 69**. In regards of the equivalent mass runs, a higher selectivity for that $C_{4=}$ product is found in Y2.6 and decreases in both Y15 and Y30. C_4 formation seems to be favored as mesoporosity is introduced but decreases as the BAS density drops. An increase towards C_1 and $C_{3=}$ products occurs as BAS lowers, products of that iC_8 protolytic cracking route. As the conversion is adjusted for all the three catalysts through changing the catalyst mass, a clear change in Y15 product selectivity is observed getting proximate to the one found in Y30. In these two samples, limitations in regards of species diffusion is negligible due to the presence of mesoporous channels. The higher BAS found in Y15 seems to assist H-transfer through that higher probability of encountering proximate sites, while in Y30 such situation is less likely to happen, resulting in a decrease in that H-transfer characteristic. Also, the minor changes observed in C_1 and $C_{3=}$s distributions with conversion in the two mesoporous catalysts suggest that a mechanism preference here is not dependent on conversion, but rather on other factors.

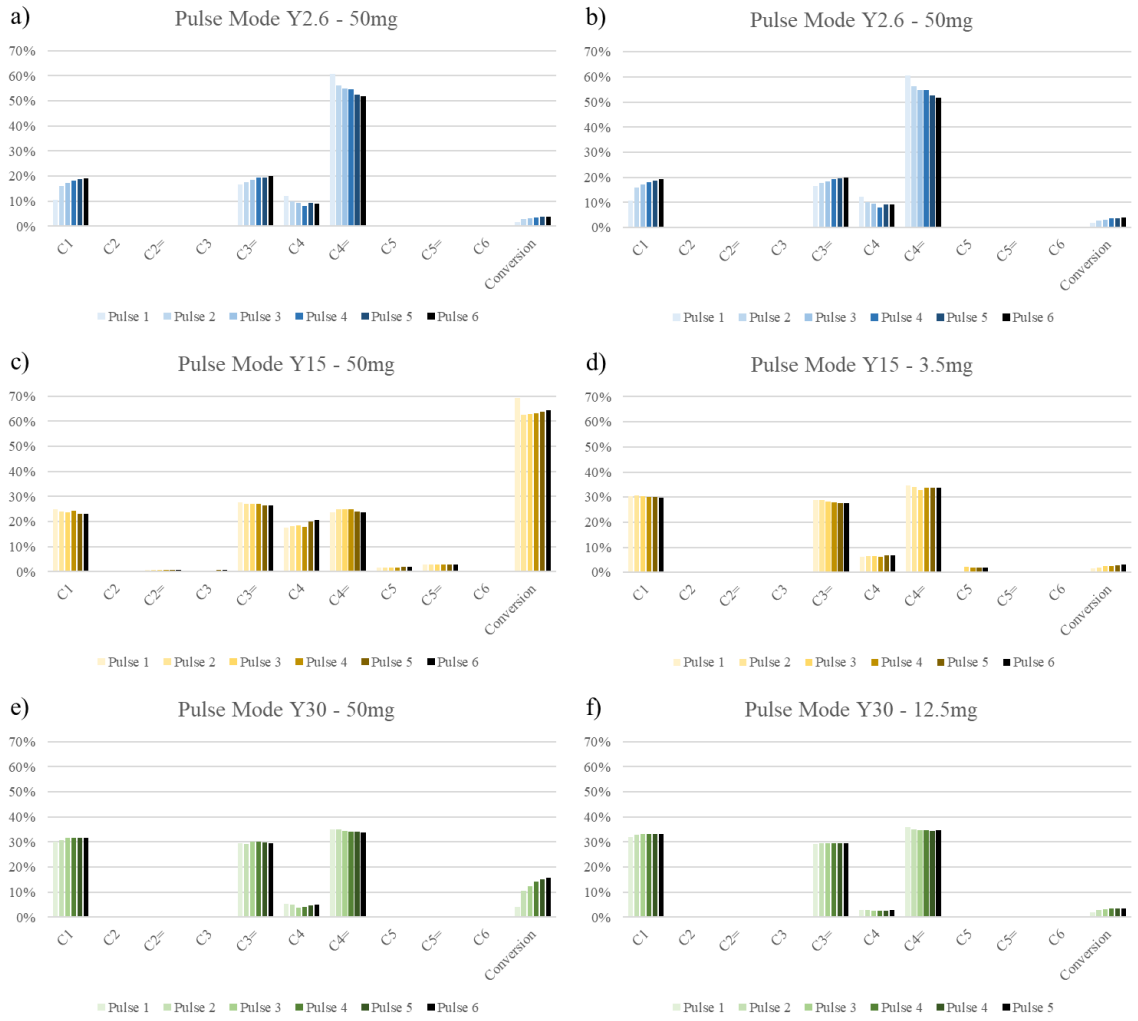

Figure 69: Product selectivity of isooctane cracking over zeolite Y2.6 (*a* and *b*), Y15 (*c* and *d*) and Y30 (*e* and *f*). Reaction conditions: 400 °C, 0.5 mL of reactant injected per hour, 100 mL/min of N_2 inert flow. Pretreatment under N_2 at 300 °C for 2 hours prior injection.

In the interest of observing these mechanistic preferences, methane (C_1) selectivity is proposed to be used as an analysis parameter as follows:

$$C_1 Selectivity = \frac{n^o\ mols\ C_1\ formed}{total\ n^o\ mols\ products\ formed} = \frac{C_1}{C_1 + C_{3=} + C_4 + C_{4=}}$$

In where C_1, $C_{3=}$, $C_{4=}$ and C_4 is relative to each mol formed in a given reaction. Since C_1, $C_{3=}$ and $C_{4=}$ are the direct products of protolytic cracking, considering a case in which iC_8 fully undergoes through this reaction path, no H-transfer occurs, and the maximum molar selectivity attributed to C_1 is 33%. As this value lowers, then, it is

understood that the other reaction pathway going through an iC_8 H-transfer and iC_8^+ carbenium ion formation is preferred.

Figure 70 shows C_1 distribution for the three commercial Y samples as a function of conversion for pulse mode gas-phase reactions. In all catalysts the values found for C_1 selectivity were close to the maximum allowed for that C_1 molar distribution (~33%), meaning that in the range studied the cracking through an iC_8^+ carbonium ion route is favored. Y2.6 presented the lowest selectivity towards an iC_8^+ carbonium ion route. This catalyst has the highest BAS density among the studied faujasite zeolites, as a result, a probability of proximate sites is large and thus suggesting a higher H-transfer rate.

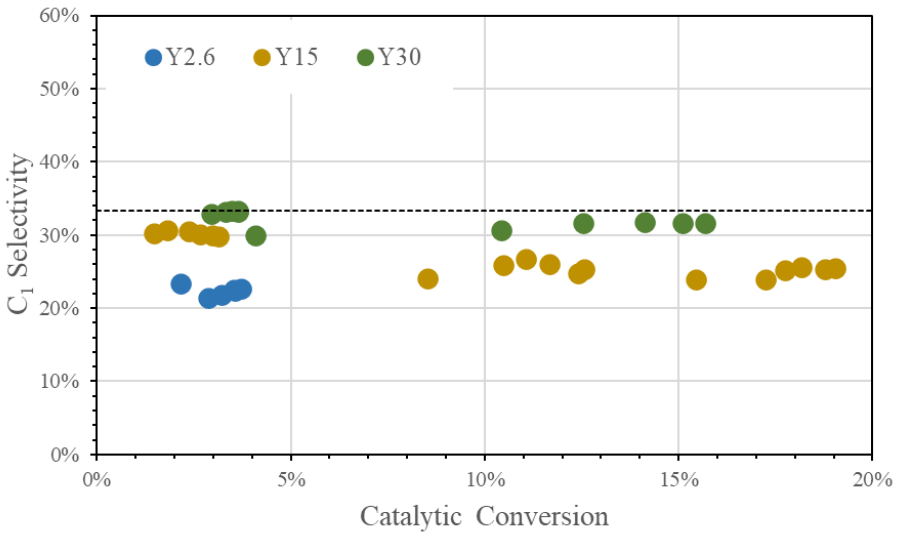

Figure 70: C_1 selectivity as a function of isooctane conversion over zeolite Y2.6, Y15, and Y30 in pulse mode. Reaction conditions: 400 ºC, 0.5 mL of reactant injected per hour, 100 mL/min of N_2 inert flow. Pretreatment under N_2 at 300 ºC for 2 hours prior injection.

At low conversions the two mesoporous zeolites Y15 and Y30 performs somehow identically, but as conversion increases Y15 shifts towards lowering C_1 selectivity. The higher BAS density in Y15 facilitates $C_{4=}$ re-adsorption and formation of a C_4^+ carbenium ion, in which at higher local concentrations of iC_8 increases the H-transfer rates, and as

conversion progresses this difference is enlarged. Again, the presumption of a higher concentration of pair-sites enhances the chances of H-transfer from an iC_8 to nearby H-receptor specie (C_4^+).

Gas-phase reactions in pulse mode are characterized for lower concentrations of H-donor species in the catalyst volume due to intermittent injection of the reactant gases to the reactor bed, whereas in flow mode a constant and continuous feeding of iC_8 occurs and happens to increase these H-donor species around the site, theoretically favoring the probability of H-transfer. Once C_4 paraffin is a direct product of the discussed iC_8^+ carbenium ion route through proton transfer, by tracking its amount obtained in a specific case, one is able to discern the reaction pathway preferences. For this, a $C_4/C_{4=}$ ratio was investigated. This ratio ranges from 0 to 1, with 0 indicating that no H-transfer is occurring and iC_8 is solely undergoing protolytic cracking, and 1 indicating that for every C_4 paraffin produced, an equivalent C_4 olefin is also produced, matching the product stoichiometry of this reaction pathway. It is assumed that there is no re-adsorption of the $C_{4=}$ olefin, which could lead to a higher concentration of the C_4^+ species necessary for the H-transfer mechanism. This intermediate is believed to exist solely due to subsequent iC_8^+ C-C cleavage. The results for the $C_4/C_{4=}$ ratio can be found in **Figure 71** for all the three catalysts at low conversion runs.

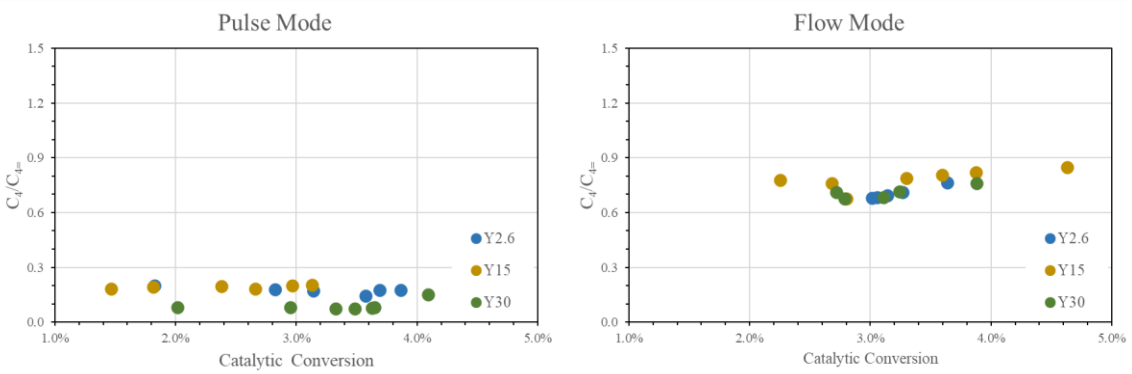

Figure 71: H-transfer ratio at low isooctane conversions over zeolite Y2.6, Y15, and Y30. Reaction conditions: 400 ^{o}C, 0.5 mL of reactant injected per hour, 100 mL/min of N_2 inert flow. Pretreatment under N_2 at 300 ^{o}C for 2 hours prior injection.

Through the results it is evident an increase in H-transfer as flow mode is used. The previous assumption in regards of a higher local presence of a H-donor molecule in flow modes is valid and it seems that in this reaction mode all the three catalysts similarly behave. A possible explanation goes for the higher coverage of iC_8 in flow modes causing the acid sites to perform individually besides the proximity or either that not necessarily this transfer is occurring with an adsorbed iC_8, but actually from a nearby molecule in the bulk phase instead.

4.3.3 Na-Titration over Commercial Zeolite Y

The presence of MTL is investigated for the three studied zeolites Y. For each catalyst four Na-samples were prepared and the results are discussed below.

Y (Si/Al 2.6) zeolite: **Figure 72** compares experimental gas-phase pulse mode cracking reactions of isooctane on Y2.6 with varying Na-loadings, at a reaction temperature of 400 ^{o}C and feeding rate of 0.5 mL/hr of pure reactant under a N_2 gas stream of 100 mL/min. Such reaction conditions are maintained throughout the whole Na-titration experiments.

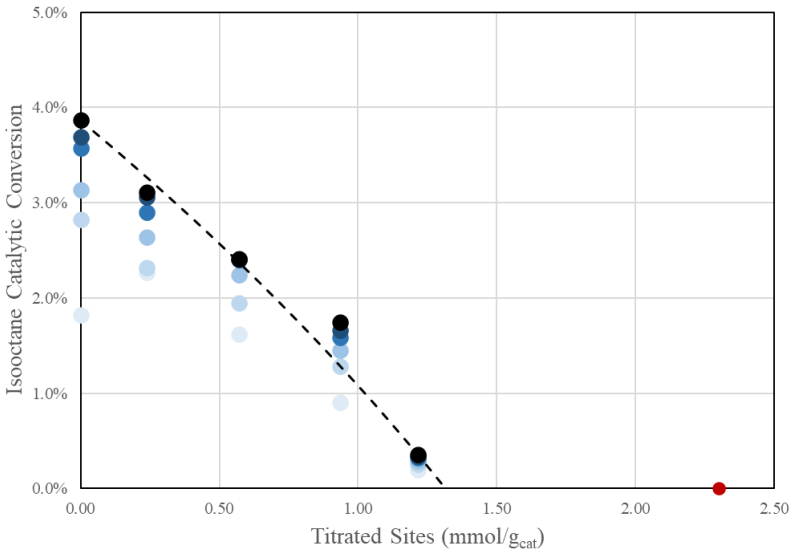

Figure 72: Pulse mode catalytic conversion of isooctane as a function of titrated site density in series of Na-exchange Y zeolite with Si/Al of 2.6. The marker color darkens from blue to lack as the number of pulses increases. The red marker over x-axis is relative to the calculated BAS density of the non-exchanged parent Y2.6. For Y2.6 a fixed 50 mg of catalyst is used.

The dotted line is respective to the modeled conversion drop as a function of titrated sites for the 6th pulse in where it is understood that the conversion had stabilized. It is notable the BAS deviation as activity approaches zero, in which the modeling finds a value of 1.32 as compared to 2.30 mmol/g$_{cat}$ in the IPA-TPD. A Thiele modulus 1.99 is found with a corresponding effectiveness factor of 0.81. These values point to conclude a small effect of mass-transfer limitations and the lower site accessibility of iC_8 as compared to isopropyl-amine, used for site counting.

For comparison purposes in zeolite Y2.6, the catalytic cracking of heptane over the Na-titrated Y2.6 series was performed and discussed. The reactions were at higher temperature of 525 ^{o}C with equivalent operational conditions and the cracking conversion plotted in **Figure 73**. Coking formation was notorious and conversion dropped as the number of pulses increased. Relative to the catalyst

activity, an identical drop to that in isooctane is observed, with a null activity at a titrated BAS of 1.29 mmol/g_{cat} and Thiele modulus close to a region free of mass-transfer ($\phi \sim 1$). The activity drop occasioned by Na was not a feature specific only to isooctane and infer that heptane might also not be able to access those hidden sites as assumed. Still, it is interesting that even a smaller and linear molecule as heptane presented MTL to a smaller extent as compared to isooctane even at higher temperatures, supporting a possible idea of a lower extent of MTL in these two molecules.

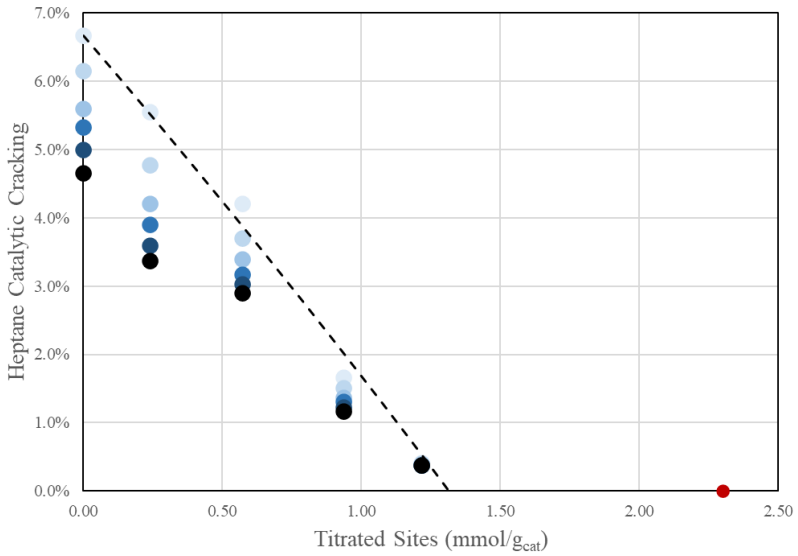

Figure 73: Pulse mode catalytic conversion of heptane as a function of titrated site density in series of Na-exchange Y zeolite with Si/Al of 2.6. The marker color darkens from blue to black as the number of pulses increases. The red marker over x-axis is relative to the calculated BAS density of the non-exchanged parent Y2.6. For Y2.6 a fixed 50 mg of catalyst is used.

Y (Si/Al 15) zeolite: In a similar way, **Figure 74** shows the cracking conversions over Y15 at different Na-loadings. A particular behavior is observed in where a sharp drop takes place between the non-exchanged Y15 and the lowest Na-exchanged sample, followed by a more moderate conversion drop as Na-titration levels increase. Again, the catalytic rate zeros at very lower values of BAS density

than those found in IPA-TPD (0.28 vs. 0.37 mmol/g_{cat}), accordingly to the linear fitting of the four Na-titrated samples (R^2 = 0.980). It appears that some highly active sites exist and are preferentially titrated by Na, here it is inferred that those sites are either in close proximity or are positioned in a more synergistic environment that favors the isooctane catalytic cracking. The first possibility is considerably more realistic once previous studies showed their influence over *n*-hexane cracking [163].

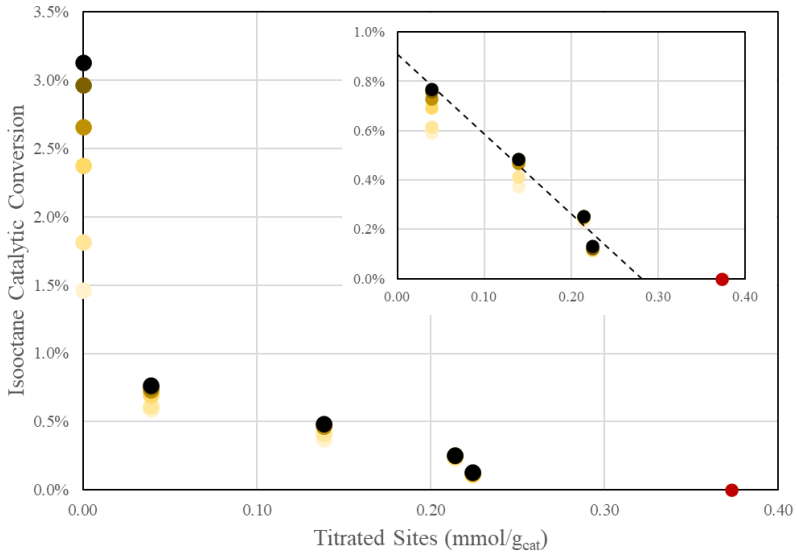

Figure 74: Pulse mode catalytic conversion of isooctane as a function of titrated site density in series of Na-exchange Y zeolite with Si/Al of 15. The marker blue colors turns darker as the number of pulses increases. The red marker over x-axis is relative to the calculated BAS density of the non-exchanged parent 15. For Y15 a fixed 3.5 mg of catalyst is used.

Y (Si/Al 30) zeolite: In Y30 the conversion drop was not pronounced as those found in Y15, rather as the exchange levels increased lower variations occurred (**Figure 75**). The modeling was not feasible in this case due to the shape of the curve even considering a linear regression. If it was hypothesized the existence of highly active sites in the Y15, those would also be present in Y30 but in lower concentrations and thus less contributive to the overall activity.

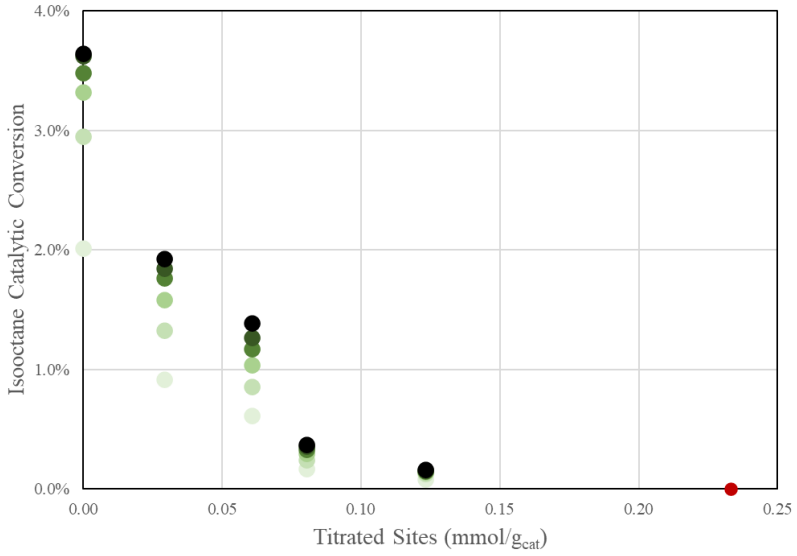

Figure 75: Pulse mode catalytic conversion of isooctane as a function of titrated site density in series of Na-exchange Y zeolite with Si/Al of 30. The marker blue colors turns darker as the number of pulses increases. The red marker over x-axis is relative to the calculated BAS density of the non-exchanged parent 30. For Y30 a fixed 12.5 mg of catalyst is used.

In Y2.6, the non-linear rate drop resembled that expected for the Uniform type of titration in which the results confirmed a certain degree of MTL, being possibly due to the constrained environment of the zeolite itself or the high activity per second in a single site. However, to match the catalytic activity levels of those found in Y15 a more pronounced MTL should had been observed with a respective effectiveness factor of around 0.06 and not 0.81 according to the calculated values. An explanation for this higher activity in zeolite Y15 is the appearance of synergistic sites through steaming and exposing them to reaction conditions that lead to such conversion extents.

A consequence of introducing mesoporosity is the removal of existing MTL in the parent zeolite. With that, the fastest diffusion of isooctane allows a concentration increase in the reaction environment and exposes each detailed particularities of that zeolite. As Na is used to deactivate a portion of active sites a noticeable drop is observed in both Y15 and

Y30. It seems that this metal cation selectively titrate those synergistic sites or either cancelling out the synergism existence between two proximate sites, but as the exchange level progress equivalent drop in conversion occurs. By plotting the relative conversion drop as a function of percentage of titrated sites this behavior is observed as shown in **Figure 76**. An understandable explanation is the higher concentration and contribution in catalytic activity of these sites in zeolite Y15 compared to Y30, stating that as steaming is extended a lower density of highly active sites is resulted. It is still not fully understood the reason for the null reaction rate as titration levels approaches 60% of those total sites calculated by IPA-TPD and requires future studies.

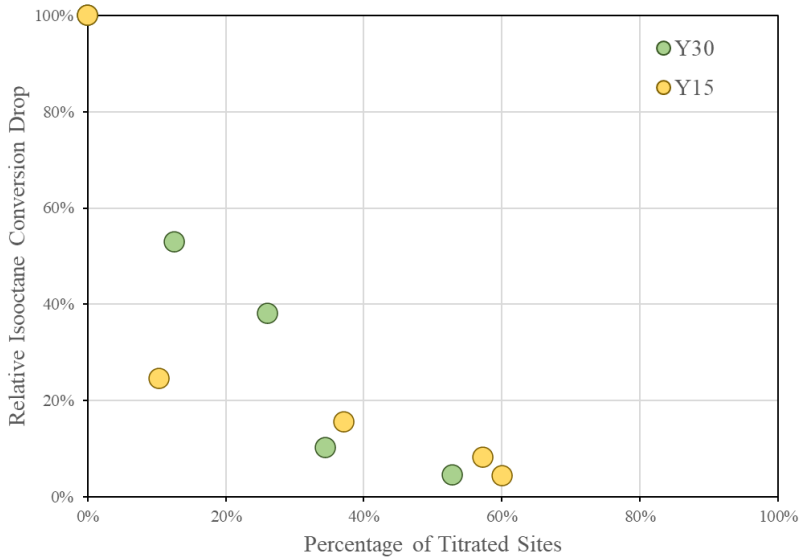

Figure 76: Relative isooctane conversion activity as a function of percentage of titrates sites in zeolite Y15 and Y30 in pulse mode reactions.

This comparison is also studied in flow mode reactions using the same set of Na-series for both Y15 and Y30 (**Figure 77**). Curiously the contrast is less pronounced than that in pulse mode, and the systems behave analogously as it has been noted for $C_4/C_{4=}$ ratios comparisons. These differences in activity caused by the hypothesized concentration of pair-sites seem acceptable until this point, once in pulse mode reactions activity is

promoted due to the lower site coverage and is less distinct in flow modes as site coverage increases.

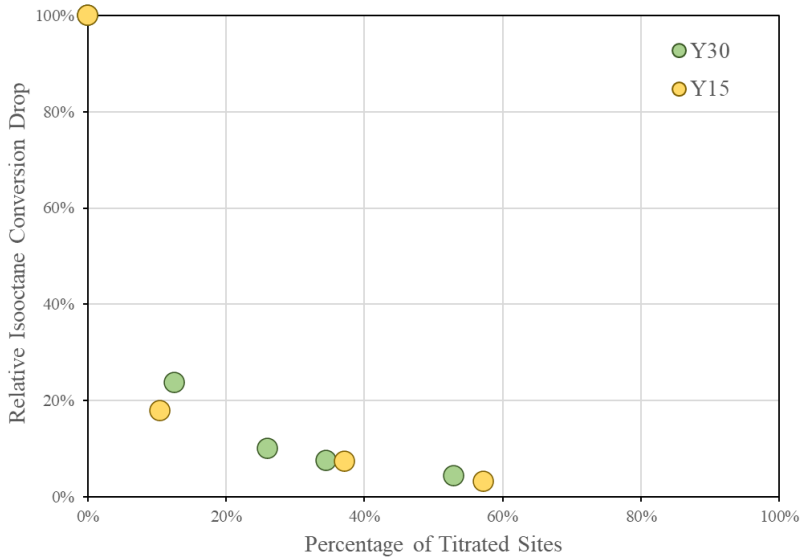

Figure 77: Relative isooctane conversion activity as a function of percentage of titrates sites in zeolite Y15 and Y30 in flow mode reactions.

In order to investigate accurately these synergistic sites and the possible proximity influence over activity, the steamed and acid leached zeolite Y15 is chosen as the studied catalyst due to the less or none effect of MTL, the moderate site concentration, and also the larger contribution on catalytic activity some sites have.

4.3.4 Pair-Acid Site Study over Y15: A Product Selectivity Analysis

In early results it was observed existing differences between the two commercial steamed zeolites in regards of C_4 selectivity, by using the H-transfer ratio ($C_4/C_{4=}$) as a mean to compare in which proportion the adsorbed isobutoxide receives a H from a donor specie. Besides zeolite properties, the mode in which the gas phase reactions are run does also interfere in the results and their interpretation. Pulse mode is characterized to expose the reactant to the catalyst bed for short and intermittent period of times whereas flow mode

provides a continuous contact between the reacting specie and reaction environment. Reaction wise in isooctane cracking one can visualize a low surface coverage and low reactant concentrations around the active site in pulse mode, while a high coverage and concentrations enough to provide a higher H-transfer rate for those absorbed H-donor species. In Y15 this behavior is evident when H-transfer ratio is plotted with increasing conversion in both modes (**Figure 78.a)**). It is obvious that at higher conversions of isooctane from both mechanisms would generate higher concentrations of adsorbed C_4^+s and a following increase in that iC_8^+ carbenium ion formation rate, as a result of its dependence on H-receptors concentration to initiate this reaction pathway. A consequent drop in C_1 selectivity is followed (**Figure 78.b)**).

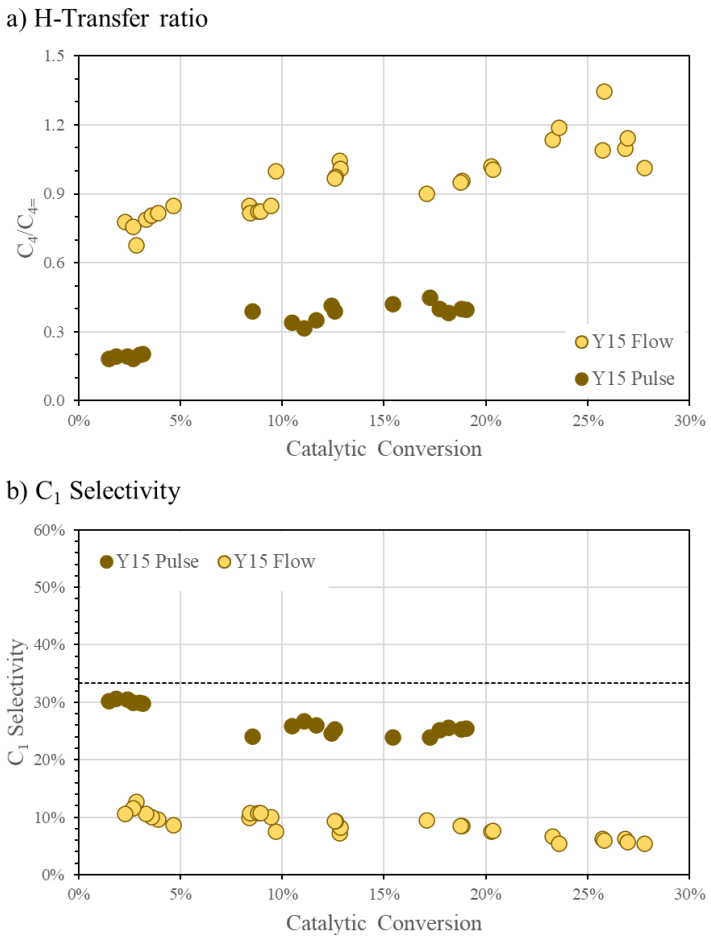

Figure 78: a) H-transfer ratio ($C_4/C_{4=}$) and **b)** C_1 selectivity as a function isooctane conversion in zeolite Y15. A comparison between reaction modes.

The observed abrupt drop in activity at low Na-loadings can also be examined with two other bivalent metal cations such as calcium (Ca) and cobalt (Co). The difference stands in their capability of titrating pair-sites instead for their 2^+ positive charge. By exchanging similar loadings to that used in the low Na-exchanged catalyst (0.01 mol of alkaline salt per liter of solution) a resulting BAS density of 0.29 and 0.33 mmol of H^+ per gram of catalyst respective to Ca and Co is found, in close exchange degree compared to 0.33 mmol/g_{cat} in Na. If this pair-site titration functionality is true for both metals, a loss in activity in similar degrees of Na is expected as well as a contrast in H-transfer ratio to that parent zeolite.

The gas phase isooctane cracking reactions over zeolite Y15 and exchanged samples presented differences in conversions as shown in **Figure 79**. Conversion per mmol of acid sites basis is capable of demonstrating a higher site activity comparison among samples, and as for those exchanged zeolites a similar conversion degree is occured.

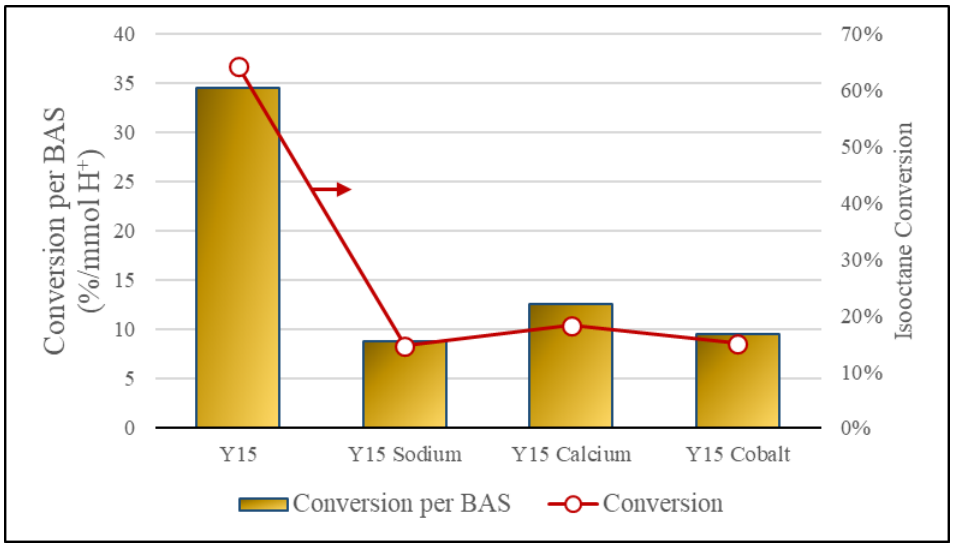

Figure 79: Conversion difference between initial Y15 and metal-exchanged zeolites, both as per Brønsted acid site basis gram of catalysis basis.

As the $C_4/C_{4=}$ ratio is analyzed an improvement is noticed as sites were titrated mainly for that Ca-exchanged sample in pulse mode reactions (**Figure 80.a)**). The Na-Y15 had similar C_4 formation as the parent Y15 at low conversions but as conversion increases contrast becomes more evident. No distinguishable differences among samples were noticed in flow mode, but with an apparent improvement in H-transfer rate as discussed before (**Figure 80.b)**). The premise of calcium titrating effectively the pair-sites is confirmed and affects C_4 and $C_{4=}$ distribution in comparison to sodium, indeed a greater effect is seen. Cobalt trends slightly deviate upward from Y15 in which a close proximity to calcium as predicted, however this disparity in product distribution shows to favor $C_{4=}$ formation confirming cobalt ability to serve as a dehydrogenation catalyst.

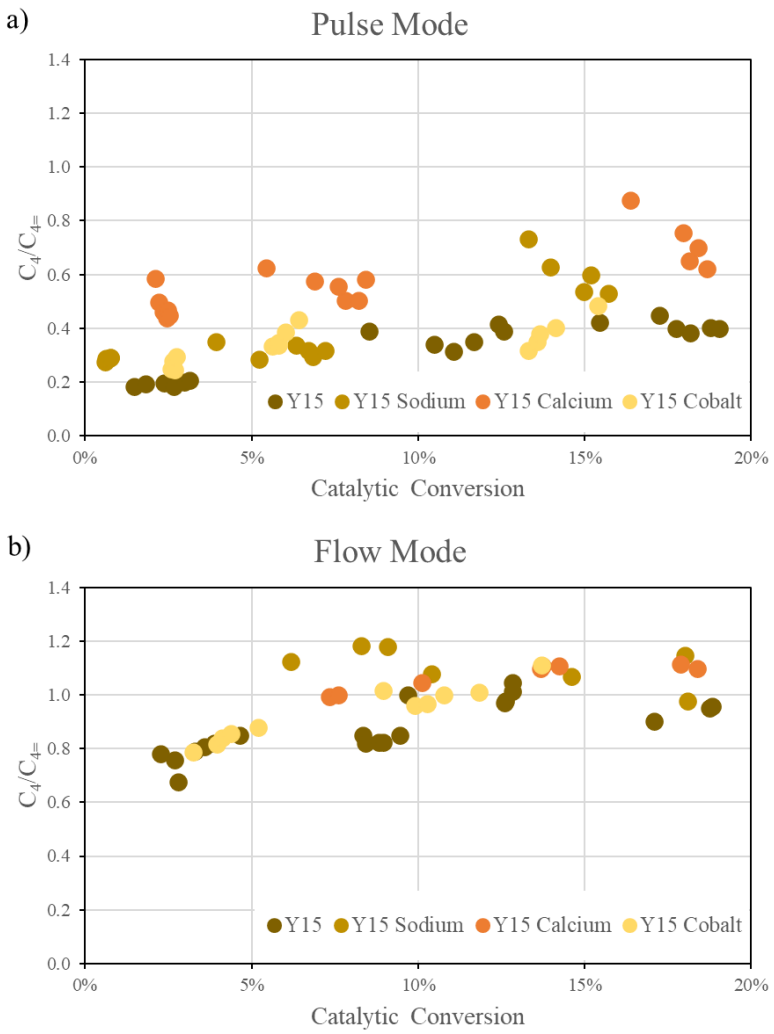

Figure 80: H-transfer ratio ($C_4/C_{4=}$) as a function isooctane conversion in zeolite Y15 and Na, Ca and Co-exchanged samples in a) pulse and b) flow reaction mode.

If C_1 selectivity is analyzed for these runs it is clear an inverse correlation with H-transfer rate (**Figure 81**). These results suggest a site distribution along the mesoporous faujasite samples favoring the protolytic cracking of iC_8 alternative to H-transfer and iC_8^+ carbenium ion formation. These sites are preferentially titrated by the metal cations and in general manage to participate in the reaction mechanism in synergism with a nearby site. Such is inferred due to the more pronounced drop in C_1 selectivity for that Ca-Y15 which has close site exchange extent to Na-Y15. As conversion increases, C_4^+ carbenium ion is

abundant and a resulting higher probability of H-transfer takes place explaining the proximity of C_1 selectivity and $C_4/C_{4=}$ ratios between Ca- and Na-samples.

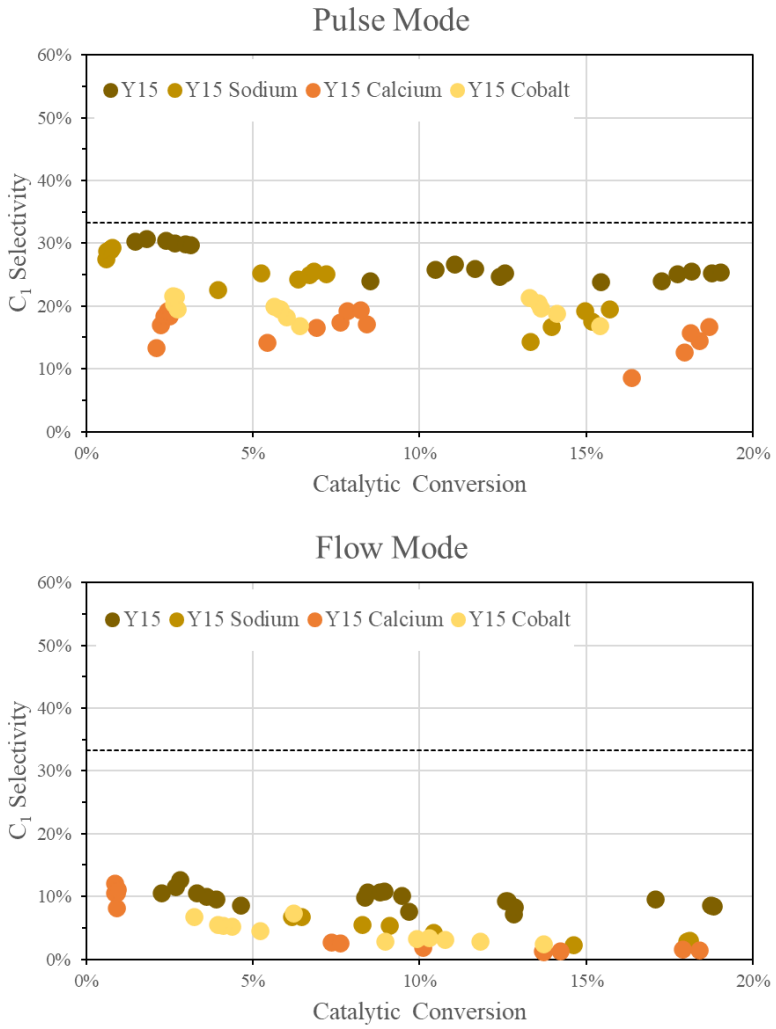

Figure 81: C_1 selectivity as a function isooctane conversion in zeolite Y15, Na, Ca and Co-exchanged samples in pulse and flow reaction mode.

Yet, computing $C_4/C_{4=}$ versus C_1 selectivity (**Figure 82**) it is remarked the overlap between Y15, Y15Na and Y15Ca, showing that the actual differences exist due to suppressing iC_8 protolytic cracking through titrating those so called synergistic sites. At very low C_1 levels, i.e. close to zero protolytic cracking rates, the $C_4/C_{4=}$ ratio goes to values higher than 1 meaning that a higher formation rate exists for that C_4 paraffin compared to C_4 olefin. The trends point to conclude that a re-adsorption of $iC_{4=}$ occurs and

are likely to happen at those synergistic sites, because as those are titrated, within the same level of C_1 selectivity, a higher C_4 formation is found, whereas in those exchanged samples to reach similar $C_4/C_{4=}$ ratios a lower rate of protolytic cracking must occur.

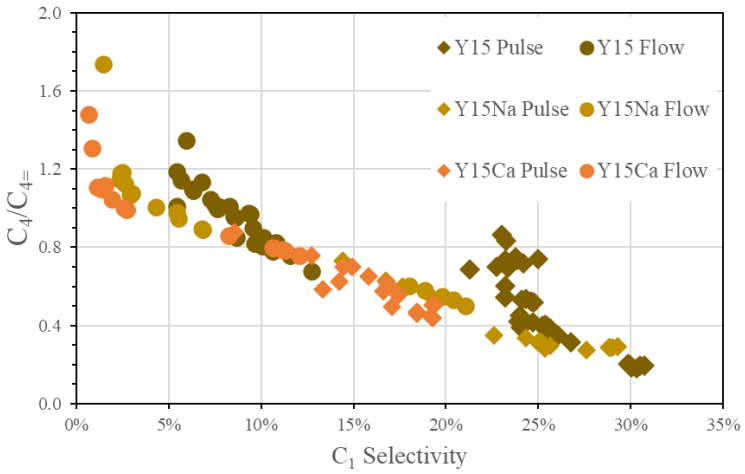

Figure 82: The inverse correlation between H-transfer ratio ($C_4/C_{4=}$) and C_1 selectivity over zeolite Y15, Na and Ca-exchanged samples in both reaction modes.

4.4 Conclusion

The introduction of mesoporosity in zeolites theoretically mitigates possible mass-transfer limitations existed in the non-modified parent catalyst, fastening reactant diffusion, and exposing active sites to optimum reaction conditions. Through steaming over the parent form of commercial faujasite a consistent drop in concentration of BAS is followed and it progresses as the thermal severity increases. Even with such drop in BAS density, the catalytic cracking conversion of isooctane boosted from 3.9% in Y2.6 to 64.3% in Y15, being 16-times higher per gram of catalysis basis and 100-times per mmol of acid site. Under severe steaming a resulting Y30 zeolite showed a conversion of 15.7%, a 75% reduction to that observed in the other mesoporous sample. This drop was not proportional to the BAS density decrease, and thus inferred the presence of synergistic sites in a higher concentration in Y15.

Na-titration helped understanding the impact of these alleged synergistic sites. In the parent zeolite Y2.6 a small degree of MTL is found and the sites presented comparable performance throughout the whole range of titration. Whereas in Y15 and Y30 an unusual and sharp drop was observed within low degrees of exchange. As titration progressed a linear drop was observed for these two catalysts showing that the majority of the sites are alike and that only a fraction has this synergism. An important observation was the near zero conversion of around 60% of the site density in all the cases. It was pointed out a probable isooctane inaccessibility to some sites, but it is also possible that those are active enough to adsorb isopropyl amine and be counted during the characterization technique but does not have enough strength to contribute into isooctane catalytic activity.

Within the particularities of isooctane cracking, the changes in product selectivity favoring an initial H-transfer from the reactant and carbenium formation ion rather than isooctane protonation and carbonium ion formation were a mere result of inactivating sites that are kinetic relevant to one step over the other. Sodium was able to detect their presence, however by using a bivalent cation metal as calcium, sites in close proximity were simultaneously titrated, and thus a shift towards H-transfer occurred. Cobalt was also used to titrate the pair-sites but this catalyst is likely to also participate in dehydrogenation reactions and distorts the results understanding.

Differences in flow and pulse mode reactions in the gas-phase demonstrate the particularity of each reaction mode and how important it is to choose the appropriate conditions beforehand. Pulse reactions presented to be more relevant in detecting zeolite uniqueness while flow mode revealed a similar behavior for all the catalysts besides the contrast difference in the concentration of acid sites. Yet, the results combination clarified the hypotheses and assisted in proving them individually.

References

[1] A. Corma, S. Zones, and J. Cejka, *Zeolites and Catalysis: Synthesis, Reactions and Applications,* p.^pp. 918: John Wiley & Sons, 2010.

[2] J. Weitkamp, "Zeolites and catalysis," *Solid State Ionics,* vol. 131, no. 1-2, pp. 175-188, 2000.

[3] K. Margeta, and A. Farkaš, *"Introductory Chapter: Zeolites - From Discovery to New Applications on the Global Market," Zeolites - New Challenges*, p.^pp. 150, 2020.

[4] R. L. Hay, and R. A. Sheppard, "Occurrence of Zeolites in Sedimentary Rocks: An Overview," *Reviews in Mineralogy and Geochemistry,* vol. 45, pp. 217-234, 2001.

[5] M. E. Davis, "Ordered porous materials for emerging applications," *Nature,* vol. 417, pp. 813-821, 2002.

[6] M. E. Davis, "New Vistas in Zeolite and Molecular Sieve Catalysis," *Accounts of Chemical Research,* vol. 26, pp. 111-115, 1993.

[7] M. Vallet-Regi, A. Rámila, R. P. d. Real, and J. Pérez-Pariente, "A New Property of MCM-41: Drug Delivery System," *Chemistry of Materials,* vol. 13, pp. 308-311, 2001.

[8] L. D. Rollmann, and D. E. Walsh, "Shape selectivity and carbon formation in zeolites," *Journal of Catalysis,* vol. 56, pp. 139-140, 1979.

[9] B. Smit, and T. L. M. Maesen, "Towards a molecular understanding of shape selectivity," *Nature,* vol. 451, pp. 671-678, 2008.

[10] C. N. Satterfield, "Mass transfer in heterogeneous catalysis," *MIT Press,* vol. 16, pp. 267, 1970.

[11] M. Chiappero, P. T. M. Do, S. Crossley, L. L. Lobban, and D. E. Resasco, "Direct conversion of triglycerides to olefins and paraffins over noble metal supported catalysts," *Fuel,* vol. 90, no. 3, pp. 1155-1165, 2011.

[12] J. A. Moulijn, M. Makkee, and R. J. Berger, "Catalyst testing in multiphase micro-packed-bed reactors; criterion for radial mass transport," *Catalysis Today,* vol. 259, pp. 354-359, 2016.

[13] A. J. Porter, and A. J. O'Malley, "A Classical Molecular Dynamics Study on the Effect of Si/Al Ratio and Silanol Nest Defects on Water Diffusion in Zeolite HY," *Journal of Physical Chemistry C,* vol. 125, no. 21, pp. 11567-11579, 2021.

[14] A. Corma, M. S. Grande, V. Gonzalez-Alfaro, and A. V. Orchilles, "Cracking Activity and Hydrothermal Stability of MCM-41 and Its Comparison with Amorphous Silica-Alumina and a USY Zeolite," *Journal of Catalysis,* vol. 159, no. 2, pp. 375-382, 1996.

[15] R. Srivastava, M. Choi, and R. Ryoo, "Mesoporous materials with zeolite framework: remarkable effect of the hierarchical structure for retardation of catalyst deactivation," *Chemical Communications,* no. 43, pp. 4489-4491, 2006.

[16] Y. Zhang, J. Song, J. Q. Mayta, F. Pan, X. Gao, M. Li, Y. Song, M. Wang, X. Cao, and Z. Jiang, "Enhanced desulfurization performance of hybrid membranes using embedded hierarchical porous SBA-15," *Frontiers of Chemical Science and Engineering,* vol. 14, pp. 661-672, 2020.

[17] G. Noh, E. Iglesia, Z. Shi, and S. I. Zones, "Isomerization and β-scission reactions of alkanes on bifunctional metal-acid catalysts: Consequences of confinement and diffusional constraints on reactivity and selectivity," *Journal of Catalysis,* vol. 368, pp. 389-410, 2018.
[18] J. V. Smith, "Definition of a zeolite," *Zeolites,* vol. 4, no. 4, pp. 309-310, 1984.
[19] S. Wang, and Y. Peng, "Natural zeolites as effective adsorbents in water and wastewater treatment," *Chemical Engineering Journal,* vol. 156, no. 1, pp. 11-24, 2010.
[20] B. Yue, S. Liu, Y. Chai, G. Wu, N. Guan, and L. Li, "Zeolites for separation: Fundamental and application," *Journal of Energy Chemistry,* vol. 71, pp. 288-303, 2022.
[21] W.-X. Zhang, H. Yahiro, N. Mizuno, J. IzumV, and M. Iwamoto, "Removal of Nitrogen Monoxide on Copper Ion-Exchanged Zeolites by Pressure Swing Adsorption," *Langmuir,* vol. 9, pp. 2337-2343, 1993.
[22] C. S. Cundy, and P. A. Cox, "The Hydrothermal Synthesis of Zeolites: History and Development from the Earliest Days to the Present Time," *Chemical Reviews,* vol. 103, no. 3, pp. 663-702, 2003.
[23] R. Szostak, *Handbook Of Molecular Sieves*, p.^pp. 584: Springer Dordrecht, 1992.
[24] J. Cejka, H. v. Bekkum, A. Corma, and F. Schueth, *Introduction to Zeolite: Science and Practice*, p.^pp. 1094: Elsevier Science, 2007.
[25] I. Levin, and D. Brandon, "Metastable Alumina Polymorphs: Crystal Structures and Transition Sequences," *Journal of the American Ceramic Society,* vol. 81, no. 8, pp. 1995-2012, 2005.
[26] A. Navrotsky, K. L. Geisinger, P. McMillan, and G. V. Gibbs, "The tetrahedral framework in glasses and melts — inferences from molecular orbital calculations and implications for structure, thermodynamics, and physical properties," *Physics and Chemistry of Minerals,* vol. 11, pp. 284-298, 1985.
[27] S.-Z. Lu, and A. Hellawell, "The mechanism of silicon modification in aluminum-silicon alloys: Impurity induced twinning," *Metallurgical Transactions A,* vol. 18, pp. 1721-1733, 1987.
[28] A. Corma, "Inorganic Solid Acids and Their Use in Acid-Catalyzed Hydrocarbon Reactions," *Chemical Reviews,* vol. 95, no. 3, pp. 559-614, 1995.
[29] B. Xu, S. Bordiga, R. Prins, and J. A. v. Bokhoven, "Effect of framework Si/Al ratio and extra-framework aluminum on the catalytic activity of Y zeolite," *Applied Catalysis A: General,* vol. 333, no. 2, pp. 245-253, 2007.
[30] M. A. Ali, B. Brisdon, and W. J. Thomas, "Synthesis, characterization and catalytic activity of ZSM-5 zeolites having variable silicon-to-aluminum ratios," *Applied Catalysis A: General,* vol. 252, no. 1, pp. 149-162, 2003.
[31] D. Si, M. Zhu, X. Sun, M. Xue, Y. Li, T. Wu, T. Gui, I. Kumakiri, X. Chen, and H. Kita, "Formation process and pervaporation of high aluminum ZSM-5 zeolite membrane with fluoride-containing and organic template-free gel," *Separation and Purification Technology,* vol. 257, pp. 117963, 2021.
[32] A. Mitra, Z. Wang, T. Cao, H. Wang, L. Huang, and Y. Yan, "Synthesis and Corrosion Resistance of High-Silica Zeolite MTW, BEA, and MFI Coatings on Steel and Aluminum," *Journal of The Electrochemical Society,* vol. 149, pp. B472-B478, 2002.

[33] K. D. Hammonds, V. Heine, and M. T. Dove, "Rigid-Unit Modes and the Quantitative Determination of the Flexibility Possessed by Zeolite Frameworks," *Journal of Physical Chemistry B,* vol. 102, no. 10, pp. 1759-1767, 1998.
[34] A. Corma, "State of the art and future challenges of zeolites as catalysts," *Journal of Catalysis,* vol. 216, no. 1-2, pp. 298-312, 2003.
[35] J. Liang, Z. Liang, R. Zou, and Y. Zhao, "Heterogeneous Catalysis in Zeolites, Mesoporous Silica, and Metal–Organic Frameworks," *Advanced Materials,* vol. 29, no. 30, 2017.
[36] J. Scherzer, *Octane-Enhancing Zeolitic FCC Catalysts: Scientific and Technical Aspects*: New York, 1990.
[37] J. E. Naber, K. P. d. Jong, W. H. J. Stork, H. P. C. E. Kuipers, and M. F. M. Post, "Industrial applications of zeolite catalysis," *Studies in Surface Science and Catalysis,* vol. 84, pp. 2197-2219, 1994.
[38] M. Guisnet, and N. S. Gnep, "Mechanism of short-chain alkane transformation over protonic zeolites. Alkylation, disproportionation and aromatization," *Applied Catalysis A: General,* vol. 146, no. 1, pp. 33-64, 1996.
[39] E. F. Iliopoulou, S. D. Stefanidis, K. G. Kalogiannis, A. Delimitis, A. A. Lappas, and K. S. Triantafyllidis, "Catalytic upgrading of biomass pyrolysis vapors using transition metal-modified ZSM-5 zeolite," *Applied Catalysis B: Environmental,* vol. 127, pp. 281-290, 2012.
[40] J. Xiao, M. Yang, Q. Che, Y. Chen, X. Chen, H. Yang, P. Bartocci, F. Fantozzi, and H. Chen, "Effect of potassium on catalytic characteristics of ZSM-5 zeolite in fast pyrolysis of biomass-based furan," *Journal of Analytical and Applied Pyrolysis,* vol. 157, pp. 105230, 2021.
[41] L. B. Young, S. A. Butter, and W. W. Kaeding, "Shape selective reactions with zeolite catalysts: III. Selectivity in xylene isomerization, toluene-methanol alkylation, and toluene disproportionation over ZSM-5 zeolite catalysts," *Journal of Catalysis,* vol. 76, no. 2, pp. 418-432, 1982.
[42] M. Guisnet, N. S. Gnep, D. Aittaleb, and Y. J. Doyemet, "Conversion of light alkanes into aromatic hydrocarbons: VI. Aromatization of C2-C4 alkanes on H-ZSM-5 —reaction mechanisms," *Applied Catalysis A: General,* vol. 87, no. 2, pp. 255-270, 1992.
[43] L. Calabrese, and E. Proverbio, "A Brief Overview on the Anticorrosion Performances of Sol-Gel Zeolite Coatings," *Coatings,* vol. 9, no. 6, pp. 409, 2019.
[44] Q. L. Wang, G. Giannetto, M. Torrealba, G. Perot, C. Kappenstein, and M. Guisnet, "Dealumination of zeolites II. Kinetic study of the dealumination by hydrothermal treatment of a NH4NaY zeolite," *Journal of Catalysis,* vol. 130, no. 2, pp. 459-470, 1991.
[45] B. H. Wouters, T. Chen, and P. J. Grobet, "Steaming of Zeolite Y: Formation of Transient Al Species," *Journal of Physical Chemistry B,* vol. 105, pp. 1135-1139, 2001.
[46] B. H. Wouters, T. H. Chen, and P. J. Grobet, "Reversible Tetrahedral−Octahedral Framework Aluminum Transformation in Zeolite Y," *Journal of American Chemical Society,* vol. 120, pp. 11419-11425, 1998.

[47] R. Dimitrijevic, W. Lutz, and A. Ritzmann, “Hydrothermal stability of zeolites: Determination of extra-framework species of H-Y faujasite-type steamed zeolite,” *Journal of Physics and Chemistry of Solids,* vol. 67, no. 8, pp. 1741-1748, 2006.
[48] K. Khivantsev, N. R. Jaegers, L. Kovarik, M. A. Derewinski, J.-H. Kwak, and J. Szanyi, “On the Nature of Extra-Framework Aluminum Species and Improved Catalytic Properties in Steamed Zeolites,” *Molecules,* vol. 27, pp. 2352, 2022.
[49] P. J. Grobet, H. Geerts, M. Tielen, J. A. Martens, and P. A. Jacobs, “Framework and Non-Framework Al Species in Dealuminated Zeolite Y,” *Studies in Surface Science and Catalysis,* vol. 46, pp. 721-734, 1989.
[50] X. Yi, K. Liu, W. Chen, J. Li, S. Xu, C. Li, Y. Xiao, H. Liu, X. Guo, S.-B. Liu, and A. Zheng, “Origin and Structural Characteristics of Tri-coordinated Extra-framework Aluminum Species in Dealuminated Zeolites,” *Journal of American Chemical Society,* vol. 140, no. 34, pp. 10764-10774, 2018.
[51] A. Primo, and H. Garcia, “Zeolites as catalysts in oil refining,” *Chemical Society Reviews,* vol. 43, pp. 7548-7561, 2014.
[52] A. Corma, A. Martínez, P. A. Arroyo, J. L. F. Monteiro, and E. F. Sousa-Aguiar, “Isobutane/2-butene alkylation on zeolite beta: Influence of post-synthesis treatments,” *Applied Catalysis A: General,* vol. 142, no. 1, pp. 139-150, 1996.
[53] M. Guisnet, and P. Magnoux, “Coking and deactivation of zeolites: Influence of the Pore Structure,” *Applied Catalysis,* vol. 54, no. 1, pp. 1-27, 1989.
[54] Q. L. Wang, G. Giannetto, and M. Guisnet, “Dealumination of zeolites III. Effect of extra-framework aluminum species on the activity, selectivity, and stability of Y zeolites in n-heptane cracking,” *Journal of Catalysis,* vol. 130, no. 2, pp. 471-482, 1991.
[55] B. Paweewan, P. J. Barrie, and L. F. Gladden, “Coking and deactivation during n-hexane cracking in ultrastable zeolite Y,” *Applied Catalysis A: General,* vol. 185, no. 2, pp. 259-268, 1999.
[56] M. Guisnet, and P. Magnoux, “Deactivation by coking of zeolite catalysts. Prevention of deactivation. Optimal conditions for regeneration,” *Catalysis Today,* vol. 36, no. 4, pp. 477-483, 1997.
[57] E. Tabor, M. Bernauer, B. Wichterlová, and J. Dedecek, “Enhancement of propene oligomerization and aromatization by proximate protons in zeolites; FTIR study of the reaction pathway in ZSM-5,” *Catalysis Science & Technology,* vol. 9, pp. 4262-4275, 2019.
[58] J. Dědeček, D. Kaucký, B. Wichterlová, and O. Gonsiorováb, “Co2+ ions as probes of Al distribution in the framework of zeolites. ZSM-5 study,” *Physical Chemistry Chemical Physics,* vol. 4, no. 5406-5413, 2002.
[59] J. Li, “Continuous Flow Hydrothermal Synthesis of ZSM-5 Zeolite,” University of Pittsburgh, 2022.
[60] C. S. Cundy, M. S. Henty, and R. J. Plaisted, “Investigation of Na, TPA-ZSM-5 zeolite synthesis by chemical methods,” *Zeolies,* vol. 15, no. 4, pp. 342-352, 1995.
[61] M. Ghamami, and L. B. Sand, “Synthesis and crystal growth of zeolite (NH4, TPA)-ZSM-5,” *Zeolites,* vol. 3, no. 2, pp. 155-162, 1983.
[62] A. Chawla, R. Li, R. Jain, R. J. Clark, J. G. Sutjianto, J. C. Palmer, and J. D. Rimer, “Cooperative effects of inorganic and organic structure-directing agents in ZSM-5

crystallization," *Molecular Systems Design & Engineering,* vol. 3, no. 1, pp. 159-170, 2018.
[63] H. Liu, H. Wang, A.-H. Xing, and J.-H. Cheng, "Effect of Al Distribution in MFI Framework Channels on the Catalytic Performance of Ethane and Ethylene Aromatization," *Journal of Physical Chemistry C,* vol. 123, pp. 15637-15647, 2019.
[64] T. Yokoi, H. Mochizuki, T. Biligetu, Y. Wang, and T. Tatsumi, "Unique Al Distribution in the MFI Framework and Its Impact on Catalytic Properties," *Chemistry Letters,* vol. 46, no. 6, pp. 798-800, 2017.
[65] R. Gounder, and E. Iglesia, "The Roles of Entropy and Enthalpy in Stabilizing Ion-Pairs at Transition States in Zeolite Acid Catalysis," *Accounts of Chemical Research,* vol. 45, no. 2, pp. 229-238, 2012.
[66] A. Bhan, and E. Iglesia, "A Link between Reactivity and Local Structure in Acid Catalysis on Zeolites," *Accounts of Chemical Research,* vol. 41, pp. 559-567, 2008.
[67] J. Cejka, *Zeolites and Ordered Mesoporous Materials: Progress and Prospects*: Elsevier Science, 2005.
[68] C. D. Chang, "Methanol Conversion to Light Olefins," *Catalysis Reviews,* vol. 26, pp. 323-345, 1984.
[69] T. W. G. Solomons, and C. B. Fryhle, *Organic Chemistry*, 8th ed.: Wiley, 2003.
[70] D. G. Truhlar, B. C. Garrett, and S. J. Klippenstein, "Current Status of Transition-State Theory," *Journal of Physical Chemistry,* vol. 100, pp. 12771-12800, 1996.
[71] A. Warshel, M. Štrajbl, J. Villà, and J. Florián, "Remarkable Rate Enhancement of Orotidine 5'-Monophosphate Decarboxylase Is Due to Transition-State Stabilization Rather Than to Ground-State Destabilization," *Biochemistry,* vol. 39, pp. 14728-14738, 2000.
[72] H. Chongfu, "Principle of information diffusion," *Fuzzy Sets and Systems,* vol. 91, no. 1, pp. 69-90, 1997.
[73] A. Fick, "Ueber Diffusion," *Annalen der Physik,* vol. 170, no. 1, pp. 59-86, 1855.
[74] K. Cao, D. Fan, L. Li, B. Fan, L. Wang, D. Zhu, Q. Wang, P. Tian, and Z. Liu, "Insights into the Pyridine-Modified MOR Zeolite Catalysts for DME Carbonylation," *ACS Catalysis,* vol. 10, pp. 3372-3380, 2020.
[75] D. H. OLSON, and W. O. HAAG, "Structure-Selectivity Relationship in Xylene Isomerization and Selective Toluene Disproportionation," 1984.
[76] H. S. Fogler, *Elements of Chemical Reaction Engineering*: Pearson, 2016.
[77] M. J. Wulfers, and R. F. Lobo, "Assessment of mass transfer limitations in oligomerization of butene at high pressure on H-beta," *Applied Catalysis A: General,* vol. 505, pp. 394-401, 2015.
[78] M. Tromp, J. A. v. Bokhoven, M. T. G. Oostenbrink, J. H. Bitter, K. P. d. Jong, and D. C. Koningsberger, "Influence of the Generation of Mesopores on the Hydroisomerization Activity and Selectivity of n-Hexane over Pt/Mordenite," *Journal of Catalysis,* vol. 190, no. 2, pp. 209-214, 2000.
[79] K. Sun, J. Lu, L. Ma, Y. Han, Z. Fu, and J. Ding, "A comparative study on the catalytic performance of different types of zeolites for biodiesel production," *Fuel,* vol. 158, pp. 848-854, 2015.
[80] H. G. Karge, and W. Nießen, "A new method for the study of diffusion and counter-diffusion in zeolites," *Catalysis Today,* vol. 8, no. 4, pp. 451-465, 1991.

[81] P. Peng, D. Stosic, A. Aitblal, A. Vimont, P. Bazin, X.-M. Liu, Z.-F. Yan, S. Mintova, and A. Travert, "Unraveling the Diffusion Properties of Zeolite-Based Multicomponent Catalyst by Combined Gravimetric Analysis and IR Spectroscopy (AGIR)," *ACS Catalysis,* vol. 10, pp. 6822-6830, 2020.

[82] J. Kärger, and H. Pfeifer, "N.m.r. self-diffusion studies in zeolite science and technology," *Zeolites,* vol. 7, no. 2, pp. 90-107, 1987.

[83] P. Cnudde, E. A. Redekop, W. Dai, N. G. Porcaro, M. Waroquier, S. Bordiga, M. Hunger, L. Li, U. Olsbye, and V. V. Speybroeck, "Experimental and Theoretical Evidence for the Promotional Effect of Acid Sites on the Diffusion of Alkenes through Small-Pore Zeolites," *Angewandte Chemie,* vol. 133, no. 18, pp. 10104-10110, 2021.

[84] D. E. Mears, "Tests for Transport Limitations in Experimental Catalytic Reactors," *Industrial & Engineering Chemistry Process Design and Development,* vol. 10, pp. 541-547, 1971.

[85] P. B. Weisz, and C. D. Prater, "Interpretation of Measurements in Experimental Catalysis," *Advances in Catalysis,* vol. 6, pp. 143-196, 1954.

[86] M. Mohagheghi, G. Bakeri, and M. Saeedizad, "Study of the Effects of External and Internal Diffusion on the Propane Dehydrogenation Reaction over Pt-Sn/Al2O3 Catalyst," *Chemical Engineering Technology,* vol. 30, no. 12, pp. 1721-1725, 2007.

[87] H. Konno, T. Okamura, T. Kawahara, Y. Nakasaka, T. Tago, and T. Masuda, "Kinetics of n-hexane cracking over ZSM-5 zeolites – Effect of crystal size on effectiveness factor and catalyst lifetime," *Chemical Engineering Journal,* vol. 207-208, pp. 490-496, 2012.

[88] E. W. Thiele, "Relation between Catalytic Activity and Size of Particle," *Industrial and Engineering Chemistry,* vol. 31, pp. 916-920, 1939.

[89] F. C. Meunier, D. Verboekend, J.-P. Gilson, J. C. Groen, and J. Pérez-Ramírez, "Influence of crystal size and probe molecule on diffusion in hierarchical ZSM-5 zeolites prepared by desilication," *Microporous and Mesoporous Materials,* vol. 148, no. 1, pp. 115-121, 2012.

[90] J. C. Groen, W. Zhu, S. Brouwer, S. J. Huynink, F. Kapteijn, J. A. Moulijn, and J. Pérez-Ramírez, "Direct Demonstration of Enhanced Diffusion in Mesoporous ZSM-5 Zeolite Obtained via Controlled Desilication," *Journal of American Chemical Society,* vol. 129, pp. 355-360, 2007.

[91] B. A. Williams, S. M. Babitz, J. T. Miller, R. Q. Snurr, and H. H. Kung, "The roles of acid strength and pore diffusion in the enhanced cracking activity of steamed Y zeolites," *Applied Catalysis A: General,* vol. 177, no. 2, pp. 161-175, 1999.

[92] J. G. S. Monteiro, A. G. H. Barbosa, A. M. Henriques, P. H. G. Neves, R. S. Furtado, R. M. Menezes, A. R. d. Santos, and F. P. Fleming, "Assessing the Molecular Basis of the Fuel Octane Scale: A Detailed Investigation on the Rate Controlling Steps of the Autoignition of Heptane and Isooctane," *Journal of Physical Chemistry A,* vol. 122, no. 2, pp. 610-630, 2018.

[93] K. A. CUMMING, and W. WOJCIECHOWSKI, "Hydrogen Transfer, Coke Formation, and Catalyst Decay and Their Role in the Chain Mechanism of Catalytic Cracking," *Catalysis Letters,* vol. 38, pp. 101-157, 1996.

[94] M. V. Twigg, *Catalyst Handbook*, p.^pp. 608, New York, 1989.

[95] M. B. Smith, and J. March, *March's Advanced Organic Chemistry: Reactions, Mechanisms, and Structure*, p.^pp. 2083: Wiley-Interscience, 2001.
[96] A. T. Nielsen, and W. J. Houlihan, "The Aldol Condensation," *Organic Reactions*, no. 16, pp. 1-438, 2004.
[97] Y. C., and M. Z.Y., "Bimolecular Condensation of Ethanol to 1-Butanol Catalyzed by Alkali Cation Zeolites," *Journal of Catalysis*, vol. 142, no. 1, pp. 37-44, 1993.
[98] G. Li, D. T. Ngo, Y. Yan, Q. Tan, B. Wang, and D. E. Resasco, "Factors Determining Selectivity of Acid- and Base-Catalyzed Self- and Cross-Condensation of Acetone and Cyclopentanone," *ACS Catalysis*, vol. 10, pp. 12790-12800, 2020.
[99] W. O. Haag, R. M. Dessau, and R. M. Lago, "Kinetics and Mechanism of Paraffin Cracking with Zeolite Catalysts," *Studies in Surface Science and Catalysis*, vol. 60, pp. 255-265, 1991.
[100] A. Corma, and B. W. Wojciechowski, "The Chemistry of Catalytic Cracking," *Catalysis Letters*, vol. 27, no. 1, pp. 29-150, 1985.
[101] S. Kotrel, H. Knözinger, and B. C. Gates, "The Haag–Dessau mechanism of protolytic cracking of alkanes," *Microporous and Mesoporous Materials*, vol. 35-36, pp. 11-20, 2000.
[102] W. O. Haag, R. M. Lago, and P. B. Weisz, "Transport and reactivity of hydrocarbon molecules in a shape-selective zeolite," *Faraday Discussions of the Chemical Society*, vol. 72, pp. 317-330, 1981.
[103] E. V. Anslyn, and D. A. Dougherty, *Modern Physical Organic Chemistry*, p.^pp. 1104: University Science, 2005.
[104] K. A. Gould, and I. A. Wiehe, "Natural Hydrogen Donors in Petroleum Resids," *Energy & Fuels*, vol. 21, no. 3, pp. 1199-1204, 2007.
[105] S. Herrmann, and E. Iglesia, "Selective conversion of acetone to isobutene and acetic acid on aluminosilicates: Kinetic coupling between acid-catalyzed and radical-mediated pathways," *Journal of Catalysis*, vol. 360, pp. 66-80, 2018.
[106] Y. Nakagawa, M. Tamura, and K. Tomishige, "Recent development of production technology of diesel- and jet-fuel-range hydrocarbons from inedible biomass," *Fuel Processing Technology*, vol. 193, pp. 404-422, 2019.
[107] D. E. Resasco, and S. P. Crossley, "Implementation of concepts derived from model compound studies in the separation and conversion of bio-oil to fuel," *Catalysis Today*, vol. 257, pp. 185-199, 2015.
[108] G. W. Huber, J. N. Chheda, C. J. Barrett, and J. A. Dumesic, "Production of Liquid Alkanes by Aqueous-Phase Processing of Biomass-Derived Carbohydrates," *Science*, vol. 308, no. 5727, pp. 1446-1450, 2005.
[109] G. W. Huber, and A. Corma, "Synergies between Bio- and Oil Refineries for the Production of Fuels from Biomass," *Angewandte Chemie International*, vol. 46, no. 38, pp. 7184-7201, 2007.
[110] C. Liu, H. Wang, A. M. Karim, J. Suna, and Y. Wang, "Catalytic fast pyrolysis of lignocellulosic biomass," *Chemical Society Reviews*, vol. 43, no. 22, pp. 7594-7623, 2014.
[111] M. Stöcker, "Biofuels and Biomass-To-Liquid Fuels in the Biorefinery: Catalytic Conversion of Lignocellulosic Biomass using Porous Materials," *Angewandte Chemie International*, vol. 47, no. 48, pp. 9200-9211, 2008.

[112] D. C. Elliott, D. Beckman, A. V. Bridgwater, J. P. Diebold, S. B. Gevert, and Y. Solantausta, "Developments in Direct Thermochemical Liquefaction of Biomass: 1983-1990," *Energy & Fuels,* vol. 5, pp. 399-410, 1991.
[113] V. K. Díez, C. R. Apesteguía, and J. I. D. Cosimo, "Aldol condensation of citral with acetone on MgO and alkali-promoted MgO catalysts," *Journal of Catalysis,* vol. 240, no. 2, pp. 235-244, 2006.
[114] C. L. Perrin, and K.-L. Chang, "The Complete Mechanism of an Aldol Condensation," *The Journal of Organic Chemistry,* vol. 81, no. 13, pp. 5631-5635, 2016.
[115] M. J. L. Gines, and E. Iglesia, "Bifunctional Condensation Reactions of Alcohols on Basic Oxides Modified by Copper and Potassium," *Journal of Catalysis,* vol. 176, no. 1, 1998.
[116] G. Li, S. Dissanayake, S. L. Suib, and D. E. Resasco, "Activity and stability of mesoporous CeO2 and ZrO2 catalysts for the self-condensation of cyclopentanone," *Applied Catalysis B: Environmental,* vol. 267, pp. 118373, 2020.
[117] O. Kikhtyanin, V. Kelbichová, D. Vitvarová, M. Kubů, and D. Kubička, "Aldol condensation of furfural and acetone on zeolites," *Catalysis Today,* vol. 227, pp. 154-162, 2014.
[118] S. Herrmann, and E. Iglesia, "Elementary steps in acetone condensation reactions catalyzed by aluminosilicates with diverse void structures," *Journal of Catalysis,* vol. 346, pp. 134-153, 2017.
[119] G. Li, B. Wang, B. Chen, and D. E. Resasco, "Role of water in cyclopentanone self-condensation reaction catalyzed by MCM-41 functionalized with sulfonic acid groups," *Journal of Catalysis,* vol. 377, pp. 245-254, 2019.
[120] X. Solans-Monfort, J. Bertran, V. Branchadell, and M. Sodupe, "Keto−Enol Isomerization of Acetaldehyde in HZSM5. A Theoretical Study Using the ONIOM2 Method," *Journal of Physical Chemistry,* vol. 106, pp. 10220-10226, 2002.
[121] T. Yan, S. Yao, W. Dai, G. Wu, N. Guan, and L. Li, "Self-aldol condensation of aldehydes over Lewis acidic rare-earth cations stabilized by zeolites," *Chinese Journal of Catalysis,* vol. 42, no. 2, pp. 595-605, 2021.
[122] C. L. Perrin, "The Complete Mechanism of an Aldol Condensation," *The Journal of Organic Chemistry,* vol. 81, no. 13, pp. 5631-5635, 2016.
[123] R. J. Madon, and M. Boudart, "Experimental criterion for the absence of artifacts in the measurement of rates of heterogeneous catalytic reactions," *Industrial & Chemical Engineering Fundamentals,* vol. 21, pp. 438-447, 1982.
[124] H. K. Chau, D. E. Resasco, P. Dob, and S. P. Crossley, "Acylation of m-cresol with acetic acid supported by in-situ ester formation on H-ZSM-5 zeolites," *Journal of Catalysis,* vol. 406, pp. 48-55, 2022.
[125] A. Gumidyala, T. Sooknoi, and S. Crossley, "Selective ketonization of acetic acid over HZSM-5: The importance of acyl species and the influence of water," *Journal of Catalysis,* vol. 340, pp. 76-84, 2016.
[126] L. García, G. Giannetto, M. R. Goldwasser, M. Guisnet, and P. Magnoux, "Phenol alkylation with methanol: effect of sodium content and ammonia selective poisoning of an HY zeolite," *Catalysis Letters,* vol. 37, pp. 121-123, 1996.

[127] P. M. Kester, J. T. Crumb, S. Li, W. F. Schneider, and R. Gounder, "Effects of Brønsted acid site proximity in chabazite zeolites on OH infrared spectra and protolytic propane cracking kinetics," *Journal of Catalysis,* vol. 395, pp. 210-226, 2021.
[128] K. Chen, M. Abdolrahmani, S. Horstmeier, T. N. Pham, V. T. Nguyen, M. Zeets, B. Wang, S. Crossley, and J. L. White, "Brønsted–Brønsted Synergies between Framework and Noncrystalline Protons in Zeolite H-ZSM-5," *ACS Catalysis,* vol. 9, no. 7, pp. 6124-6136, 2019.
[129] A. Bhan, A. D. Allian, G. J. Sunley, D. J. Law, and E. Iglesia, "Specificity of Sites within Eight-Membered Ring Zeolite Channels for Carbonylation of Methyls to Acetyls," *Journal of American Chemical Society,* vol. 129, no. 16, pp. 4919-4924, 2007.
[130] V. A. Veefkind, M. L. Smidt, and J. A. Lercher, "On the role of strength and location of Brønsted acid sites for ethylamine synthesis on mordenite catalysts," *Applied Catalysis A: General,* vol. 194-195, pp. 319-332, 2000.
[131] V. L. Zholobenko, M. A. Makarova, and J. Dwyer, "Inhomogeneity of Broensted acid sites in H-mordenite," *Journal of Physical Chemistry,* vol. 97, no. 22, pp. 5962-5964, 1993.
[132] M. A. Makarova, A. E. Wilson, B. J. v. Liemt, C. M. A. M. Mesters, A. W. d. Winter, and C. Williams, "Quantification of Brønsted Acidity in Mordenites," *Journal of Catalysis,* vol. 172, no. 1, pp. 170-177, 1997.
[133] J. W. Ward, "A spectroscopic study of the surface of zeolite Y: the adsorption of pyridine," *Journal of Colloid and Interface Science,* vol. 28, no. 2, pp. 269-278, 1968.
[134] O. A. Abdelrahman, K. P. Vinter, L. Ren, D. Xu, R. J. Gorte, M. Tsapatsis, and P. J. Dauenhauer, "Simple quantification of zeolite acid site density by reactive gas chromatography," *Catalysis Science & Technology,* vol. 7, no. 17, pp. 3831-3841, 2017.
[135] T. Danuthai, S. Jongpatiwut, T. Rirksomboon, S. Osuwana, and D. E. Resasco, "Conversion of methylesters to hydrocarbons over an H-ZSM5 zeolite catalyst," *Applied Catalysis A: General,* vol. 361, no. 1-2, pp. 99-105, 2009.
[136] R. Gounder, A. J. Jones, R. T. Carr, and E. Iglesia, "Solvation and acid strength effects on catalysis by faujasite zeolites," *Journal of Catalysis,* vol. 286, pp. 214-223, 2012.
[137] M. J. Kim, S. M. Park, S.-J. Song, J. Won, J. Y. Lee, M. Yoon, K. Kim, and G. Seo, "Adsorption of pyridine onto the metal organic framework MIL-101," *Journal of Colloid and Interface Science,* vol. 361, no. 2, pp. 612-617, 2011.
[138] H. Bludau, H. G. Karge, and W. Niessen, "Sorption, sorption kinetics and diffusion of pyridine in zeolites," *Microporous and Mesoporous Materials,* vol. 22, no. 1-3, pp. 297-308, 1998.
[139] D. T. Yazıcı, and C. Bilgiç, "Determining the surface acidic properties of solid catalysts by amine titration using Hammett indicators and FTIR-pyridine adsorption methods," *Surface and Interface Analysis,* vol. 42, no. 6-7, pp. 959-962, 2010.

[140] J. N. Hall, and P. Bollini, "Metal–Organic Framework MIL-100 Catalyzed Acetalization of Benzaldehyde with Methanol: Lewis or Brønsted Acid Catalysis?," *ACS Catalysis,* vol. 10, no. 6, pp. 3750-3763, 2020.
[141] C. D. Baertsch, K. T. Komala, Y.-H. Chua, and E. Iglesia, "Genesis of Brønsted Acid Sites during Dehydration of 2-Butanol on Tungsten Oxide Catalysts," *Journal of Catalysis,* vol. 205, no. 1, pp. 44-57, 2002.
[142] A. Corma, V. Fornés, L. Forni, F. Márquez, J. Martínez-Triguero, and D. Moscotti, "2,6-Di-Tert-Butyl-Pyridine as a Probe Molecule to Measure External Acidity of Zeolites," *Journal of Catalysis,* vol. 179, no. 2, pp. 451-458, 1998.
[143] K. Góra-Marek, K. Tarach, and M. Choi, "2,6-Di-tert-butylpyridine Sorption Approach to Quantify the External Acidity in Hierarchical Zeolites," *Journal of Physical Chemistry,* vol. 118, no. 23, pp. 12266-12274, 2014.
[144] R. J. Argauer, *Crystalline zeolite ZSM-5 and method of preparing the same.*, USA 3702886, U. S. P. Office, 1972.
[145] W. Song, R. E. Justice, C. A. Jones, V. H. Grassian, and S. C. Larsen, "Synthesis, Characterization, and Adsorption Properties of Nanocrystalline ZSM-5," *Langmuir,* vol. 20, pp. 8301-8306, 2004.
[146] E. Epelde, J. I. Santos, P. Florian, A. T. Aguayo, A. G. Gayubo, J. Bilbao, and P. Castaño, "Controlling coke deactivation and cracking selectivity of MFI zeolite by H3PO4 or KOH modification," *Applied Catalysis A: General,* vol. 505, pp. 105-107, 2015.
[147] H. Kim, H.-G. Jang, E. Jang, S. J. Park, T. Lee, Y. Jeong, H. Baik, S. J. Cho, and J. Choi, "On methanol to hydrocarbons reactions in a hierarchically structured ZSM-5 zeolite catalyst," *Catalysis Today,* vol. 303, pp. 150-158, 2018.
[148] S. H. Jhung, J. W. Yoon, J. S. Lee, and J.-S. Chang, "Low-Temperature Adsorption/Storage of Hydrogen on FAU, MFI, and MOR Zeolites with Various Si/Al Ratios: Effect of Electrostatic Fields and Pore Structures," *Chemistry - A European Journal,* vol. 13, no. 22, pp. 6502-6507, 2007.
[149] Y. Xu, M. Chen, T. Wang, B. Liu, F. Jiang, and X. Liu, "Probing cobalt localization on HZSM-5 for efficient methane dehydroaromatization catalysts," *Journal of Catalysis,* vol. 387, 2020.
[150] C. Li, P. Ferri, C. Paris, M. Moliner, M. Boronat, and A. Corma, "Design and Synthesis of the Active Site Environment in Zeolite Catalysts for Selectively Manipulating Mechanistic Pathways," *Journal of the American Chemical Society* vol. 143, pp. 10718-10726, 2021.
[151] H. Eyring, "The Activated Complex in Chemical Reactions," *The Journal of Chemical Physics,* vol. 33, no. 2, pp. 65-77, 1935.
[152] M. Frenkel, *Thermodynamics of Organic Compounds in the Gas State*: CRC Press, 1994.
[153] S. Wang, Y. He, W. Jiao, J. Wang, and W. Fan, "Recent experimental and theoretical studies on Al siting/acid site distribution in zeolite framework," *Current Opinion in Chemical Engineering,* vol. 23, pp. 146-154, 2019.
[154] M. E. Z. Velthoen, S. Nab, and B. M. Weckhuysen, "Probing acid sites in solid catalysts with pyridine UV-Vis spectroscopy," *Physical Chemistry Chemical Physics,* vol. 20, no. 33, pp. 21647-21659, 2018.

[155] A. Palčić, and V. Valtchev, "Analysis and control of acid sites in zeolites," *Applied Catalysis A: General,* vol. 606, pp. 117795, 2020.
[156] R. B. Borade, A. Adnot, and S. Kaliaguine, "Acid sites in dehydroxylated Y zeolites: an X-ray photoelectron and infrared spectroscopic study using pyridine as a probe molecule," *Journal of the Chemical Society, Faraday Transactions,* vol. 86, no. 23, pp. 3949-3956, 1990.
[157] J. N. Kondo, R. Nishitani, E. Yoda, T. Yokoi, T. Tatsumia, and K. Domenc, "A comparative IR characterization of acidic sites on HYzeolite by pyridine and COprobes with silica–alumina and γ-alumina references," *Physical Chemistry Chemical Physics,* vol. 12, no. 37, pp. 11567-11586, 2010.
[158] O. M. Busch, W. Brijoux, S. Thomson, and F. Schüth, "Spatially resolving infrared spectroscopy for parallelized characterization of acid sites of catalysts via pyridine sorption: Possibilities and limitations," *Journal of Catalysis,* vol. 222, no. 1, pp. 174-179, 2004.
[159] J. E. Leonard, G. S. Hammond, and H. E. Simmons, "The Apparent Symmetry of Cyclohexane," *Journal of American Chemical Society,* pp. 5052-5054, 1975.
[160] D. Mootz, and H. G. Wussow, "Crystal structures of pyridine and pyridine trihydrate," *The Journal of Chemical Physics,* vol. 75, pp. 1517-1522, 1981.
[161] F. Pang, J. E. Boggs, P. Pulay, and G. Fogarasi, "The molecular structure of toluene," *Journal of Molecular Structure,* vol. 66, pp. 281-287, 1980.
[162] J. Datka, "Adsorption of benzene and toluene on Y zeolites studied by infrared spectroscopy," *Journal of Chemical Society, Faraday Transactions 1: Physical Chemistry in Condensed Phases,* vol. 77, pp. 511-517, 1981.
[163] T. N. Pham, V. Nguyen, H. Nguyen-Phu, B. Wang, and S. Crossley, "Influence of Brønsted Acid Site Proximity on Alkane Cracking in MFI Zeolites," *ACS Catalysis,* vol. 13, no. 2, pp. 1359-1370, 2023.
[164] M. Yoldi, E. G. Fuentes-Ordoñez, S. A. Korili, and A. Gil, "Zeolite synthesis from industrial wastes," *Microporous and Mesoporous Materials,* vol. 287, pp. 183-191, 2019.
[165] A. Khaleque, M. Alam, M. Hoque, S. Mondal, J. B. Haider, B. Xu, M. A. H. Johir, A. K. Karmakar, J. L. Zhou, M. B. Ahmed, and M. A. Moni, "Zeolite synthesis from low-cost materials and environmental applications: A review," *Environmental Advances,* vol. 2, pp. 100019, 2020.
[166] J. Shin, D. Jo, and S. B. Hong, "Rediscovery of the Importance of Inorganic Synthesis Parameters in the Search for New Zeolites," *Accounts of Chemical Research,* vol. 52, no. 5, pp. 1419-1427, 2019.
[167] M. Kanezashi, and J. O'Brien, "Template-free synthesis of MFI-type zeolite membranes: Permeation characteristics and thermal stability improvement of membrane structure," *Journal of Membrane Science,* vol. 286, no. 1-2, pp. 213-222, 2006.
[168] X. H. Vu, M. S. Marschall, V. T. Tran, T. P. Ngo, T. T. Dang, D. M. Dinh, T. K. T. Dao, O. Busse, and J. J. Weigand, "Enhanced thermal stability of hierarchical Y zeolites obtained by acid and subsequent base treatments," *Journal of Physics and Chemistry of Solids,* vol. 152, pp. 109962, 2021.
[169] D. E. Resasco, S. P. Crossley, B. Wang, and J. L. White, "Interaction of water with zeolites: a review," *Catalysis Reviews,* vol. 63, pp. 302-362, 2021.

[170] R. Jain, A. Chawla, N. Linares, J. G. Martínez, and J. D. Rimer, "Spontaneous Pillaring of Pentasil Zeolites," *Advanced Materials,* vol. 33, no. 22, pp. 2100897, 2021.
[171] M. Moliner, C. Martínez, and A. Corma, "Multipore Zeolites: Synthesis and Catalytic Applications," *Angewandte Chemie International,* vol. 54, no. 12, pp. 3523-3825, 2015.
[172] M. H. Nada, S. C. Larsena, and E. G. Gillan, "Solvent-free synthesis of crystalline ZSM-5 zeolite: Investigation of mechanochemical pre-reaction impact on growth of thermally stable zeolite structures," *Solid State Sciences,* vol. 94, pp. 15-22, 2019.
[173] A. Inayat, I. Knoke, E. Spiecker, and W. Schwieger, "Assemblies of Mesoporous FAU-Type Zeolite Nanosheets," *Angewandte Chemie International,* vol. 51, no. 8, pp. 1731-1976, 2012.
[174] Y. Jiao, L. Forster, S. Xu, H. Chen, J. Han, X. Liu, Y. Zhou, J. Liu, J. Zhang, J. Yu, C. D'Agostino, and X. Fan, "Creation of Al-Enriched Mesoporous ZSM-5 Nanoboxes with High Catalytic Activity: Converting Tetrahedral Extra-Framework Al into Framework Sites by Post Treatment," *Angewandte Chemie International,* vol. 59, no. 44, pp. 19478-19486, 2020.
[175] J. C. Groen, L. A. A. Peffer, J. A. Moulijn, and J. Pérez-Ramírez, "On the introduction of intracrystalline mesoporosity in zeolites upon desilication in alkaline medium," *Microporous and Mesoporous Materials,* vol. 69, no. 1-2, pp. 29-34, 2004.
[176] D. Verboekend, S. Mitchell, M. Milina, J. C. Groen, and J. Pérez-Ramírez, "Full Compositional Flexibility in the Preparation of Mesoporous MFI Zeolites by Desilication," *The Journal of Physical Chemistry C,* vol. 115, pp. 14193-14203, 2011.
[177] X. Zhu, L. L. .Lobban, R. G. Mallinson, and D. E. Resasco, "Tailoring the mesopore structure of HZSM-5 to control product distribution in the conversion of propanal," *Journal of Catalysis,* vol. 271, no. 1, pp. 88-98, 2010.
[178] A. K. Patra, A. Dutta, M. Pramanik, M. Nandi, H. Uyama, and A. Bhaumik, "Synthesis of Hierarchical Mesoporous Mn–MFI Zeolite Nanoparticles: A Unique Architecture of Heterogeneous Catalyst for the Aerobic Oxidation of Thiols to Disulfides," *ChemCatChem,* vol. 6, no. 1, pp. 220-229, 2013.
[179] H. Wang, and T. J. Pinnavaia, "MFI Zeolite with Small and Uniform Intracrystal Mesopores," *Angewandte Chemie,* vol. 118, no. 45, pp. 7637-7805, 2006.
[180] R. F. Lobo, S. I. Zones, and M. E. Davis, "Structure-direction in zeolite synthesis," *Journal of inclusion phenomena and molecular recognition in chemistry volume,* vol. 21, pp. 47-78, 1995.
[181] M. Moliner, F. Rey, and A. Corma, "Towards the Rational Design of Efficient Organic Structure-Directing Agents for Zeolite Synthesis," *Angewandte Chemie International,* vol. 52, no. 52, pp. 13880-13889, 2013.
[182] J. Čejka, A. Corma, and S. Zones, *Zeolites and Catalysis: Synthesis, Reactions and Applications*: John Wiley & Sons, 2010.
[183] S. Soltanali, R. Halladj, A. Rashidi, and M. Bazmi, "Mixed templates application in ZSM-5 nanoparticles synthesis: Effect on the size, crystallinity, and surface area," *Advanced Power Technology,* vol. 25, no. 6, pp. 1767-1771, 2014.

[184] V. P. Valtchev, L. Tosheva, and K. N. Bozhilov, “Synthesis of Zeolite Nanocrystals at Room Temperature,” *Langmuir,* vol. 21, pp. 10724-10729, 2005.
[185] A. E. Persson, B. J. Schoeman, J. Sterte, and J.-E. Otterstedt, “Synthesis of stable suspensions of discrete colloidal zeolite (Na, TPA)ZSM-5 crystals,” *Zeolies,* vol. 15, no. 7, pp. 611-619, 1995.
[186] C. Li, Y. Wang, B. Shi, J. Ren, X. Liu, Y. Wang, Y. Guo, Y. Guo, and G. Lu, “Synthesis of hierarchical MFI zeolite microspheres with stacking nanocrystals,” *Microporous and Mesoporous Materials,* vol. 117, no. 1-2, pp. 104-110, 2009.
[187] V. P. Valtchev, A.-C. Faust, and J. Lézervant, “Rapid synthesis of silicalite-1 nanocrystals by conventional heating,” *Microporous and Mesoporous Materials,* vol. 68, no. 1-3, pp. 91-95, 2004.
[188] H. Konno, T. Okamura, Y. Nakasaka, T. Tago, and T. Masuda, “Effects of Crystal Size and Si/Al Ratio of MFI-type Zeolite Catalyst on
n-Hexane Cracking for Light Olefin Synthesis,” *Journal of the Japan Petroleum Institute,* vol. 55, pp. 267-274, 2012.
[189] S. Ahmed, M. Z. El-Faer, M. M. Abdillahi, M. A. B. Siddiqui, and S. A. I. Barri, “Investigation of the rapid crystallization method for the synthesis of MFI-type zeolites and study of the physicochemical properties of the products,” *Zeolites,* vol. 17, no. 4, pp. 373-380, 1996.
[190] L. Shirazi, E. Jamshidi, and M. R. Ghasemi, “The effect of Si/Al ratio of ZSM-5 zeolite on its morphology, acidity and crystal size,” *Crystal Research and Technology,* vol. 43, no. 12, pp. 1247-1344, 2008.
[191] R. V. Grieken, J. L. Sotelo, J. M. Menéndez, and J. A. Melero, “Anomalous crystallization mechanism in the synthesis of nanocrystalline ZSM-5,” *Microporous and Mesoporous Materials,* vol. 39, no. 1-2, pp. 135-147, 2000.
[192] T. Fu, Z. Ma, Y. Wang, J. Shao, Q. Ma, C. Zhang, L. Cui, and Z. Li, “Si/Al ratio induced structure evolution during desilication-recrystallization of silicalite-1 to synthesize nano-ZSM-5 catalyst for MTH reaction,” *Fuel Processing Technology,* vol. 194, pp. 106122, 2019.
[193] H. Dai, Y. Shen, T. Yang, C. Lee, D. Fu, A. Agarwal, T. T. Le, M. Tsapatsis, J. C. Palmer, B. M. Weckhuysen, P. J. Dauenhauer, X. Zou, and J. D. Rimer, “Finned zeolite catalysts,” *Nature Materials,* vol. 19, pp. 1074-1080, 2020.
[194] R. Ravishankar, C. E. A. Kirschhock, P.-P. Knops-Gerrits, E. J. P. Feijen, P. J. Grobet, P. Vanoppen, F. C. D. Schryver, G. Miehe, H. Fuess, B. J. Schoeman, P. A. Jacobs, and J. A. Martens, “Characterization of Nanosized Material Extracted from Clear Suspensions for MFI Zeolite Synthesis,” *Journal of Physical Chemistry B,* vol. 103, no. 24, pp. 4960-4964, 1999.
[195] J. Dedecek, V. Balgová, V. Pashkova, P. Klein, and B. Wichterlová, “Synthesis of ZSM-5 Zeolites with Defined Distribution of Al Atoms in the Framework and Multinuclear MAS NMR Analysis of the Control of Al Distribution,” *Chemistry of Materials,* vol. 24, no. 16, pp. 3231-3239, 2012.
[196] V. Pashkova, S. Sklenak, P. Klein, M. Urbanova, and J. Dědeček, “Location of Framework Al Atoms in the Channels of ZSM-5: Effect of the (Hydrothermal) Synthesis,” *Chemistry - A European Journal,* vol. 22, no. 12, pp. 3937-3941, 2016.

[197] S. M. Opalka, and T. Zhu, "Influence of the Si/Al ratio and Al distribution on the H-ZSM-5 lattice and Brønsted acid site characteristics," *Microporous and Mesoporous Materials,* vol. 222, pp. 256-270, 2016.
[198] C. E. A. Kirschhock, R. Ravishankar, F. Verspeurt, P. J. Grobet, P. A. Jacobs, and J. A. Martens, "Identification of Precursor Species in the Formation of MFI Zeolite in the TPAOH−TEOS−H2O System," *Journal of Physical Chemistry B,* vol. 103, no. 24, pp. 4965-4971, 1999.
[199] N. V. Choudary, and B. L. Newalkar, "Use of zeolites in petroleum refining and petrochemical processes: recent advances," *Journal of Porous Materials,* vol. 18, pp. 685-692, 2011.
[200] V. B. Kazansky, and I. N. Senchenya, "Quantum chemical study of the electronic structure and geometry of surface alkoxy groups as probable active intermediates of heterogeneous acidic catalysts: What are the adsorbed carbenium ions?," *Journal of Catalysis,* vol. 119, no. 1, pp. 108-120, 1989.
[201] A. F. H. Wielers, M. Vaarkamp, and M. F. M. Post, "Relation between properties and performance of zeolites in paraffin cracking," *Journal of Catalysis,* vol. 127, no. 1, pp. 51-66, 1991.
[202] J. Abbot, and B. W. Wojciechowski, "The mechanism of paraffin reactions on HY zeolite," *Journal of Catalysis,* vol. 115, no. 1, pp. 1-15, 1989.
[203] J. Abbot, "Active sites and intermediates for isomerization and cracking of cyclohexane on HY," *Journal of Catalysis,* vol. 123, no. 2, pp. 383-395, 1990.
[204] Y. V. Kissin, "Chemical Mechanism of Hydrocarbon Cracking over Solid Acidic Catalysts," *Journal of Catalysis,* vol. 163, no. 1, pp. 50-622, 1996.
[205] A. Bhan, R. Gounder, J. Macht, and E. Iglesia, "Entropy considerations in monomolecular cracking of alkanes on acidic zeolites," *Journal of Catalysis,* vol. 253, no. 1, pp. 221-224, 2008.
[206] J. A. v. Bokhoven, B. A. Williams, W. Ji, D. C. Koningsberger, H. H. Kung, and J. T. Miller, "Observation of a compensation relation for monomolecular alkane cracking by zeolites: the dominant role of reactant sorption," *Journal of Catalysis,* vol. 224, no. 1, pp. 50-59, 2004.
[207] N. Katada, S. Sota, N. Morishita, K. Okumura, and M. Niwa, "Relationship between activation energy and pre-exponential factor normalized by the number of Brønsted acid sites in cracking of short chain alkanes on zeolites," *Catalysis Science & Technology,* vol. 5, pp. 1864-1869, 2015.
[208] A. A. Avidan, *Chapter 1 Origin, Development and Scope of Fcc Catalysis,* 1993.
[209] S. v. Donk, A. H. Janssen, J. H. Bitter, and K. P. d. Jong, "Generation, Characterization, and Impact of Mesopores in Zeolite Catalysts," *Catalysis Reviews,* vol. 45, no. 2, pp. 297-319, 2007.
[210] A. Corma, V. González-Alfaro, and A. V. Orchillés, "The role of pore topology on the behaviour of FCC zeolite additives," *Applied Catalysis A: General,* vol. 187, no. 2, pp. 245-254, 1999.
[211] A. H. Janssen, A. J. Koster, and K. P. d. Jong, "On the Shape of the Mesopores in Zeolite Y: A Three-Dimensional Transmission Electron Microscopy Study Combined with Texture Analysis," *Journal of Physical Chemistry B,* vol. 106, no. 46, pp. 11905-11909, 2002.

[212] A. Corma, A. Martinez, S. Pergher, S. Peratello, C. Perego, and G. Bellusi, "Hydrocracking-hydroisomerization of n-decane on amorphous silica-alumina with uniform pore diameter," *Applied Catalysis A: General,* vol. 152, no. 1, pp. 107-125, 1997.
[213] J. Kenvin, S. Mitchell, M. Sterling, R. Warringham, T. C. Keller, P. Crivelli, J. Jagiello, and J. Pérez-Ramírez, "Quantifying the Complex Pore Architecture of Hierarchical Faujasite Zeolites and the Impact on Diffusion," *Advanced Functional Materials,* vol. 26, no. 31, pp. 5581-5763, 2016.
[214] R. Chal, C. Gérardin, M. Bulut, and S. v. Donk, "Overview and Industrial Assessment of Synthesis Strategies towards Zeolites with Mesopores," *ChemCatChem,* vol. 3, no. 1, pp. 67-81, 2011.
[215] P. G. Smirniotis, and E. Ruckenstein, "Comparison of the Performance of ZSM-5,. beta. Zeolite, Y, USY, and Their Composites in the Catalytic Cracking of n-Octane, 2, 2, 4-Trimethylpentane, and 1-Octene," *Industrial & engineering chemistry research,* vol. 33, no. 4, pp. 800-813, 1994.
[216] R. V. Borm, A. Aerts, M.-F. Reyniers, J. A. Martens, and G. B. Marin, "Catalytic Cracking of 2,2,4-Trimethylpentane on FAU, MFI, and Bimodal Porous Materials: Influence of Acid Properties and Pore Topology," *Industrial & Chemical Engineering Fundamentals,* vol. 49, no. 15, pp. 6815-6823, 2010.
[217] M. M. Pereira, F. M. Santos, A. V. Silva, N. Batalha, F. J. F. d. S. Henrique, P. M. Esteves, and B. Louis, "Insights into the Role of Framework and Nonframework Aluminum in the Protolytic Reaction of Carbon–Carbon and Tertiary Carbon–Hydrogen Bonds of Isobutane," *Journal of Physical Chemistry,* vol. 125, no. 21, pp. 11636-11647, 2021.
[218] J. Engelhardt, and W. K. Hall, "Contribution to the understanding of the reaction chemistry of isobutane and neopentane over acid catalysts, I," *Journal of Catalysis,* vol. 125, no. 2, pp. 472-487, 1990.
[219] G. M. Mullen, and M. J. Janik, "Density Functional Theory Study of Alkane-Alkoxide Hydride Transfer in Zeolites," *ACS Catalysis,* vol. 1, no. 2, pp. 102-115, 2011.
[220] M. Gackowski, K. Tarach, Ł. Kuterasiński, J. Podobiński, B. Sulikowski, and J. Datka, "Spectroscopic IR and NMR studies of hierarchical zeolites obtained by desilication of zeolite Y: Optimization of the desilication route," *Microporous and Mesoporous Materials,* vol. 281, pp. 134-141, 2019.
[221] J. V. Milato, R. J. França, A. S. Rocha, and M. R. C. M. Calderari, "Catalytic co-pyrolysis of oil sludge with HDPE to obtain paraffinic products over HUSY zeolites prepared by dealumination and desilication," *Journal of Analytical and Applied Pyrolysis,* vol. 151, pp. 104928, 2020.
[222] S. Li, A. Zheng, Y. Su, H. Zhang, L. Chen, J. Yang, C. Ye, and F. Deng, "Brønsted/Lewis Acid Synergy in Dealuminated HY Zeolite: A Combined Solid-State NMR and Theoretical Calculation Study," *Journal of American Chemical Society,* vol. 129, no. 36, pp. 11161-11171, 2007.